

The Development of Room Temperature Sodium-Sulfur Batteries

**BY
AJIT KUMAR**



DEPARTMENT OF ENERGY SCIENCE AND ENGINEERING

INDIAN INSTITUTE OF TECHNOLOGY BOMBAY, INDIA

SCHOOL OF CHEMISTRY

MONASH UNIVERSITY, AUSTRALIA

July 2020

The Development of Room Temperature Sodium-Sulfur Batteries

Submitted in partial fulfillment of the requirements

of the degree of

Doctor of Philosophy

of the

Indian Institute of Technology Bombay, India

and

Monash University, Australia

by

Ajit Kumar

Supervisors:

Prof. Sagar Mitra (IIT Bombay)

Prof. Douglas R. MacFarlane (Monash University)

Prof. Maria Forsyth (Monash University)



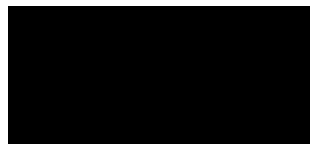
*The course of study for this award was developed jointly by
Monash University, Australia and the Indian Institute of Technology Bombay, India
and was given academic recognition by each of them.
The programme was administrated by The IITB-Monash Research Academy*

July 2020

Dedicated to my parents

Approval Sheet

The thesis entitled “**The Development of Room Temperature Sodium-Sulfur Batteries**” by **Ajit Kumar** is approved for the degree of **Doctor of Philosophy**.



Prof. S. Ramaprabhu

External Examiner



Prof. Venkatasailanathan Ramadesigan

Internal Examiner



Prof. Sagar Mitra

IITB Supervisor



Prof. Douglas R MacFarlane

Monash Supervisor



Date: 09/07/2020
Place: Powai

Prof. Rajiv Dusane
Chairperson

Declaration

I declare that this written submission represents my ideas in my own words and where others ideas or words have been included, I have adequately cited and referenced the original sources,

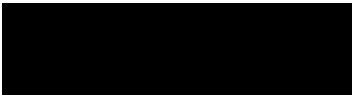
I also declare that I have adhered to all principles of academic honesty and integrity and have not misrepresented or fabricated or falsified any idea/data/fact/source in my submission. I understand that any violation of the above will be cause for disciplinary action by the Institute and can also evoke penal action from the sources which have thus not been properly cited or from whom proper permission has not been taken when needed.

Notice 1

Under the Copyright Act 1968, this thesis must be used only under the normal conditions of scholarly fair dealing. In particular no results or conclusions should be extracted from it, nor should it be copied or closely paraphrase in whole or in part without the written consent of the author. Proper written acknowledgement should be made for any assistance obtained from this thesis

Notice 2

I certify that I have made all reasonable efforts to secure copyright permissions for third-party content included in this thesis and have not knowingly added copyright content to my work without the owner's permission.



Student Name: Ajit Kumar

IITB ID: 154174002

Monash ID: 27331814

Abstract

An electrochemical energy-storage cell, also known as a battery, is one of the best electrical energy-storage devices available. There are types of technologies that come under this category. Since its initiation, the lithium-ion battery has been used as a commercially viable rechargeable battery. However, as the demand for energy-intensive applications grows in the market, there is a requirement for an alternative energy-storage battery technology that can act a good substitute for Li-ion batteries. The sodium-sulfur (Na-S) battery is a well-known large-scale electrochemical storage option. The disadvantage of this particular battery technology is its high operating temperature. Room-temperature sodium-sulfur (RT Na-S) batteries could overcome these issues, but they have issues of their own. The rapid capacity decay is caused by the “polysulfide shuttle” and by the low utilization of the active material that results from the insulating nature of sulfur and the final discharge product. Moreover, the practical performance remains far from theoretical mainly due to sluggish reaction kinetics, severe volume change in sulfur during cycling, and low electronic conductivity of the active material, which limits both their energy and rate characteristics.

To achieve high electronic conductivity and to mitigate the polysulfide dissolution here we present a free-standing cathode using manganese dioxide decorated carbon cloth (CC@MnO₂) as an electronically-conducting substrate and polysulfide reservoir, and sodium polysulfide (Na₂S₆) catholyte as the active material. Without incorporating any active interlayer, nor an expensive ion-selective membrane, this free-standing cathode exhibits an initial reversible specific capacity of 938 mA h g⁻¹ with remarkable capacity retention of 67% after 500 cycles. The as-assembled RT Na-S cell operates at an average potential of 1.82 V and delivered an initial energy density (based on the mass and molecular weight of sulfur and sodium) of 946 W h kg⁻¹, retained an energy density of 855 W h kg⁻¹ after 50 cycles, and attend energy density of 728 W h kg⁻¹ after 500 cycles. Furthermore, the nature of the interactions between MnO₂ and the intermediate polysulfides is investigated by X-ray photoelectron spectroscopy.

To mitigate the severe volume change of sulfur cathode during cycling, we prepared a free-standing cathode scaffold utilizing the advantages of excellent electronic conductivity of carbon cloth, efficient polysulfide adsorption ability of manganese dioxide and outstanding elasticity of sodium-alginate binder, along with facile ion-transport kinetics of liquid-phase Na₂S₆ catholyte as active material. Comprehensive theoretical analysis reveals the possible anchoring sites in sodium-

alginate for polysulfide confinement. At 0.2C ($C = 1672 \text{ mA g}^{-1}$), the freestanding cathode with sulfur loading of 1.7 mg cm^{-2} exhibits high reversible specific capacity during cycling, delivering an initial reversible capacity of 1095 mA h g^{-1} with remarkable capacity retention of 92% after 300 cycles. At 1C, the freestanding cathode delivers an initial reversible specific capacity of 882 mA h g^{-1} , retaining 838 mA h g^{-1} after 1000 cycles. Our freestanding cathode exhibits similar cycling stability even with high sulfur loading of 3.4 mg cm^{-2} , delivering an initial capacity of 752 mA h g^{-1} and retains 710 mA h g^{-1} after 1000 cycles.

To overcome the sluggish reaction kinetics which limit both their energy and rate characteristics, a conceptually new mechanism is demonstrated here based on catalysis by stabilized free radical species, as indicated by ESR measurements, generated on the surface of a Na_2S_6 catholyte-infiltrated activated carbon cloth ($\text{Na}_2\text{S}_6@\text{ACC}$) cathode. We demonstrate by XPS that the mechanism promotes reduction to end-discharge products, including Na_2S , via a surface bound intermediate state, ACC-S_3^- . Due to this catalytic effect of the surface radical species, our RT Na-S cell achieves a high nominal cell potential of 1.85 V. At a current rate of 0.5 C, the Na-S cell delivers a high specific capacity of $866 \text{ mA h g(s)}^{-1}$ and retains $678 \text{ mA h g(s)}^{-1}$ after 700 cycles. The concept of a free-radical mechanism, as described herein, could be adapted to enhance the electrochemical kinetics of other energy storage devices that involve radical intermediate species. To further improved the cell kinetics and cycle life, we decorated the current collector with tin-doped indium oxide by keeping the high proportion of dangling bond in activated carbon cloth, Here we report indium-tin-oxide decorated activated carbon cloth ($\text{ACC}@ \text{ITO}$) as a novel hybride current collector, which eventually resolve all of these major issues. Due to homogeneous dispersibility, liquid-phase sodium polysulfide (Na_2S_6) catholyte has used as an active material. Activated carbon cloth offers three-dimensional pathway for electron conduction throughout the cathode scaffold. Interestingly, the presence of unsaturated carbons containing unpaired electron on the surface of activated carbon cloth enhance the extent of sulfur utilization through free-radical catalysis process. Indium tin oxide, being a polar additive, effectively binds and immobilizes the sodium polysulfides. Besides, due to excellent electronic conductivity of indium tin oxide (ITO), it owns extremely high electronic conductivity and thus greatly facilitates the sluggish kinetics of solid phase interconversion between insoluble lower-order sodium sulfides during charge/discharge process. The $\text{ACC}@ \text{ITO}$ substrate infiltrated with Na_2S_6 catholyte offers a high

reversible specific capacity of 1036 mA h g⁻¹ during second cycle and retains 931 mA h g⁻¹ after 1000 cycles, with an extremely low rate of capacity decay of 0.01% per cycle.

Finally, the practical room temperature sodium-sulfur (RT-NaS) battery technology has a significant potential that can be exploited, and many researchers like us are continually working to resolve the issues. So here, we conclude that by the use of an optimized cathode scaffold which can suppress the polysulfide dissolution and enhance the cell kinetics can make the RT-NaS battery practical. Further, in-detail studies are necessary. Nevertheless, we believe that this work may somehow help in finding the new directions to achieve high capacity and cyclability of RT-NaS battery.

Key Words: Room-temperature Sodium-sulfur batteries; Flexible electrode; Metal oxide; Catholyte; Freestanding cathode; Manganese dioxide; Sodium-alginate; Polysulfide immobilizer

CONTENTS

Abstract	i
List of Figures	vii
List of Abbreviations	xii
Chapter 1: General Introduction	1 - 14
1.1 Motivation	2
1.2 High-temperature sodium-sulfur battery	2
1.3 Working principle of RT Na-S batteries	3
1.4 Parameters for the evaluation of battery performance	5
1.5 Challenges to develop the room-temperature sodium-sulfur batteries	6
1.5.1 Insulating active materials	6
1.5.2 Volume expansion	7
1.5.3 Shuttle phenomenon	7
1.5.4 Self-discharge	8
1.5.5 Sluggish Kinetics	8
1.5.6 Challenges of anode in RT Na-S batteries	8
1.6 Literature studies	9
1.7 Objective / Research plan	11
1.8 Outline of the thesis	12
References	13
Chapter 2: Experimental	15 - 23
2.1 Chemicals	16
2.2 Preparation of Electrolyte	16
2.3 Electrode Materials	16
2.3.1 Preparation of MnO ₂ nanoarrays decorated carbon cloth (CC@MnO ₂)	16
2.3.2 Synthesis of catholyte	17
2.3.3 Preparation of Na-alg wrapped MnO ₂ Nanoarrays Decorated Carbon Cloth	17
2.3.4 Preparation of activated carbon cloth	17
2.3.5 Preparation of activated carbon cloth decorated with indium-tin-oxide (AA@ITO)	18

2.4 Cell Assembly	18
2.4.1 Coin cell assembly for CC@MnO ₂ @Na ₂ S ₆ cathode	18
2.4.2 Coin cell assembly for CC@MnO ₂ @Na ₂ S ₆ @Na-alginate cathode	19
2.4.3 Coin cell assembly for ACC@ Na ₂ S ₆ cathode	19
2.4.4 Coin cell assembly for ACC@ITO@ Na ₂ S ₆ cathode	19
2.5 Experimental Techniques	20
2.5.1 Materials characterizations	20
2.5.2 electrochemical measurements	20
2.5.3 XPS analysis	20
2.5.4 In-situ Raman characterization and analysis	21
2.5.5 ESR spectroscopy	21
2.5.6 Computational details	21
References	23

Chapter 3: High-energy density room temperature sodium-sulfur battery enabled by sodium polysulfide catholyte and carbon cloth current collector decorated with MnO₂ nanoarrays

24 - 40

3.1. Introduction	25
3.2. Results and discussion	26
3.2.1 Synthesis and characterization	26
3.2.2. Electrochemical performances of RT Na-S batteries	27
3.2.3. Probing the mechanism of the interaction between sodium polysulfides and MnO ₂ through X-ray photoelectron spectroscopy	31
3.2.4. Post-cycling analysis of Na-S cell after charge-discharge	35
3.3. Conclusions	38
3.4 References	39

Chapter 4: Robust cathode scaffold for room-temperature sodium-sulfur batteries

41 - 58

4.1. Introduction	42
4.2 Results and discussion	43
4.2.1 Synthesis and characterization	43

4.2.2 Electrochemical performance	46
4.2.3. DFT simulation	50
4.2.4 Post-cycling analysis of CC@MnO ₂ @Na ₂ S ₆ @Na-alginate cathode	53
4.3. Conclusions	55
References	57
Chapter 5: Free-radical catalysis enhances the redox kinetics of roomtemperature sodium-sulfur batteries	59 - 97
5.1 Introduction	60
5.2 Results and discussion	61
5.2.1 Synthesis and characterization	61
5.2.2 Electrochemical performance of RT Na-S batteries	63
5.2.3 Understanding the catalytic behavior of ACC@Na ₂ S ₆ cathode	67
5.2.4 Post-cycling characterization of ACC@Na ₂ S ₆ cathode	77
5.3 Conclusions	78
References	79
Chapter 6: Indium-tin-oxide (ITO) decorated activated carbon cloth as a current collector for room-temperature sodium-sulfur batteries	82 - 102
6.1 Introduction	83
6.2 Results and discussion	84
6.2.1 Synthesis and characterization	84
6.2.2 Electrochemical performances of RT Na-S batteries	85
6.2.3 Understanding the catalytic behavior of ACC@ITO@Na ₂ S ₆ cathode in Na-S battery	89
6.2.4 Post-cycling characterization of Na ₂ S ₆ @ACC@ITO cathode after charge-discharge	95
6.3 Conclusions	95
References	96
Chapter 7: Concluding Remarks and Future Scope	98 - 100

List of Figures

- Figure 1.1** Schematic of RT Na-S battery made of a sodium-metal anode, organic electrolyte, and sulfur-carbon composite cathode. (a) Discharge and (b) Charge. 4
- Figure 3.1:** Schematic of the preparation of CC@MnO₂@Na₂S₆ cathode for room temperature sodium-sulfur batteries. 26
- Figure 3.2:** (a–c) SEM images of CC@MnO₂ at different magnifications. (d) XRD patterns of bare carbon cloth and CC@MnO₂. Low-resolution TEM image (e) and high-resolution TEM image (f) of CC@MnO₂ substrate. 27
- Figure 3.3:** (a) Cyclic voltammograms of the cell for the initial ten cycles, within 1.2–2.6 V at a scan rate of 0.1 mV s⁻¹. (b) Voltage versus charge-discharge capacity profiles of the cathode CC@0.5MnO₂@Na₂S₆ (MnO₂ loading 0.5 mg cm⁻²) at 0.2 A g⁻¹ 28
- Figure 3.4:** (a) Discharge capacity and coulombic efficiency versus cycle number of CC@Na₂S₆ (violet = without MnO₂), and CC@MnO₂@Na₂S₆ (MnO₂ loadings: black = 0.25, red = 0.5 and blue = 0.75 mg cm⁻²) cathodes. (b) Voltage versus charge-discharge capacity profiles of the cathode CC@MnO₂@Na₂S₆ (MnO₂ loading 0.5 mg cm⁻²) at different currents at 20°C ± 2°C 29
- Figure 3.5:** (a) Performances of CC@MnO₂@Na₂S₆ cathode at different currents. (b) Discharge capacity and coulombic efficiency versus cycle number of CC@MnO₂@Na₂S₆ (MnO₂ loading 0.5 mg cm⁻²) at the current rate of 0.2 A g⁻¹ at 20°C ± 2°C. 30
- Figure 3.6.** Discharge profile of 20th cycle for CC@MnO₂@Na₂S₆ cathode at 200 mA g⁻¹. 31
- Figure 3.7:** (a) Mn 2p_{3/2} spectra of CC@0.5MnO₂, CC@0.5MnO₂@Na₂S₄, and CC@0.5MnO₂@Na₂S₆ specimens. (b) S 2p_{3/2} spectrum of CC@0.5MnO₂@Na₂S₆ sample. (c) Photograph of loss of color of polysulfide solution upon addition of MnO₂, indicating “entrapment” of polysulfides on the metal oxide surface. 32
- Figure 3.8:** FTIR spectrum of Na₂S₆ adsorbed MnO₂ sample. 33
- Figure 3.9:** Schematic representation of the possible interactions of manganese oxide with different sodium polysulfides and polythionate complexes. 34
- Figure 3.10:** Post-mortem analysis of CC@0.5MnO₂@Na₂S₆ cathode after 150 cycles, at fully discharged state: low-resolution SEM image (a) and high-resolution

- SEM image (b) of cycled electrode. (c–f) Carbon, sulfur, sodium and manganese mapping on the cycled CC@0.5MnO₂@Na₂S₆ cathode. 35
- Figure 3.11:** Ex-situ high-resolution SEM image of CC@0.5MnO₂@Na₂S₆ cathode after 150 cycles, at fully discharged state, showing a good adhesion of discharged products on the surface of CC@0.5MnO₂ substrate. 36
- Figure 3.12:** XRD patterns of pristine carbon cloth and CC@0.5MnO₂@Na₂S₆ cathode after 150 cycles, at fully discharged state. The appearance of the new peaks (marked with asterisks) seem to be appeared from insoluble lower-order sodium polysulfides (Na₂S_n, 1 ≤ n ≤ 3) deposited on the surface of CC@0.5MnO₂ substrate 37
- Figure 3.13:** Ex-situ SEM images of the surfaces of sodium metal anode placed towards (a) CC@0.5MnO₂@Na₂S₆ cathode and (b) CC@Na₂S₆ cathode after 150 cycles 37
- Figure 4.1:** Schematic representation of CC@MnO₂@Na₂S₆@Na-alginate cathode preparation. 44
- Figure 4.2:** (a-c) SEM images of the CC@MnO₂ at different magnifications; (d-f) SEM images of the CC@MnO₂@Na-alginate substrate at different magnifications. 44
- Figure 4.3:** (a-d) Elemental mapping acquired on the CC@MnO₂@Na-alginate substrate. 45
- Figure 4.4:** (a) Cyclic voltammograms of CC@MnO₂@Na₂S₆@Na-alginate cathode (sulfur loading = 1.7 mg cm⁻²) at the scan rate of 0.1 mV s⁻¹; (b) second cycle discharge profiles of CC@Na₂S₆, CC@MnO₂@Na₂S₆ and CC@MnO₂@Na₂S₆@Na-alginate cathodes with sulfur loading of 1.7 mg cm⁻² at 0.2 C; (c) charge-discharge profiles of the CC@MnO₂@Na₂S₆@Na-alginate cathode (sulfur loading = 1.7 mg cm⁻²) at 0.2C for first, second and fifth cycles. 47
- Figure 4.5:** (a) cycling performance of CC@MnO₂@Na₂S₆ cathode (sulfur loading = 1.7 mg cm⁻²), CC@MnO₂@Na₂S₆@Na-alginate cathode (sulfur loading = 1.7 mg cm⁻²) and CC@MnO₂@Na₂S₆@Na-alginate cathode (sulfur loading = 3.4 mg cm⁻²) at 0.2 C; (b) charge-discharge profiles of CC@MnO₂@Na₂S₆@Na-alginate cathode (sulfur loading = 1.7 mg cm⁻²) cathode at different current rates at 20°C ± 2°C. 48
- Figure 4.6:** (a) rate performance of CC@MnO₂@Na₂S₆ cathode (sulfur loading = 1.7 mg cm⁻²), CC@MnO₂@Na₂S₆@Na-alginate cathode (sulfur loading = 1.7 mg cm⁻²)

and CC@MnO ₂ @Na ₂ S ₆ @Na-alginate cathode (sulfur loading = 3.4 mg cm ⁻²); and (b) long-term cycling of CC@MnO ₂ @Na ₂ S ₆ cathode (sulfur loading = 1.7 mg cm ⁻²), CC@MnO ₂ @Na ₂ S ₆ @Na-alginate cathode (sulfur loading = 1.7 mg cm ⁻²) and CC@MnO ₂ @Na ₂ S ₆ @Na-alginate cathode (sulfur loading = 3.4 mg cm ⁻²) at 1C at 20°C ± 2°C.	50
Figure 4.7: Optimized structures of different sodium-polysulfides.	51
Figure 4.8: Optimized geometries of different polysulfide-adsorbed systems.	52
Figure 4.9: (a) Mulliken charge distribution before and after adsorption of Na ₂ S for site 1 and site 2; (b) binding energies of different Na-polysulfides on sodium-alginate, inset shows optimized geometry and electron density mapping of a sodium-alginate unit; (c) partial density of states of sodium-alginate before and after Na ₂ S ₄ adsorption.	53
Figure 4.10: (a) Scanning electron microscopy image of CC@MnO ₂ @Na ₂ S ₆ @Na-alg cathode after 1000 cycles, at fully discharged state; (b–f) mapping of different elements taken on the cycled electrode.	54
Figure 4.11: (a) SEM image of fresh sodium metal surface before cycling; (b, c) SEM images of cycled sodium anode surface placed towards CC@Na ₂ S ₆ cathode after 50 cycles and CC@MnO ₂ @Na ₂ S ₆ @Na-alg cathode after 300 cycles.	54
Figure 5.1: Schematics of pristine carbon cloth, activated carbon cloth and ACC@Na ₂ S ₆ cathode	61
Figure 5.2: (a–c) SEM images and (d–f) TEM images of pristine carbon cloth (a, d), activated carbon cloth (d, e) and ACC@Na ₂ S ₆ cathode (c, f).	62
Figure 5.3: SEM images of activated carbon cloth before washing (a, b) and after washing with de-ionized water (c, d).	63
Figure 5.4: (a) Cyclic voltammograms of the Na ₂ S ₆ @CC cathode at a scan rate of 0.1 mV s ⁻¹ ; (b) cyclic voltammograms of the Na ₂ S ₆ @ACC cathode at a scan rate of 0.1 mV s ⁻¹ .	64
Figure 5.5: (a) Charge discharge profile of the Na ₂ S ₆ @ACC cathode at 0.2 C; (b) second cycle discharge profiles of the Na ₂ S ₆ @CC and Na ₂ S ₆ @ACC cathode at 0.2 C.	65
Figure 5.6: Second cycle discharge profile of Na ₂ S ₆ @ACC cathode at 0.2 C current rate.	65
Figure 5.7: (a) Cycling performance of Na ₂ S ₆ @CC and Na ₂ S ₆ @ACC cathodes at 0.2 C; (b) charge-discharge profiles of Na ₂ S ₆ @ACC cathode at different current rates.	66

- Figure 5.8:** (a) Rate capability of $\text{Na}_2\text{S}_6@\text{ACC}$ cathode at different current rates; and (b) long-term cycling performance of $\text{Na}_2\text{S}_6@\text{ACC}$ cathode at 0.5 C at $20^\circ\text{C} \pm 2^\circ\text{C}$. 67
- Figure 5.9:** (a) Schematic of in-situ coin cell fabrication; (b) in-situ Raman spectra of RT Na-S battery containing $\text{Na}_2\text{S}_6@\text{ACC}$ cathode 0.1C. 70
- Figure 5.10:** (a) ERS spectra of pristine carbon cloth, partially activated carbon cloth and strongly activated carbon cloth; (b) ESR spectra of blank electrolyte, Na_2S_4 and Na_2S_6 catholytes; (c) deconvoluted C1s XPS spectrum and (d) deconvoluted S 2p_{3/2} XPS spectrum of Na_2S_6 adsorbed activated carbon cloth ($\text{Na}_2\text{S}_6@\text{ACC}$). 71
- Figure 5.11:** XRD pattern of $\text{Na}_2\text{S}_6@\text{PCC}$ cathode (blue) and $\text{Na}_2\text{S}_6@\text{ACC}$ cathode (red) after discharge to 1.8V. 72
- Figure 5.12:** C1s XPS spectra of fresh ACC, fully discharged $\text{Na}_2\text{S}_6@\text{ACC}$ cathode and fully recharged $\text{Na}_2\text{S}_6@\text{ACC}$ cathode. 73
- Figure 5.13:** ESR spectra of fresh ACC (red), fully discharged $\text{Na}_2\text{S}_6@\text{ACC}$ cathode (black) and fully recharged $\text{Na}_2\text{S}_6@\text{ACC}$ cathode (blue) 74
- Figure 5.14:** Reaction mechanism behind the catalytic effect of activated carbon cloth in room temperature sodium-sulfur batteries. 75
- Figure 5.15:** XRD pattern of $\text{Na}_2\text{S}_6@\text{ACC}$ cathode after discharging to 1.2 V. The XRD pattern confirms the complete reduction of sulfur to lower-order sodium polysulfides (Na_2S_2 and Na_2S) as fully discharged products. 76
- Figure 5.16:** (a) Scanning electron microscopy image of $\text{Na}_2\text{S}_6@\text{ACC}$ cathode after 700 cycles, at fully discharged state; (b-f) Mapping of different elements taken on the cycled electrode 77
- Figure 6.1:** Schematic representation of pristine carbon cloth (CC), activated carbon cloth decorated with tin-doped indium-oxide nanoparticle ($\text{ACC}@ \text{ITO}$) and catholyte loaded on activated carbon cloth decorated with tin-doped indium-oxide nanoparticle ($\text{ACC}@ \text{ITO} @ \text{Na}_2\text{S}_6$). 84
- Figure 6.2:** (a–d) SEM images and (e) TEM image of activated carbon cloth decorated with tin-doped indium-oxide nanoparticle ($\text{ACC}@ \text{ITO}$) and (f) $\text{ACC}@ \text{ITO} @ \text{Na}_2\text{S}_6$ cathode. 85
- Figure 6.3:** (a) Cyclic voltammograms of the $\text{ACC}@ \text{ITO} @ \text{Na}_2\text{S}_6$ cathode at a scan rate of 0.1 mV s^{-1} ; (b) charge-discharge profiles of the $\text{ACC}@ \text{ITO} @ \text{Na}_2\text{S}_6$ cathode

at 0.2 C; (c) second cycle discharge profiles of ACC@ITO@ Na ₂ S ₆ and CC@Na ₂ S ₆ cathodes at 0.2 C at 20°C ±2°C.	86
Figure 6.4: (a) cycling performance of ACC@ITO@ Na ₂ S ₆ cathode at different current rates; (b) charge-discharge profiles of ACC@ITO@Na ₂ S ₆ cathode at different current rates at 20°C ±2°C.	87
Figure 6.5: (a) rate capability of ACC@ITO@ Na ₂ S ₆ cathode at different current rates; and (b) long-term cycling performance of ACC@ITO@ Na ₂ S ₆ cathode with different sulfur loading at 0.5 C at 20°C ±2°C.	88
Figure 6.6: (a) ERS spectra of pristine carbon cloth, NaOH activated carbon cloth, ITO powder and activated carbon cloth decorated with tin-doped indium-oxide nanoparticle (ACC@ITO); (b) ESR spectra of blank electrolyte, Na ₂ S ₄ , Na ₂ S ₆ , and Na ₂ S ₈ catholyte.	90
Figure 6.7: XPS spectra of fresh ACC@ITO (a), fully discharged Na ₂ S ₆ @ACC cathode (b) and fully re-charged Na ₂ S ₆ @ACC cathode (c).	91
Figure 6.8: XRD pattern of ACC@ITO (a) and ACC@ITO@Na ₂ S ₆ cathode after 50 cycles at 0.2 C, at fully discharged state (b). The XRD pattern confirms the complete reduction of sulfur to lower-order sodium polysulfides (Na ₂ S ₂ and Na ₂ S) as fully discharged products.	92
Figure 6.9: Reaction mechanism behind the catalytic effect of ACC@ITO in room temperature sodium-sulfur batteries.	93
Figure 6.10: (a) Scanning electron microscopy image of ACC@ITO@ Na ₂ S ₆ cathode after 1000 cycles, at fully discharged state; (b–f) mapping of different elements taken on the cycled electrode.	94

List of Abbreviations

ACC	Activated carbon cloth
ITO	Indium tin oxide
BET	Brunauer – Emmett – Teller
CC	Carbon cloth
PCC	Pristine carbon cloth
CV	Cyclic voltammetry
DFT	Density functional theory
DI-water	De-ionized water
EDXS	Energy dispersive X-ray spectroscopy
EIS	Electrochemical impedance spectroscopy
FEG – SEM	Field emission gun scanning electron microscopy
FEG-TEM	Field emission gun transmission electron microscopy
FTIR	Fourier transform infrared spectroscopy
HR-TEM	High resolution transmission electron microscopy
JCPDS	Joint committee on powder diffraction standards
LIB	Lithium ion battery
OCV	Open circuit voltage
PVDF	Polyvinylidene difluoride
RT Na-S	Room-temperature Sodium sulfur
SEI	Solid electrolyte interface
SIB	Sodium ion battery
XPS	X-ray photoelectron spectroscopy
XRD	X-ray diffraction

Chapter 1

Introduction

Chapter 1

1.1 Motivation

The increasing human population and consumption of electricity per capita generate a high demand for electrical energy. Currently, the limited sources of fossil fuels are being used for the electrification of vehicles and electricity generation. Due to the continual use of renewable sources of energy such as wind and solar, there is always a requirement for an energy-storage device. To fulfill the current demands of electrical energy and its storage, modern society requires an efficient and low-cost energy-storage unit. Since conventional lithium-ion batteries are nearing their theoretical energy-density limits (500 W h kg^{-1})¹⁻³, metal-sulfur (Li-S, Na-S, and Mg-S) batteries are becoming significant due to their high energy-storage capacity⁴⁻⁶. Since the last decade, the lithium-sulfur battery has gained special attention among metal-sulfur batteries due to the high theoretical capacity of sulfur (1672 mA h g^{-1}), lithium (3885 mA h g^{-1}), and the energy density of the lithium-sulfur (Li-S) battery (2500 W h kg^{-1}). Natural abundance and the environment-friendliness of elemental sulfur⁶⁻¹⁰ make this battery a more promising alternative toward a green energy-storage system. Sodium is the alternative anode to lithium. Sodium is the second lightest and smallest alkali metal in a periodic table with a theoretical capacity of 1165 mA h g^{-1} . The theoretical energy density of a room-temperature sodium-sulfur (RT Na-S) battery is 1230 W h kg^{-1} . The cost of the RT Na-S battery is significantly lesser (the price of Na is only $1/25^{\text{th}}$ that of Li) than Li-S,¹¹ which is due to the abundance of sodium (Na - $23.6 \times 10^3 \text{ mg kg}^{-1}$ and Li- 20 mg kg^{-1} of the earth's crust)¹²⁻¹⁶. The global distribution of sodium also renders it a more suitable and viable option than lithium¹⁶.

1.2 High-temperature sodium-sulfur battery

The high-temperature sodium-sulfur battery was introduced by Ford Motors in the 1960s, and the technology was marketed by Nihon Gaishi Kaisha (NGK Insulators, Ltd. Nagoya, Japan), Japan, which is known to be a primary source of large-scale electrochemical storage options to date. High-temperature (above 300°C) sodium-sulfur (Na-S) batteries that are made of a liquid sodium (m.p. 98°C) anode, liquid sulfur (m.p. 118°C) cathode, and a solid beta-alumina electrolyte^{17,18} have been used in grid-scale energy-storage systems. However, the main drawbacks of the high-temperature sodium-sulfur battery are that it contains highly corrosive sulfur and that its reduced products (sodium polysulfides) require perfect sealing and packing¹⁷, maintenance, and power

consumption; this further reduces the energy-storage efficiency of the battery¹⁹, and it induces explosions²⁰. Assuming that Na_2S_3 (m.p. 235 °C) is the final discharge product, a high-temperature sodium-sulfur battery can use a maximum of 33.3 % (558 mA h g⁻¹) of the full capacity of sulfur (1672 mA h g⁻¹), and the maximum theoretical energy density of the battery is 760 W h kg⁻¹.¹⁵ This limitation of the theoretical capacity of high-temperature sodium-sulfur batteries is due to high melting point of low-order sodium polysulfide (Na_2S_2 - m.p. 475 °C and Na_2S – m.p. 1176 °C), which is the reduced product of sulfur. The development of an ambient- or room-temperature sodium-sulfur battery has been reported from 2006, and it has been continually gaining attention as an alternative to large-scale energy storage^{6-10, 21-27}.

1.3 Working principle of RT Na-S batteries

Conventional room-temperature sodium-sulfur batteries have solid electrodes and a liquid electrolyte. In the RT Na-S battery, the sodium metal is an anode and the sulfur-carbon composite acts as the cathode. The electrolyte is an electronic insulator but a high ionic conductor, which provides a way to migrate the ions inside the cell between the anode and cathode. In the discharge process, the anode releases electrons to the external circuit and gets oxidized during the electrochemical reaction. The cathode accepts electrons from the external circuit, and it is reduced during the electrochemical reaction. The reversal of the discharge process is a charge process or charging. The electrochemical reaction of a rechargeable battery must be reversible on application of a charging current and voltage. This is the process to convert electrical energy into chemical energy. The power source extracts the electrons from the cathode and pumps them to the anode. Figure 1 represents the schematic of (a) discharge and (b) charge mechanisms of the RT Na-S battery, in which elemental sodium (Na) is the anode and the sulfur-carbon composite is utilized as a cathode.

Discharge

The discharge reaction at the anode and the cathode in the Na-S battery is shown in Figure 1(a). Sodium oxidizes and provides electrons to the external circuit load, whereas sulfur reduces and accepts the electrons from the external circuit load, through the current collector and carbon additives. Oxidized sodium ion (Na^+) moves through the electrolyte from the anode to the cathode, as shown in Figure 1a. During discharge, as the transition of sulfur to sodium sulfide (Na_2S) occurs,

several steps are followed through a series of long-chain (Na_2S_n , $4 \leq n \leq 8$) and short-chain (Na_2S_n , $1 \leq n \leq 3$) sodium polysulfide intermediate compounds^{12, 20}. Long-chain sodium polysulfide is soluble and short-chain sodium polysulfide is insoluble in organic electrolyte¹⁰.

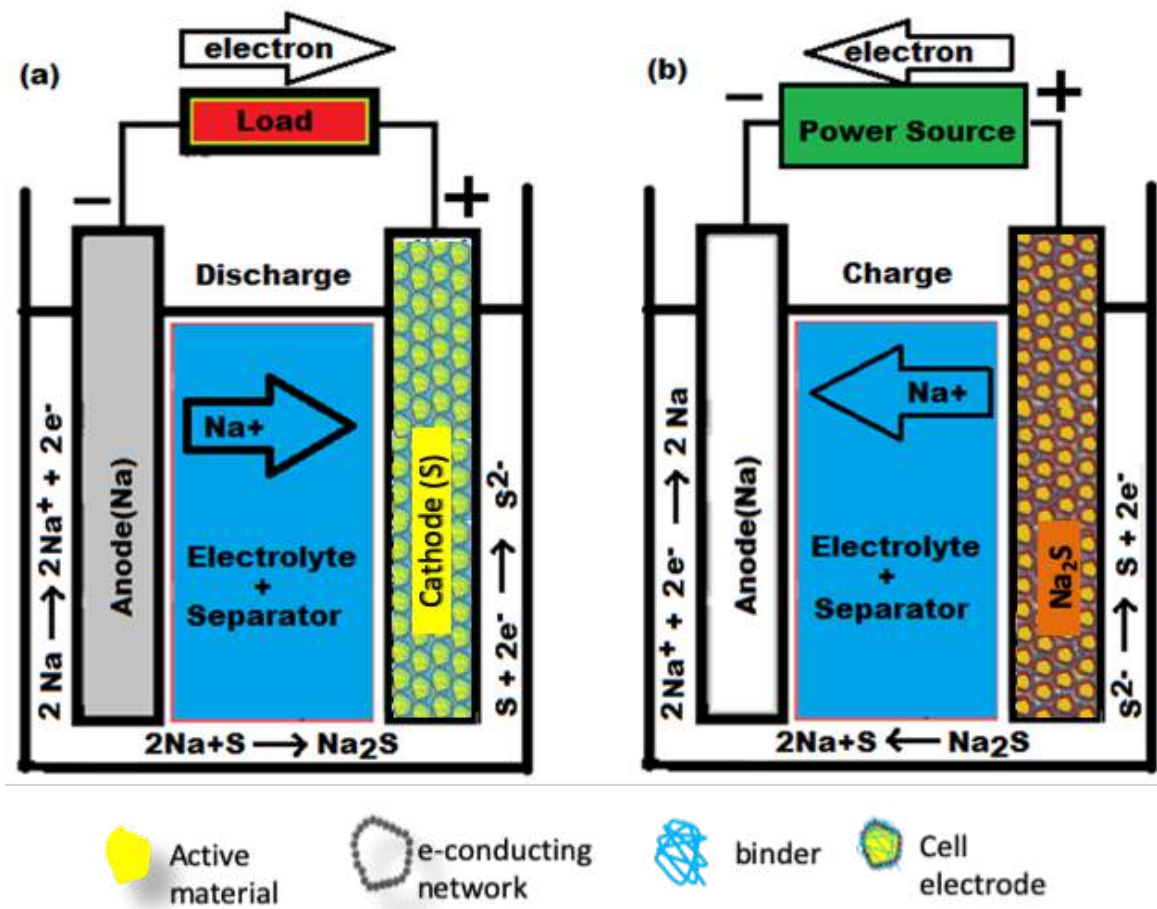


Figure 1: Schematic of RT Na-S battery made of a sodium-metal anode, organic electrolyte, and sulfur-carbon composite cathode. (a) Discharge and (b) Charge.

Charge

During charge, cations (Na^+) migrate through the electrolyte from the cathode to the anode, the discharged cathode (Na_2S) oxidizes into sulfur, and the migrated cations (Na^+) reduce into sodium metal at the anode, as shown in Figure 1b. The corresponding reactions at the anode and the cathode during the charging process are shown in Figure 1(b).

1.4 Parameters for the evaluation of battery performance

1.4.1 Specific Capacity

Specific capacity is the amount of charge stored per unit mass of a given material. The unit of specific capacity is mAh g⁻¹.

Specific capacity of electrode: It is the amount of charge stored per unit mass of electrode's active material. In this report each and every value of specific capacity of cathode electrode is calculated with respect to the mass of the sulfur only.

Specific capacity of cell: It is the amount of charge stored per unit mass of both electrode's active material (anode and cathode). In this report each and every value of specific capacity of cell is calculated with respect to the mass of the sulfur and sodium both.

$$\text{Specific capacity of cell} = \frac{C_{\text{anode}} \times C_{\text{cathode}}}{C_{\text{anode}} + C_{\text{cathode}}} \text{ (mAh g}^{-1}\text{)} \quad \dots \text{eq. (1.1)}$$

Where, C_{anode} and C_{cathode} is the specific capacity of anode and cathode, respectively.

1.4.2 Cell voltage

Cell voltage is the potential difference between the two electrodes, (anode and cathode) and is the most important parameter of a cell for its electrochemical state evaluation.

Open circuit voltage (OCV): The potential difference between the electrodes when the charge/discharge current is zero is known as open circuit voltage.

$$E_{\text{cell}} = E_{\text{cathode}} - E_{\text{anode}} \quad \dots \text{eq. (1.2)}$$

Average cell voltage: The average cell voltage is defined as the ratio of total energy stored and the total storage capacity of the cell

$$V_{\text{avg}} = \frac{\text{Full cell energy density}}{\text{Full cell specific capacity}}$$
$$V_{\text{avg}} = \frac{1}{\int_{Q_1}^{Q_2} dQ} \int_{Q_1}^{Q_2} V dQ \quad \dots \text{eq. (1.3)}$$

Where, $\int_{Q_1}^{Q_2} dQ$ represents the specific discharge capacity and $\int_{Q_1}^{Q_2} V dQ$ (= area under the curve) represents the corresponding specific discharge energy.

1.4.3 Full-cell energy density

It is the amount of energy stored per unit mass of both electrode's active material (anode and cathode). The unit of energy density is Wh kg⁻¹

The full cell energy density is calculated by using the following formula:

$$\text{Energy density} = \text{average cell potential} \times \text{full cell specific capacity}$$

1.4.4 Coulombic efficiency

It is the ratio of specific charge capacity to the specific discharge capacity

$$\text{Coulombic efficiency} = \frac{\text{Charge capacity}}{\text{Discharge capacity}} \times 100 \%$$

1.4.5 Capacity retention

$$\text{Capacity retention after } n^{\text{th}} \text{ cycle} = \frac{\text{Initial discharge capacity} - n^{\text{th}} \text{ cycle discharge capacity}}{\text{initial discharge capacity}} \times 100 \%$$

Rate of capacity decay:

$$\text{Rate of capacity decay for } n \text{ cycle} = \frac{\text{Initial discharge capacity} - n^{\text{th}} \text{ cycle discharge capacity}}{\text{initial discharge capacity} \times \text{no. of cycles}} \times 100 \%$$

1.5 Challenges to develop the room-temperature sodium-sulfur batteries

Although the RT Na-S battery claims many advantages, there are major challenges associated with such technology, for example, the low utilization of the active material, which is due to the insulating nature of the active material (sulfur and polysulfides)⁶. The capacity loss of cell during both cycling and at rest is the result of elemental sulfur and polysulfide dissolution¹⁰. This in turn eventually produces low Coulombic efficiency and poor cycle life⁸. Self-discharge is another outcome of the dissolution process. Another major issue that inhibits the Na-S battery from reaching its full potential is the high electrode volume expansion that arises due to the transition of sulfur to solid-state short-chain polysulfides¹⁰. Furthermore, the sluggish reaction kinetics between Na-S and the electrical insulating nature of sulfur and its discharged products results in low reversible capacity²⁹. The associated challenges are elaborated in detail in the following sections:

1.5.1 Insulating active materials

Sulfur has a very low electronic conductivity of $1 \times 10^{-15} \text{ S m}^{-1}$ at room temperature. Furthermore, the discharge products that arise from the electrochemical reaction, namely, sodium sulfide also has poor electrical conductivity. The transportation of electrons from the active material (sulfur and polysulfides) to the current collector requires a high proportion and relevant structures of the

electrically conductive matrix in the cathode structure. The poor conductivity of active material results in lesser utilization of the active material and low specific capacity.

1.5.2 Volume expansion

During the discharge process, the cyclic S_8 molecules of sulfur undergo a series of transition reactions and produce sodium polysulfides. The transition between elemental sulfur (S_8) and long-chain polysulfide (Na_2S_n , $4 \leq n \leq 8$) does not induce too much volume change in the cathode, because the long-chain polysulfides are generally soluble and exist as liquid-phase species. However, the large volume change occurs when solid-state short-chain polysulfides (Na_2S_n , $1 \leq n \leq 3$) are produced. The density difference between elemental sulfur (1.96 g cm^{-3}) and Na_2S (1.86 g cm^{-3}) can generate a volume expansion of the sulfur cathode up to 154.5 % upon a full discharge. The large volume change of the cathode can destroy the mechanical integrity of sulfur-active materials within the conductive matrix, and it may result in capacity fading. In addition, since both sulfur and sodium polysulfides are electronic insulators, the volume change can destroy the electrical contacts between the carbon matrix and the active materials, so that the utilization of the active material and other electrochemical performances of the RT Na-S batteries are affected as well. Due to these reasons, the development of advanced cathode structures to accommodate the volume change of sulfur electrodes during deep discharge is essential to improve the cyclability of Na-S batteries.

1.5.3 Shuttle phenomenon

Long-chain sodium polysulfides (Na_2S_n , $4 \leq n \leq 8$) are soluble in most organic electrolytes¹⁰. During the discharging-charging process, these polysulfides can freely migrate between the cathode and the anode, and this process is called the polysulfide shuttle phenomenon⁸. The behavior of the shuttle is the main reason for the low Coulombic efficiency of RT Na-S batteries. The long-chain polysulfides migrate toward the anode (Na), react with sodium metal, reduce to short-chain polysulfides, migrate back to the cathode, form long-chain polysulfides again, and so on.

1.5.4 Self-discharge

Self-discharge is another challenge to deal with before the RT Na-S batteries can be made commercially viable. Unfortunately, RT Na-S batteries have strong self-discharge behavior because of the dissolution of elemental sulfur as well as long-chain sodium polysulfides into organic electrolytes. Long-chain sodium polysulfides after discharging continue to slowly dissolve in the electrolyte even in the resting stage. When the batteries are at rest, the self-discharge occurs because the active materials gradually dissolve and diffuse to the anode due to the concentration gradient and then react with sodium metal, which results in a decrease in the open-circuit voltage and discharge capacity.

1.5.5 Sluggish Kinetics

The accessible capacity of the RT-NaS battery, which is much lower than the theoretical capacity, is caused by the insulating nature of sulfur and the sluggish reactivity of sulfur with sodium. Due to slow kinetics and non-conductive nature of Na_2S_2 and Na_2S , the Na-S battery suffers from irreversible capacity loss. This results in an incomplete reduction of Na_2S rather than a complete production^[10].

1.5.6 Challenges of anode in RT Na-S batteries

The applications of RT Na-S batteries are being hindered due to several issues related to the metallic sodium anode. The sodium metal anode is an essential part of the RT Na-S battery system because the anode stability determines the long-term cycle stability of RT Na-S batteries. However, metallic sodium is unstable with organic electrolytes, which hampers the performance of rechargeable batteries. The electrolyte gets reduced on the anode surface to form a SEI layer, leading to an enhancement in overall cell impedance⁷. The most serious concern related to metallic sodium is the dendrite formation. The dendrite formation occurs due to uneven deposition of Na atoms on the sodium metal anode surface¹⁰. The rapid growth of Na dendrite raises the safety issues for RT Na-S batteries. Moreover, in the RT Na-S batteries, bare sodium metal anode reacts with soluble higher-order polysulfides to form the insoluble lower-order sulfides (Na_2S_2 , Na_2S). This phenomenon also contributes towards the cell impedance, leading to poor electrochemical performances.

1.6 Literature studies

The high-temperature the Na-S battery has long been considered one of the most viable electrochemical storage solutions; however, high-level safety issues and material degradation make the technology less attractive²⁰. To mitigate the operational issues at a high temperature, researchers have recently attempted to develop room-temperature sodium-sulfur (RT Na-S) battery chemistry¹⁰.

Room-temperature Na-S batteries experience certain challenges such as low sulfur utilization due to poor electronic conductivity of sulfur and sluggish kinetics, continuous dissolution of polysulfide intermediates, and volume expansion⁸.

As mentioned earlier, sulfur has many advantages as a cathode material, but it suffers from poor electrical conductivity. Yu et al.¹⁶ reported that the overall practical discharge capacity (1050 mAhg⁻¹) of the RT Na-S cell is between the theoretical capacity at the discharge products, Na₂S₂ and Na₂S, which indicates that elemental sulfur is not completely discharged to S²⁻. It indicates that the final discharged products may constitute a mixture of Na₂S₂ and Na₂S. Thus, the intermediate polysulfides that are produced from the sulfur in the cycling process results in poor conductivity as well.

Park et al.³ reported on the first effective use of this strategy through physical mixing. This method is simple and effective, but it only results in poor accessibility and steeper capacity decay with cycling. This is because direct mechanical mixing can result in poor contact between S and the conductive additives. Moreover, a large amount of sulfur deposits in agglomeration form on the carbon surface. This results in an inferior electrochemical performance due to diffusion and the blockage of electron transport.

It has also been reported that physical confinement of sulfur within a microporous carbon matrix was effective in terms of improvement in electronic conductivity of sulfur and physical reservoirs of polysulfides in sodium-sulfur batteries⁷.

In another study, Yu et al.⁶ reported free-standing binder-free multiwall carbon nanotube (MWCNT) fabric electrodes by using soluble sodium polysulfide (catholyte) and multiwall carbon nanotube fabric. This nanostructured, free-standing MWCNT fabric electrode acts as a high-surface area current collector. The sodium polysulfide catholyte/MWCNT fabric cathode provides

greater utilization of the active material and capacity retention during cycling than does the traditional solid sulfur-carbon composite cathode.

The sluggish reaction kinetics between Na and S and the electrical insulating nature of sulfur and its discharged products cause low reversible capacity¹⁰. This challenge was addressed by Lee et al.³³; he explored the possibility of hollow carbon spheres as an effective S host. The interior void space of the hollow carbon has the ability to accommodate active elemental sulfur in large amounts. This guarantees high sulfur loading in the composite. In addition, the carbon shell has the ability to confine the starting active sulfur and polysulfides in its interior space, which inhibits the shuttle effect. The developed composite delivered a reversible capacity of $\approx 600 \text{ mA h g}^{-1}$ over 20 cycles. Unfortunately, the polysulfide intermediates (Na_2S_n , $4 \leq n \leq 8$) that are formed during charge-discharge are soluble in both ether¹⁵ and a carbonate-based electrolyte²⁵. The dissolution triggers shuttling of polysulfides between the cathode and the anode, which induces a low discharge capacity, fast capacity fade, and deterioration of the anode^{21–27}.

To overcome the issue of polysulfide dissolution and the shuttling mechanism, a Nafion-coated polypropylene separator⁷ and a presodiated Nafion polymer membrane⁸ have been investigated as nonporous separators to improve cell performance, in aspects of cyclability and high capacity. The sodiated Nafion coating on a porous polypropylene membrane combines both sufficient sodium-ion conductivity and reduced polysulfide permeation. This coated separator that consisting of a thin layer of Nafion that is hosted on a standard porous polypropylene separator results in a lower capacity fading than in cells with a non-coated separator⁷.

In another strategy, a carbon interlayer is used between a sulfur cathode and the separator, which traps the long-chain polysulfides and reutilizes it, improving the cycle life of the RT Na-S battery¹⁰. To alleviate polysulfide diffusion and reutilization of active materials, Yu et al. used a presodiated nonporous Nafion membrane that was coated with carbon nanostructures between the cathode and the anode, which resulted in improved capacity and high cyclability⁸.

Carter et al. physically trapped short sulfur molecules (S_n , $n \leq 4$) in nanopores of carbon²¹ to investigate the system as a cathode, in which the formation of long-chain sodium polysulfides (Na_2S_n , $4 \leq n \leq 8$) was not allowed.

All these strategies have a positive effect on the cycle life of the RT Na-S battery. However, such architectures of a sulfur cathode and cell structures have been focused to physically trap the sodium polysulfides into the cathode and at the interface of cathode and separator.

1.7 Objective / Research plan

From the multiple strategies adopted by various researchers, in order to increase the overall capacity and cyclability of RT-NaS batteries, many improvements have been made. However, the full potential of the reach of RT-NaS batteries is currently unrealized. For example, the nonpolar carbon additives exhibit inefficacious physisorption toward the polar sodium polysulfides in alleviating the shuttle phenomenon. Moreover, due to the hydrophobic surface of carbon and the higher solvation energy of long-chain polysulfides, intermediate polysulfides have the natural tendency to diffuse into the electrolyte. Therefore, a sulfur host that can offer strong chemical interaction sites to polysulfides, along with a stable electronically conductive network is desirable to improve the overall performances of Na-S batteries. In this work, a new path has been adopted to overcome the cumbersome challenges associated with RT-NaS batteries, by investigating the potential of a cathode scaffold that has distinct properties i.e., electronic conductivity and mechanical integrity.

Based on an understanding of the working principle of RT-NaS batteries and literature studies, it can be concluded that an ideal conductive network (cathode scaffold), which can be a good host to the active material, should meet a certain criterion. To serve the purpose, a cathode scaffold is prepared, which acts as an efficient polysulfide reservoir that can trap the polysulphides, thus inhibiting their dissolution into the electrolyte. However, it is composed in an electronically conducting substrate. Additionally, the cathode scaffold acts as a conductive sulfiphilic host to support the reversible redox conversion of sulfur to discharge products and vice versa. At the same time, sufficient free space is available to accommodate the expanded active materials, which results from the discharged products that are produced during electrochemical cycling. It had to be ensured that there is a seamless transport of electrons and Na-ion for the electrochemical reaction. Furthermore, to overcome the slow kinetics of the RT Na-S battery, a superior catalytic substrate/current collector is employed. The objectives of this project are designed to enable the developing of the cathode scaffold, which may comprise all the characteristics mentioned above along with high-energy density and a long cycle life.

For this purpose, it was important to identify the demerits of the sulfur-carbon composite electrode, which has been extensively used in several studies, as mentioned in the section on literature review. Despite using this strategy, however, capacity fading occurred after a few cycles. Therefore, it was

important to understand the reason for capacity fading and to enhance the performance of the cell so that a different strategy can be employed to overcome the issue: the selection of a suitable current collector/cathode scaffold. Further, ways to modify the cathode scaffold have been explored to increase the cell energy density. In order to explore the hosting capabilities of the cathode scaffold, the extent of utilization of the sodium polysulfide (Na_2S_6) catholyte as an active material into the flexible substrate is studied. An electronically conductive and mechanically stable cathode scaffold is developed. Investigating the interaction between sodium polysulfides and MnO_2 is also an important process that must be studied and analyzed. At later stages, the redox kinetics of sulfur conversion is enhanced by modifying the surface of the current collector to catalyze the conversion of sulfur to low-order polysulfides.

To observe the effect of the cathode scaffold on cell kinetics, the catalytic behavior of the $\text{ACC@Na}_2\text{S}_6$ cathode in the Na-S battery is studied. The cathode scaffold is decorated with electronic conductive polar ceramic particles. To overcome the pulverization issues of the cathode due to volume expansion of the cathode during discharge, a sulfiphilic cathode scaffold wrapped with a polar binder is used.

1.8 Outline of the thesis

Throughout the following seven chapters, the scope of the application of room-temperature sodium-sulfur (RT-NaS) batteries is discussed in detail.

Chapter 1 contains the basic details of the introduction and the literature survey of the RT-NaS battery. Chapter 2 deals with the experimental section, and it provides information on the procedure that was followed for the synthesis and the characterization techniques. Chapter 3 describes a high energy-density room-temperature sodium-sulfur battery that is enabled by a sodium polysulfide catholyte and a carbon cloth current collector that is decorated with MnO_2 nanoarrays. Chapter 4 contemplates a robust cathode scaffold for room-temperature sodium-sulfur batteries. Chapter 5 reveals free-radical catalysis, which enhances the redox kinetics of room-temperature sodium-sulfur batteries. Chapter 6 provides a description on the indium-tin-oxide (ITO)-decorated activated carbon cloth as a current collector for room-temperature sodium-sulfur batteries. In Chapter 7, we present a brief summary of the thesis, and we discuss the scope for the future application of RT-NaS batteries.

References

1. B. Dunn, H. Kamath and J. M. Tarascon, *Science*, 2011, 334, 928–935.
2. X. Lu, G. Xia, J. P. Lemmon and Z. Yang, *J. Power Sources*, 2010, 195, 2431–2442.
3. C.W. Park, J. H. Ahn, H.S. Ryu, K. W. Kim and H.J. Ahn, *Electrochem. Solid-State Lett.*, 2006, 9, A123–A125.
4. S. Wenzel, H. Metelmann, C. Reiß, C., A. K. Dürr, J. Janek and P. Adelhelm, *J. Power Sources*, 2013, 243, 758–765.
5. S. Xin, Y. X. Yin, Y.G. Guo and L.J. Wan, *Adv. Mater.*, 2014, 26, 1261–1265.
6. X. Yu and A. Manthiram, *J. Phys. Chem. C*, 2014, 118, 22952–22959.
7. I. Bauer, M. Kohl, H. Althues and S. Kaskel, *Chem. Commun.*, 2014, 50, 3208–3210.
8. X. Yu and A. Manthiram, *Adv. Energy Mater.*, 2015, 5, 1500350.
9. X. Yu and A. Manthiram, *Chem. Eur. J.*, 2015, 21, 4233–4237.
10. A. Manthiram and X. Yu, *Small*, 2015, 11, 2108–2114.
11. I. Kim, J. Y. Park, C. H. Kim, J. W. Park, J. P. Ahn, J. H. Ahn, K.W. Kim and H.J. Ahn, *J. Power Sources*, 2016, 301, 332–337.
12. I. Kim, C. H. Kim, S. H. Choi, J. P. Ahn, J. H. Ahn, K. W. Kim, E. J. Cairns, and H. J. Ahn, *J. Power Sources*, 2016, 307, 31–37.
13. S. Wei, S. Xu, A. Agrawal, S. Choudhury, Y. Lu, Z. Tu, L. Ma and L.A. Archer, *Nat. Commun.*, 2016, 7, 11722.
14. Y.-X. Wang, J. Yang, W. Lai, S.-L. Chou, Q.-F. Gu, H. K. Liu, D. Zhao and S. X. Dou, *J. Am. Chem. Soc.* 2016, 138, 16576–16579.
15. I. Kim, J. Y. Park, C.H. Kim, J. W. Park, J. P. Ahn, J. H. Ahn, K. W. Kim and H. J. Ahn, *J. Electrochem. Soc.*, 2016, 163, 611–616.
16. X. Yu and A. Manthiram, *Chem. Mater.*, 2016, 28, 896–905.
17. Y. M. Chen, W. Liang, S. Li, F. Zou, S. M. Bhaway, Z. Qiang, M. Gao, B. D. Vogt and Y. Zhu, *J. Mater. Chem. A*, 2016, 4, 12471–12478.
18. Z. Qiang, Y. M. Chen, Y. Xia, W. Liang, Y. Zhu and B. D. Vogt, *Nano Energy*, 2017, 32, 59–66.
19. L. Fan, R. Ma, Y. Yang, S. Chen and B. Lu, *Nano Energy*, 2016, 28, 304–310.

20. Y.-X. Wang, B. Zhang, W. Lai, Y. Xu, S.-L. Chou, H.-K. Liu and S.-X. Dou, *Adv. Energy Mater.*, 2017, 7, 1602829.
21. R. Carter, L. Oakes, A. Douglas, N. Muralidharan, A. P. Cohn and C. L. Pint, *Nano Lett.* 2017, 17, 1863–1869.
22. A. Ghosh, S. Shukla, M. Monisha, A. Kumar, B. Lochab and S. Mitra, *ACS Energy Lett.*, 2017, 2, 2478–2485.
23. S. Gope, D. K. Singh, M. Eswaramoorthy and A. J. Bhattacharyya, *ChemistrySelect*, 2017, 2, 9249–9255.
24. Y. Hao, X. Li, X. Sun and C. Wang, *ChemistrySelect*, 2017, 2, 9425–9432.
25. D. Ma, Y. Li, J. Yang, H. Mi, S. Luo, L. Deng, C. Yan, M. Rauf, P. Zhang, X. Sun, X. Ren, J. Li and H. Zhang, *Adv. Funct. Mater.*, 2018, 28, 1705537.
26. M. A. Yahya, C.W. Zanariah, C. W. Ngah, M. A. Hashim and Z. Al-Qodah, *Journal of Materials Science Research*, 2016, 5, 24–31.
27. S. Y. Moon, M.-S. Kim, H.-S. Hahm and Y.-S. Lim, *Materials Science Forum*, 2006, 510, 750–753.
28. H. M. Kim, J-Y Hwang, A. Manthiram, Y. K. Sun, *ACS Appl. Mater. Interfaces* 2016, 8, 983-987.
29. D.-J. Lee, J.-W. Park, I. Hasa, Y.-K. Sun, B. Scrosati, J. Hassoun, *J. Mater. Chem. A* 2013, 1, 5256.

Chapter 2

Experimental

Chapter 2

2.1 Chemicals

Sulfur powder, tetraethyleneglycoldimethylether (TEGDME) solvent, indium chloride (InCl_3), tin chloride (SnCl_4), alginic acid sodium salt (Na-alginate), sodium nitrate (NaNO_3) and sodium perchlorate (NaClO_4) were purchased from Sigma-Aldrich. Potassium permanganate (KMnO_4) and nitric acid (HNO_3) from Fisher Scientific. Anhydrous sodium sulfide (Na_2S) from Acros Organics. Sodium hydroxide (NaOH) from MERCK. All the chemicals were used as received.

2.2 Preparation of Electrolyte

Ether-based organic liquid electrolytes for catholyte and coin-cell assembly were prepared by solubilizing NaClO_4 and NaNO_3 into tetramethylene glycol dimethyl ether solvent inside the glove box. The concentration of NaClO_4 and NaNO_3 was maintained 1.5 M and 0.2 M respectively, which termed as a base/blank electrolyte.

2.3 Electrode Materials

2.3.1 Preparation of MnO_2 nanoarrays decorated carbon cloth (CC@MnO_2)

Manganese dioxide decorated carbon cloth was synthesized in an autoclave through a reported hydrothermal method¹. A commercially available carbon cloth (W0S1002) was washed thoroughly with diluted HNO_3 and then placed inside a Teflon-lined stainless-steel autoclave, standing against the wall. An aqueous solution of KMnO_4 was transferred into the autoclave. The sealed autoclave was heated at 150 °C for 12 h in a muffle furnace and then cooled down to room temperature. After the hydrothermal reaction, the carbon cloth was removed from the autoclave and washed with DI water followed by acetone to remove all residual side products. The dark brown color of the matrix confirmed a uniform growth of MnO_2 on the surface of carbon cloth. The MnO_2 decorated carbon cloth is designated and further referred as CC@MnO_2 . After successful synthesis, the CC@MnO_2 was dried for 24 h at 70 °C under vacuum. Carbon cloths with different MnO_2 loading were synthesized to optimize the cathode performances.

2.3.2 Synthesis of catholyte

To prepare a Na₂S₆ polysulfide catholyte, stoichiometric amounts of elemental sulfur and anhydrous sodium sulfide powder were mixed in electrolyte comprised of 1.5 M NaClO₄ and 0.2 M NaNO₃ in TEGDME to maintain the sulfur concentration of 1.5 M, 3 M, and 4.5 M sulfur (S). The mixture was heated at 50-60 °C and stirred continuously for 20 h inside the argon-filled glove box (Lab Star, Mbraun). Finally, a dark brown solution of Na₂S₆ polysulfide catholyte was obtained for experimental use.

2.3.3 Preparation of Na-alg wrapped MnO₂ Nanoarrays Decorated Carbon Cloth

In order to prepare sodium-alginate wrapped MnO₂-decorated carbon cloth, MnO₂ nanoarrays with an optimized areal loading of 0.5 mg cm⁻² were first grown on a carbon cloth (W0S1002) following our previous report². Briefly, a piece of carbon cloth (6 cm × 6 cm) was first washed with 10% aqueous HNO₃ solution and later with DI water. The washed carbon cloth was then dried and transferred into an autoclave containing an aqueous solution of KMnO₄. The Teflon-sealed autoclave was then heated at 150 °C for 12 h. After completion of the hydrothermal reaction, the autoclave was cooled down to room-temperature. The hydrothermal-treated carbon cloth was then washed with DI water and acetone for multiple times and subsequently dried at 70 °C under vacuum for 24 h. The MnO₂ decorated carbon cloth is designated as CC@MnO₂. However, the dried CC@MnO₂ substrate was cut into circular disks of 12 mm diameter for further treatment to uniformly wrap with sodium-alginate nanofibers. 50 mg of sodium-alginate (Sigma-Aldrich) was first dissolved into 10 ml of de-ionized water. The circular disks of CC@MnO₂ substrate were then dipped into the aqueous solution of sodium-alginate and freeze dried. The sodium-alginate wrapped CC@MnO₂ substrate is designated and further referred as CC@MnO₂@Na-alg. The average loading of sodium-alginate on CC@MnO₂@Na-alg substrate was estimated to be 0.3 mg cm⁻².

2.3.4 Preparation of activated carbon cloth

Activated carbon cloth (ACC) was prepared through chemical treatment of a commercially available pristine carbon cloth as reported previously^{3,4}. The as purchased carbon cloth (W0S1002) was washed thoroughly with diluted HNO₃ and dried at 70 °C. The washed carbon cloth was subsequently soaked with 2 M NaOH aqueous solution. The NaOH soaked carbon cloth was then

transferred to a high temperature tube furnace and heated at 800 °C for 1h under an inert atmosphere. After the chemical treatment, the activated carbon cloth was removed from the furnace and washed with DI water to remove all residual side products. After successful preparation, the treated carbon cloth was dried for 24 h at 70 °C under vacuum.

2.3.5 Preparation of activated carbon cloth decorated with indium-tin-oxide (ACC@ITO)

Activated carbon cloth decorated with tin-doped indium-oxide nanoparticle (ACC@ITO) was prepared through solvothermal method followed by heat treatment at 1000 °C in an argon atmosphere as reported previously^{3,4}. As obtained carbon cloth (W0S1002) was washed carefully with diluted HNO₃ and dried at 70 °C. This washed carbon cloth fiber was used as a substrate to grow tin-doped indium-oxide nanoparticles on it. ITO nanoparticle synthesized on carbon fiber in an autoclave by the solvothermal method as described in the literature. Washed carbon cloth (8 cm × 4 cm) was kept inside the Teflon-lined autoclave against the wall. Indium chloride (InCl₃) and tin chloride (SnCl₄) as In³⁺ and Sn⁴⁺ ion precursors are dissolved in 1,4-butanediol. The molar ratio of indium and tin precursors was fixed at 85:15. Then this solution was transferred into the Teflon-lined stainless-steel autoclave and bolted to sealed it. The bolted autoclave kept at 200 °C for 24 h in a muffle furnace and then cooled down to room temperature. After the solvothermal reaction, carbon cloth was taken out from the autoclave and transferred to the tubular furnace and was further heated at 1000 °C for 1 h in an argon atmosphere. The nanoparticle of ITO was grown on activated carbon cloth uniformly which we called CC@ITO. Subsequently, CC@ITO was cut as round disks with a diameter of 12 cm which was used as a polysulfide reservoir in RT Na-S battery.

2.4 Cell Assembly

2.4.1 Coin cell assembly for CC@MnO₂@Na₂S₆ cathode

The CC@MnO₂ matrix was cut into the disks of 12 mm diameter and used as an active material host. To keep areal sulfur loading = 1.7 mg_(S) cm⁻², the 40 μL of 1.5M Na₂S₆ catholyte was then added dropwise into those CC@MnO₂ disks and allowed to be soaked. The Na₂S₆ soaked CC@MnO₂ disks were then used as cathodes to fabricate Na-S cells. The CC@MnO₂ electrodes soaked with Na₂S₆ are designated and further referred to as CC@MnO₂@Na₂S₆. To assemble a CR 2032 coin cell, CC@MnO₂@Na₂S₆ cathode was placed with respect to sodium metal anode.

Polypropylene membrane (GELON LIB Co. Ltd., PR China) was incorporated as a separator in between cathode and anode.

2.4.2 Coin cell assembly for CC@MnO₂@Na₂S₆@Na-alginate cathode

The Na || polypropylene membrane || CC@MnO₂@Na₂S₆ cells (CR 2032 coin cells) were assembled in an argon-filled glove box, where H₂O and O₂ both <0.5 ppm were maintained. First, Na₂S₆ polysulfide catholyte was drop cast into the CC@MnO₂@Na-alginate polysulfide reservoir. To keep areal sulfur loading = 3.4 mg_(S) cm⁻², the 40 μL of 3.0 M Na₂S₆ catholyte was then added dropwise into those CC@MnO₂ disks and allowed to be soaked. Then, porous polypropylene membrane (GELON LIB Co. Ltd., PRChina) as a separator was placed on the top of the CC@MnO₂@Na₂S₆@Na-alginate electrode. After the addition of 20 μL base electrolyte on top of the separator, the sodium metal foil was placed on the separator. In the end, the coin cell was cramped and sealed inside the argon-filled glove box (Lab star, MBraun) with water and oxygen content of < 0.5 and 0.5 ppm, respectively.

2.4.3 Coin cell assembly for ACC@ Na₂S₆ cathode

The activated carbon cloth (ACC) was cut into circular disks of 12 mm diameter. 40 μL of Na₂S₆ catholyte containing 3 M concentration of atomic sulfur (S) was then incorporated dropwise into each ACC disk and allowed to soak fully. The Na₂S₆ soaked ACC disks (Na₂S₆@ACC) were used as cathodes with respect to a sodium metal anode in the RT Na-S batteries. A polypropylene membrane (GELON LIB Co. Ltd., PR China) was used as separator between cathode and anode.

2.4.4 Coin cell assembly for ACC@ITO@ Na₂S₆ cathode

The activated carbon cloth decorated with tin-doped indium-oxide nanoparticle (ACC@ITO) was cut into the circular disks of 12 mm diameter. To load 5.1 mg cm⁻² of sulfur, 40 μL of Na₂S₆ catholyte comprising 4.5 M concentration of atomic sulfur (S) was then loaded dropwise into each ACC@ITO disk and permitted to be soaked appropriately. The Na₂S₆ soaked ACC@ITO disks (ACC@ITO@ Na₂S₆) were used as cathodes with respect to sodium metal anode in the RT Na-S batteries. Polypropylene membrane was used as separator in between cathode and anode.

2.5 Experimental Techniques

2.5.1 Materials characterizations

The microstructure and morphology of the samples were examined using a field-emission gun scanning electron microscope (FEG-SEM; JEOL-7600F) and field-emission gun transmission electron microscope (FEG-TEM, JEOL-2100F). Elemental mapping of the samples was examined through energy-dispersive X-ray spectroscopy (EDS) associated with FEG-SEM. Electron spin resonance (ESR) spectra of the activated carbon cloths and the catholytes were recorded on an ESR spectrometer (JEOL, JES-FA200) with X-band working at a microwave frequency of 9.447 GHz. To examine the nature of interactions between intermediate products and the sulfur hosts, X-ray photoelectron spectrometer (Kratos Analytical, AXIS Supra) was utilized.

2.5.2 Electrochemical measurements

As a preliminary electrochemical characterization tool, the cyclic voltammetry (CV) experiment was carried out between 1.2 and 2.6 V at a scan rate of 0.1 mV s^{-1} on a Biologic VMP-3. Galvanostatic charge-discharge cyclic performances of cells were carried out on an Arbin instrument (BT2000, USA). The cell was galvanostatically charged and discharged within the potential range of 1.2–2.45 V vs Na^+/Na . All the electrochemical tests were performed at $20 \text{ }^\circ\text{C} \pm 2^\circ\text{C}$.

2.5.3 XPS analysis

X-ray photoelectron spectroscopy (XPS) technique was employed to investigate the interaction between sulfur species and MnO_2 . First, two different catholyte, Na_2S_6 , and Na_2S_4 were synthesized separately by mixing the prerequisite amounts of sulfur and anhydrous sodium sulfide into the electrolyte, containing 1.5 M NaClO_4 and 0.2 M NaNO_3 . Then both the catholyte were soaked into two different manganese dioxide decorated carbon cloth substrates separately. Both Mn 2p and S2p XPS spectra were recorded. To investigate the nature of interactions and their mechanism between intermediate products and the sulfur hosts(ACC), X-ray photoelectron spectrometer (Kratos Analytical, AXIS Supra) was utilized. The XPS spectra were collected by probing the surface of the cathode before and after cycling and subsequently deconvoluted and fitted using the XPS software. The XPS curves were deconvoluted and fitted using Casa XPS processing software.

2.5.4 *In-situ* Raman characterization and analysis

In order to investigate the generation of polysulfide radical anions and the change of their concentration during the discharge process, *in-situ* Raman experiments were performed and analyzed. To perform the *in-situ* Raman experiment, a regular coin cell was modified accordingly. An optical window was prepared at the cathode side and sealed with transparent adhesive tape. Raman spectra were recorded using a laser Raman spectrometer (Horiba Jobin Yvon) with an excitation wavelength of 532 nm. During the *in-situ* Raman experiment, the Na-S cell was discharged from its OCV (~ 2.12 V) to 1.60 V at a scan rate of 0.02 mV s^{-1} . Each Raman spectrum was obtained with an exposure time of 30 s. During the acquisition of each Raman spectrum, the cell potential was held constant through the chronoamperometry technique.

2.5.5 ESR spectroscopy

Electron spin resonance (ESR) spectra of the pristine carbon cloth, activated carbon cloths, and the catholyte was recorded on an ESR spectrometer (JEOL, JES-FA200) with X-band operating at a microwave frequency of 9.447 GHz. The samples were loaded into a quartz tube, inside an argon-filled glove box. In order to identify the ESR resonance of the samples, the magnetic field was swept repeatedly for 20 sweeps.

2.5.6 Computational details

Theoretical calculations based on density functional theory (DFT) were carried out with the Gaussian 09 package⁵. The geometry optimization for sodium-alginate and various order polysulfides (Na_2S_8 , Na_2S_6 , Na_2S_4 , Na_2S_2 and Na_2S), generated at different depth of discharge have been performed using Becke's hybrid three-parameter nonlocal exchange functional combined with the Lee-Yang-Parr gradient corrected correlation functional (B3LYP) along with the 6-31G(d,p) basis set⁶⁻⁹. The optimized geometries for all the structures with the lowest energy were considered as the ground state and further used for polysulfide (PS) adsorption studies. All calculations including Grimme's dispersion corrections were carried out using a locally modified version of the Gaussian 09 program (IOP(3/124=3)¹⁰⁻¹². In order to understand the charge distribution over sodium-alginate as well as PS adsorbed structure, the electron density mapping (with electrostatic potential (ESP)) and Mulliken charge distribution analysis have been carried out respectively.

The binding energies were calculated by the following equation:

$$E_B = (E_{S/PS} - E_S - E_{PS})$$

where, E_S , E_{PS} , and $E_{S/PS}$ are the ground state energies of sodium-alginate (S), polysulfide (PS) molecules and PS adsorbed sodium-alginate (S/PS) systems, respectively.

References:

1. D. Guo, X. Yu, W. Shi, Y. Luo, Q. Li, T. Wang, *J. Mater. Chem. A* 2014, 2, 8833.
2. Kumar, A., Ghosh, A., Roy, A., Panda, M.R., Forsyth, M., MacFarlane, D. R., and Mitra, S. *Energy Storage Mater.* 2019, 20, 196–202. 3.
3. M. A. Lillo-Rodenas, D. Cazorla-Amoros and A. Linares-Solano, *Carbon*, 2003, 41, 267.
4. S.-H. Yoon, S. Lim, Y. Song, Y. Ota, W. Qiao, A. Tanaka and I. Mochida, *Carbon*, 2004, 42, 1723.
5. Ayoko, G. A. (2018). *RSC Adv.* 2018, 8, 2271–2279.
6. Lee, C., Yang, W., and Parr, R. G. *Phys. Rev. B* 1988, 37, 785–789.
7. Hay, P. J., and Wadt, W. R. *J. Chem. Phys.* 1985, 82, 270–283.
8. Becke, A. D. *J. Chem. Phys.* 1993, 98, 5648.
9. Stephens, P. J., Devlin, F. J., Chabalowski, C. F., and Frisch, M. J. *J. Phys. Chem.* 1994, 98, 11623–11627.
10. Grimme, S. *J. Comput. Chem.* 2004, 25, 1463–1473.
11. Grimme, S. *J. Comput. Chem.* 2006, 27, 1787–1799.
12. Osuna, S., Swart, M., and Solà, M. *J. Phys. Chem. A* 2011, 115, 3491–3496.

Chapter 3

High-energy density room temperature sodium-sulfur battery enabled by
sodium polysulfide catholyte and carbon cloth current collector
decorated with MnO₂ nanoarrays

Chapter 3

3.1. Introduction

Sulfur is one of the promising cathode materials for rechargeable battery application¹⁻². However, as mentioned earlier in chapter 1 that the higher-order sodium polysulfide intermediates (Na_2S_n , $4 \leq n \leq 8$) formed during charge-discharge are soluble in typically-used electrolytes³⁻²⁵. These polysulfides can “shuttle” to sodium metal anode, causing lower utilization of active material, fast capacity decay and deterioration of the anode¹⁰. Physical confinement of sulfur in a microporous carbon matrix was found to improve the electronic conductivity as well as to provide physical reservoirs of polysulfides^{3-9,11-18,21,23,24}. Although, owing to the hydrophobic surface of carbon and the higher solvation energy of long-chain polysulfides, intermediate polysulfides still tend to diffuse into the electrolyte. Therefore, a sulfur host which can offer strong chemical interaction sites for polysulfides, along with a stable conductive network, is desirable to improve the overall performance of RT Na-S batteries.

Herein, we introduce a cathode scaffold consisting of MnO_2 nanoneedle arrays on flexible carbon cloth (CC@MnO_2) and demonstrated for the as a multifunctional polysulfide reservoir to enhance the energy density and prolong the cycle life of RT Na-S batteries. Sodium polysulfide (Na_2S_6) catholyte was used and incorporated as an active material into the flexible CC@MnO_2 substrate. The cathode architectures containing polysulfide catholyte as active material and porous carbon current collector were previously demonstrated and showed improved performance in Li-S battery systems²⁵⁻²⁹. Liquid phase catholyte has the tendency of facile dispersion and homogeneous distribution on conductive matrix and thus could facilitate higher utilization of sulfur. The use of carbon cloth as current collector can significantly enhance the electronic conduction throughout cathode scaffold and thus improve the active material utilization. To immobilize and retain the soluble intermediates into the cathode scaffold, an array of MnO_2 nanoneedles as “sulfiphilic matrix”³⁰ has been decorated on the surface of carbon. The strong affinity of CC@MnO_2 substrate for the soluble higher-order sodium polysulfides (Na_2S_n , $4 \leq n \leq 8$) could impede the shuttling phenomenon and accelerate complete conversion of sulfur to lower-ordered polysulfides.

Moreover, the large surface area of MnO_2 nanoneedle arrays might afford the continuous deposition of electrolyte-insoluble lower-order sodium polysulfides (Na_2S_n , $1 \leq n \leq 3$) during discharge³⁰. The RT Na-S batteries, containing Na_2S_6 catholyte incorporated CC@MnO_2 substrate

as cathodes, exhibit high initial specific capacity, slow capacity decay and excellent rate capability. At 0.2 A g⁻¹ current, our RT Na-S batteries deliver an initial reversible capacity of 938 mA h g⁻¹, which ensures a high initial energy density of 946 W h kg⁻¹. The RT Na-S batteries retain the reversible capacity up to 610 mA h g⁻¹ (corresponding to the energy density of 728 W h kg⁻¹) after 500 cycles.

3.2. Results and discussion

3.2.1. Synthesis and characterization

To prepare sodium-polysulfide adsorbed MnO₂-decorated carbon cloth (CC@MnO₂) as a freestanding cathode, MnO₂ nanoarrays were first grown on the surface of carbon cloth via a facile hydrothermal process in the presence of KMnO₄³¹. The flexible carbon cloth was selected as both substrate and current collector in this study, owing to its excellent mechanical strength and electronic conductivity. The carbon cloth (CC) not only serves as a substrate for MnO₂ growth, but also acts as a reducing agent to reduce KMnO₄ to MnO₂, producing uniform deposition of MnO₂ on the surface of the carbon fibres. After successful synthesis of CC@MnO₂, the sodium polysulfide (Na₂S₆) catholyte was incorporated drop wise and allowed to adsorb. The Na₂S₆ catholyte-adsorbed CC@MnO₂ substrate (i.e., CC@MnO₂@Na₂S₆) was then directly used as the cathode in RT Na-S batteries. The schematic illustration of synthesis of CC@MnO₂@Na₂S₆ cathode is shown in Figure 3.1.

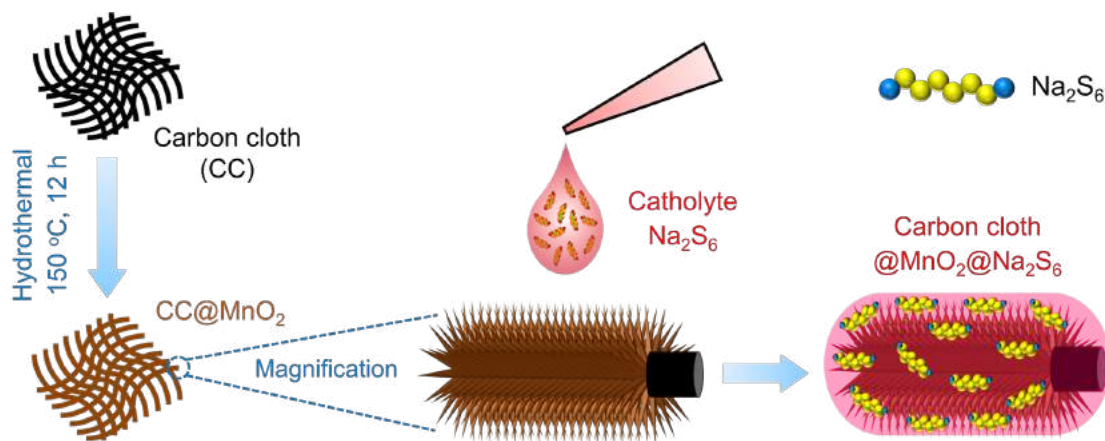


Figure 3.1: Schematic of the preparation of CC@MnO₂@Na₂S₆ cathode for room temperature sodium-sulfur batteries.

The microstructure and surface morphology of the CC@MnO₂ substrate were investigated. SEM images of CC@MnO₂ (Figure 3.2 a–c) reveal that the MnO₂ nanoneedles are uniformly distributed at high density on the surface of the CC fibers. The XRD pattern of CC@MnO₂ (Figure 3.2d) exhibits all the peaks characteristic of both CC and δ -MnO₂ (JCPDS no. 18-802). The TEM image of CC@MnO₂ shows strong adhesion of the MnO₂ nanoneedles to the carbon cloth, even after ultrasonication in isopropyl alcohol (Figure 3.2e). Figure 3.2f shows a high-resolution TEM image of MnO₂, showing well-resolved lattice fringes separated by 0.24 nm, corresponding to the (006) plane of δ -MnO₂.

3.2.2. Electrochemical performances of RT Na-S batteries

The CC@MnO₂ substrate soaked with Na₂S₆ catholyte (i.e., CC@MnO₂@Na₂S₆) was used as the free-standing cathode, along with a sodium anode, in RT Na-S coin cells. After fabrication, the cell was in an intermediate state of charge, with an open circuit potential (OCP) of 2.23 V; it could then have been either fully charged or discharged first. In this study, the Na-S cell was first fully

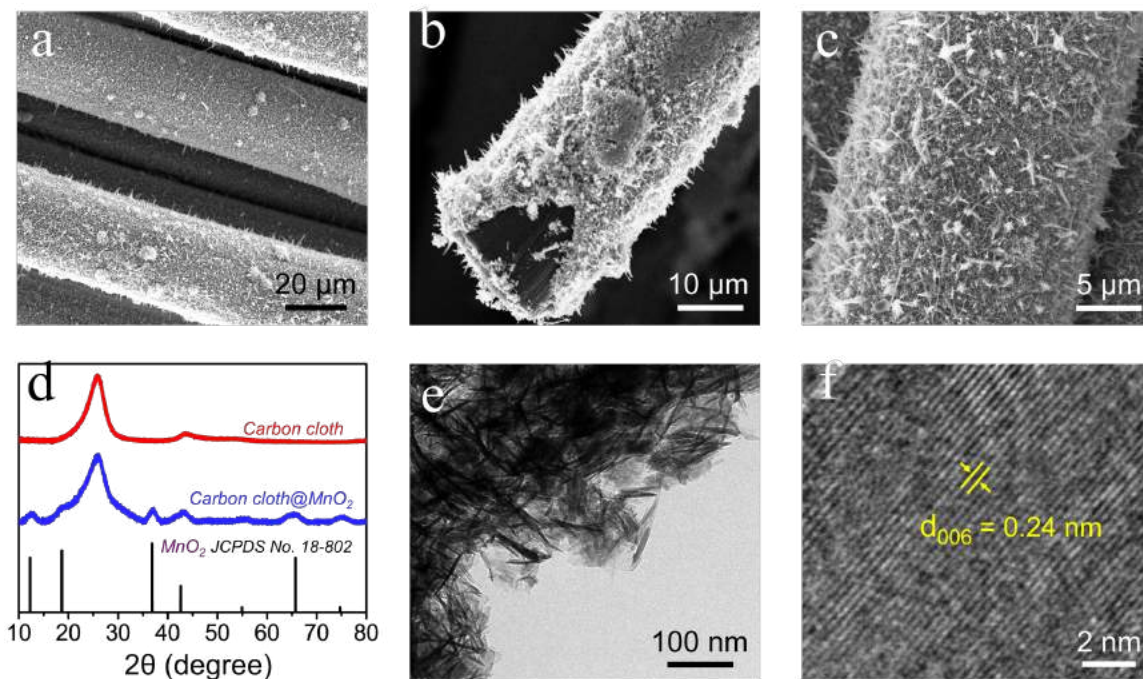


Figure 3.2: (a–c) SEM images of CC@MnO₂ at different magnifications. (d) XRD patterns of bare carbon cloth and CC@MnO₂. Low-resolution TEM image (e) and high-resolution TEM image (f) of CC@MnO₂ substrate.

discharged to complete the reduction reaction. Figure 3.3a shows the cyclic voltammograms of CC@MnO₂@Na₂S₆ cathode over the initial 10 cycles. During the initial discharge, the cell exhibited a small weak peak at 1.95 V, followed by an intense peak at 1.65 V. The weak peak at 1.95 could be ascribed to a liquid–liquid transition from Na₂S₆ to middle-order sodium polysulfides, Na₂S₄ ³². The following peak at 1.65 V is corresponding to the complete reduction of Na₂S₄ to lower-order sodium polysulfides (Na₂S_n, 1 ≤ n ≤ 3). On changing the sweep direction, two distinguishable anodic peaks were obtained at 1.9 V and 2.4 V. The first anodic peak at 1.9 V indicates the oxidation of lower-order polysulfides to higher-order sodium polysulfides (Na₂S_n, 4

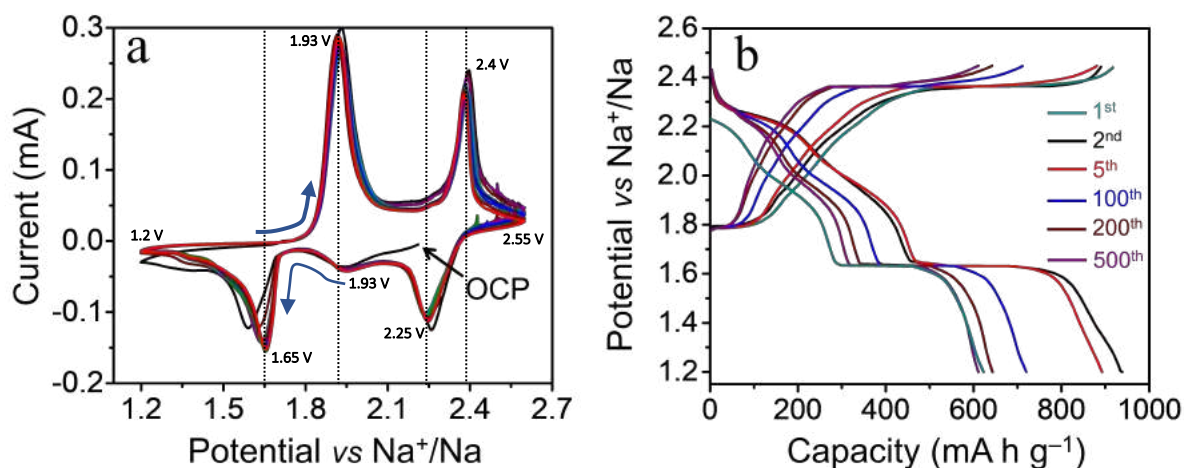


Figure 3.3: (a) Cyclic voltammograms of the cell for the initial ten cycles, within 1.2–2.6 V at a scan rate of 0.1 mV s⁻¹. (b) Voltage versus charge-discharge capacity profiles of the cathode CC@0.5MnO₂@Na₂S₆ (MnO₂ loading 0.5 mg cm⁻²) at 0.2 A g⁻¹ at 20°C ± 2°C.

≤ n ≤ 8); while the following anodic peak at 2.4 V corresponds to the oxidation of higher-order sodium polysulfides to elemental sulfur (S₈). During the second cathodic scan, the cell exhibited an intense reduction peaks at 2.2 V indicates the reduction of S₈ to higher order polysulfides (Na₂S_n; 4 ≤ n ≤ 8) and again 1.67 V corresponds to the complete reduction of Na₂S₄ to lower-order sodium polysulfides (Na₂S_n, 1 ≤ n ≤ 3). From the second cycle onwards, both the peak positions and areas of the two pairs of cathodic and anodic peaks remain constant, indicating completely reversible sodiation/de-sodiation processes in the cell. Further charge-discharge cycling experiments were carried out within an active potential window of 1.2–2.45 V vs Na⁺/Na. Figure 3.3b illustrates the charge-discharge profiles of CC@MnO₂@Na₂S₆ cathode with MnO₂ areal loading of 0.5 mg cm⁻²

² for different cycles at a current of 0.2 A g^{-1} . A large mismatch between the specific capacities obtained during initial discharge process and subsequent charge process was observed. This phenomenon may be because our starting material (i.e., Na_2S_6) was already in sodiated form. However, after the first charge-discharge cycle, the Na-S cell exhibited two distinct discharge plateaus at 2.25 V and 1.65 V, exactly corresponding to the positions of the two

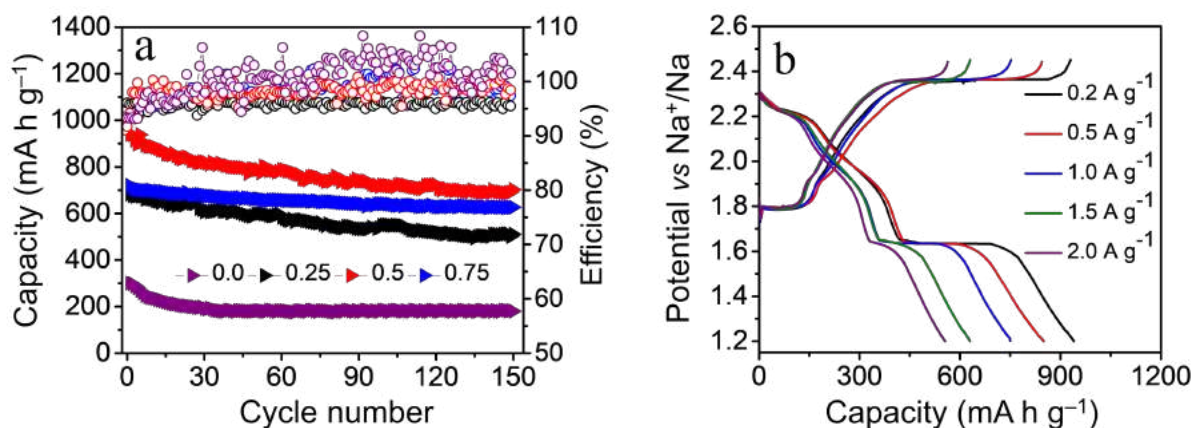


Figure 3.4: (a) Discharge capacity and Coulombic efficiency versus cycle number of $\text{CC@Na}_2\text{S}_6$ (violet = without MnO_2), and $\text{CC@MnO}_2\text{@Na}_2\text{S}_6$ (MnO_2 loadings: black = 0.25, red = 0.5 and blue = 0.75 mg cm^{-2}) cathodes. (b) Voltage versus charge-discharge capacity profiles of the cathode $\text{CC@MnO}_2\text{@Na}_2\text{S}_6$ (MnO_2 loading 0.5 mg cm^{-2}) at different currents at $20^\circ\text{C} \pm 2^\circ\text{C}$.

reduction peaks observed during the cathodic CV scans. Maintaining the identical areal mass of sulfur, the $\text{CC@MnO}_2\text{@Na}_2\text{S}_6$ cathodes with different MnO_2 areal loadings were cycled at 0.2 A g^{-1} and the cyclic performances are shown in Figure 3.4a. The cathode scaffold without MnO_2 loading (i.e., $\text{CC@Na}_2\text{S}_6$) showed lowest average specific capacity of 195 mA h g^{-1} during cycling. The $\text{CC@MnO}_2\text{@Na}_2\text{S}_6$ cathode with MnO_2 loading of 0.5 mg cm^{-2} delivered the highest specific capacity during cycling, an initial reversible specific capacity of 938 mA h g^{-1} at the second cycle and a capacity of 708 mA h g^{-1} was retained after 150 cycles, indicating an optimized cycling behaviour. However, to investigate the rate capability of the optimized cathode structure (i.e., $\text{CC@0.5MnO}_2\text{@Na}_2\text{S}_6$); the cell was cycled at different current rates. The charge-discharge profiles of the $\text{CC@0.5MnO}_2\text{@Na}_2\text{S}_6$ cathode at 0.2 A g^{-1} , 0.5 A g^{-1} , 1 A g^{-1} , 1.5 A g^{-1} and 2 A g^{-1} , respectively, are shown in Figure 3.4b. Figure 3.5a shows the corresponding specific capacities

at the different current rates. High average specific capacities were recorded: 930 mA h g⁻¹ (@0.2 A g⁻¹), 845 mA h g⁻¹ (@0.5 A g⁻¹), 750 mA h g⁻¹ (@1 A g⁻¹), 630 mA h g⁻¹ (@1.5 A g⁻¹) and 555 mA h g⁻¹ (@2 A g⁻¹).

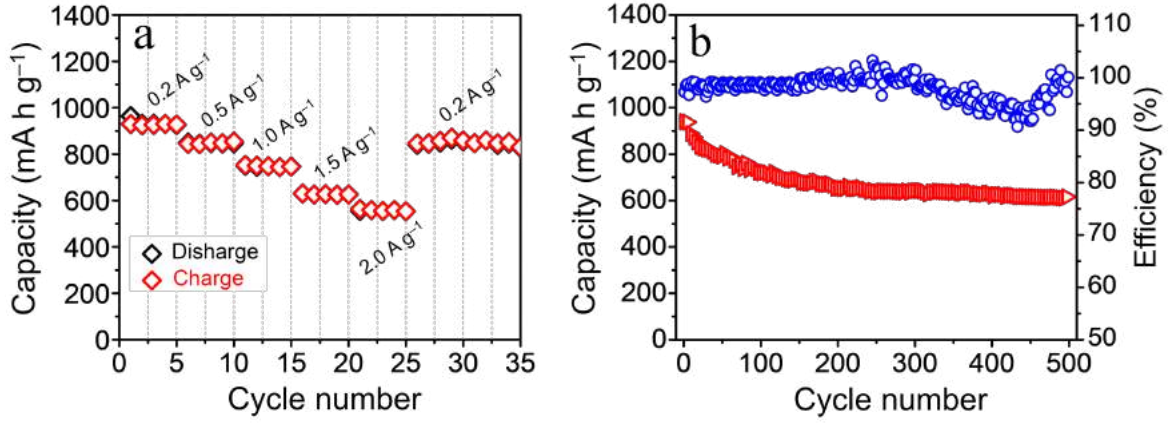


Figure 3.5: (a) Performances of CC@MnO₂@Na₂S₆ cathode at different currents. (b) Discharge capacity and Coulombic efficiency versus cycle number of CC@MnO₂@Na₂S₆ (MnO₂ loading 0.5 mg cm⁻²) at the current rate of 0.2 A g⁻¹ at 20°C ± 2°C.

When the current was reversed to 0.2 A g⁻¹, the CC@0.5MnO₂@Na₂S₆ cathode retained 89.2% of its initial capacity, implying that the CC@0.5MnO₂@Na₂S₆ cathode is robust in Na-S batteries. Figure 3.5b shows the results of an extended cycling test on the CC@0.5MnO₂@Na₂S₆ cathode, which maintained 67% of the initial capacity after 500 cycles. It is notable that during cycling, the rate of capacity decay was slightly high (0.15% per cycle) for initial 200 cycles. However, the reversible specific capacity appeared to be reaching very stable value after 200 cycles. The cell exhibited a reversible specific capacity of 654 mA h g⁻¹ at 200th cycle and maintained a capacity of 609 mA h g⁻¹ up to 500 cycles, with an average capacity fading of 0.023% per cycle. Operating at a high average potential of 1.82 V (Figure 3.6), the Na-S cells delivered the energy density of 946 W h kg⁻¹ at second cycle, 881 W h kg⁻¹ at 20th cycle.

Figure 3.6 shows the 20th cycle discharge profile of a CC@MnO₂@Na₂S₆ cathode at 0.2 A g⁻¹.

$$\int_{Q_1}^{Q_2} dQ = \text{discharge capacity} = 828 \text{ mA h g}^{-1}, \int_{Q_1}^{Q_2} V dQ = \text{discharge energy} = 1506 \text{ W h kg}^{-1}.$$

Therefore, the average potential is estimated to be 1.82 V (Using eqn. in section 1.4.2.)

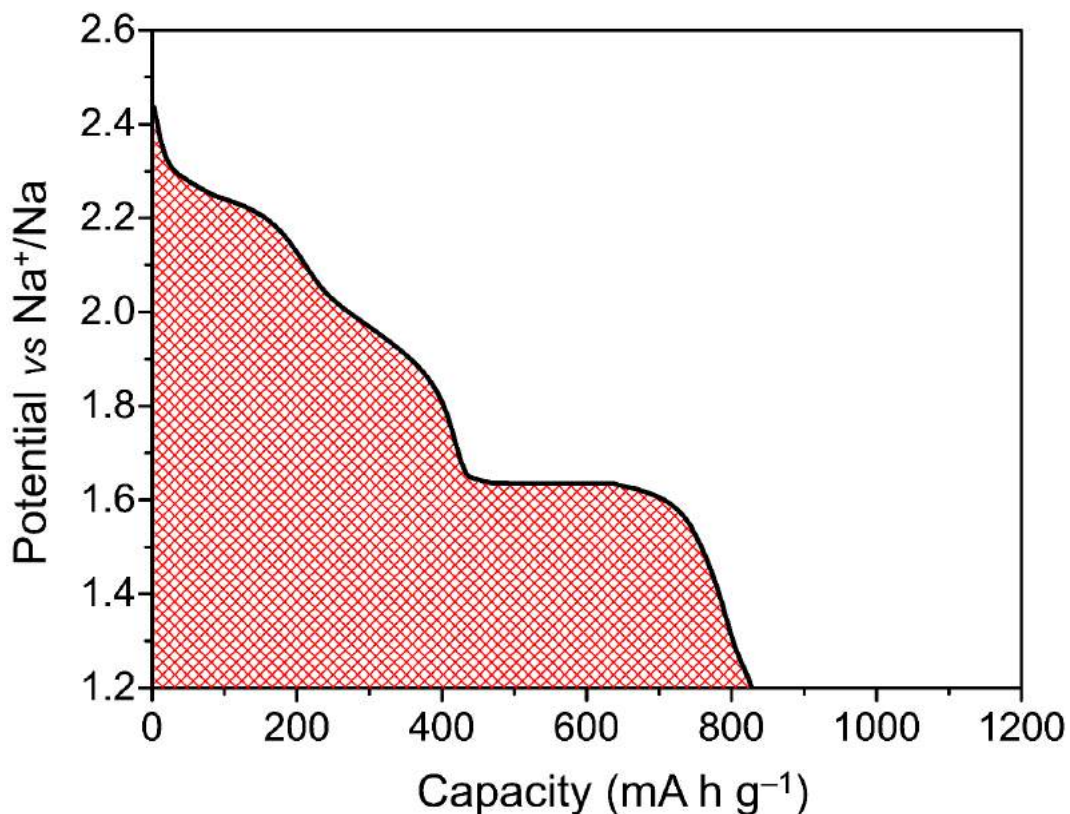


Figure 3.6. Discharge profile of 20th cycle for CC@MnO₂@Na₂S₆ cathode at 200 mA g⁻¹.

3.2.3. Probing the mechanism of the interaction between sodium polysulfides and MnO₂ through X-ray photoelectron spectroscopy

The interactions between MnO₂ and intermediate sodium polysulfides were examined using Mn2p and S2p XPS analyses. The best-performing cathode substrate, CC@0.5MnO₂ was used for these XPS studies. Both Na₂S₄ and Na₂S₆ were examined as examples of typical intermediate discharge products, which are prone to dissolve in the electrolyte. The XPS results and fits are shown in Figure 3.7. Figure 3.7a presents the Mn 2p_{3/2} XPS spectra of CC@MnO₂, CC@0.5MnO₂@Na₂S₄ and CC@0.5MnO₂@Na₂S₆. The Mn2p_{3/2} XPS spectrum of CC@0.5MnO₂ shows a strong peak at a binding energy of 642.5 eV, corresponding to Mn⁴⁺ and a small peak at 641.5 eV, related to a smaller amount of reduced Mn(O)OH compound with a Mn³⁺ redox center³³. Along with these two characteristic peaks, a satellite peak can also be observed at a higher binding energy of 643.8 eV³⁰.

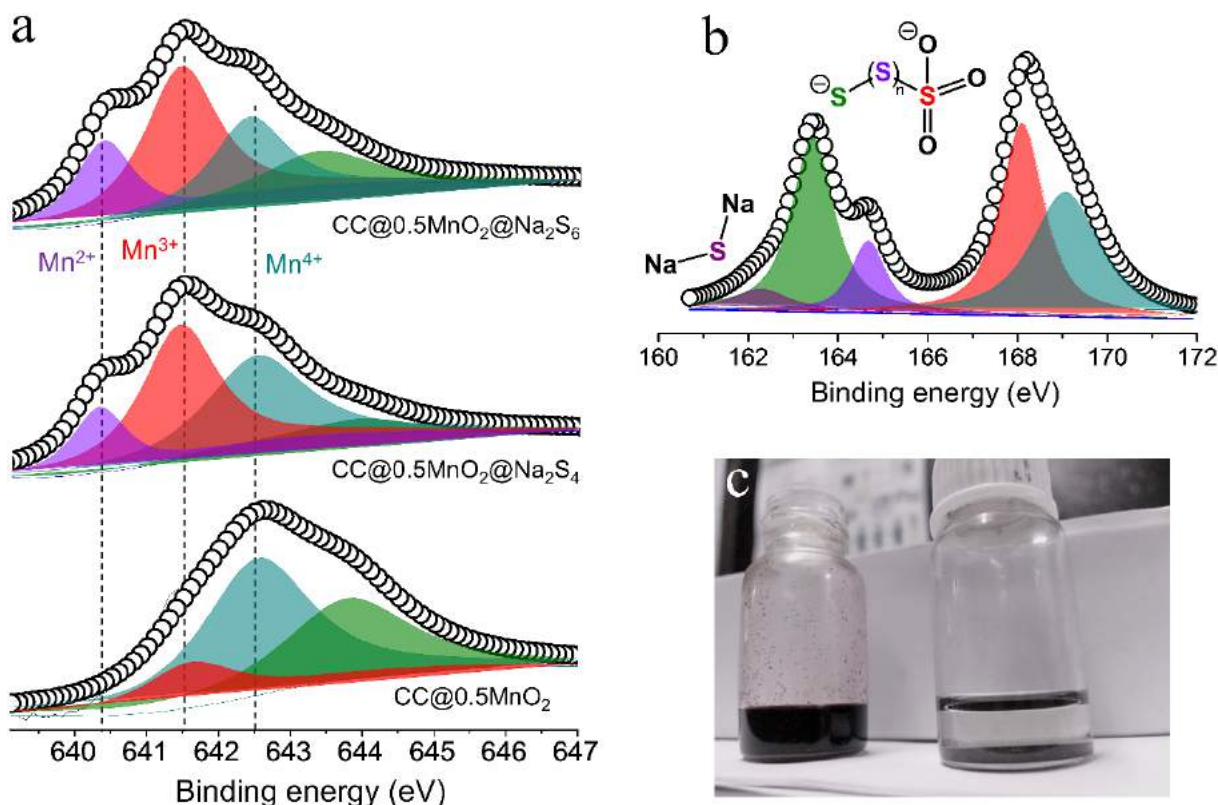


Figure 3.7: (a) Mn 2p_{3/2} spectra of CC@0.5MnO₂, CC@0.5MnO₂@Na₂S₄, and CC@0.5MnO₂@Na₂S₆ specimens. (b) S 2p_{3/2} spectrum of CC@0.5MnO₂@Na₂S₆ sample. (c) Photograph of loss of color of polysulfide solution upon addition of MnO₂, indicating “entrapment” of polysulfides on the metal oxide surface.

The Mn 2p_{3/2} spectra of both CC@0.5MnO₂@Na₂S₄ and CC@0.5MnO₂@Na₂S₆ samples indicate that after incorporation of sodium polysulfide solutions, the contribution from Mn³⁺ was found to be significantly enhanced and a new peak centered at 640.4 eV, ascribed to Mn²⁺ appeared^{30,33}. The enhancement of intensity related to Mn³⁺ and the appearance of the new peak corresponding to Mn²⁺ suggest that there is not only dipole-induced electrostatic interaction between MnO₂ and Na₂S_n, but that a surface redox reaction also occurs, where Mn⁴⁺ is reduced by Na₂S_n. However, to confirm our prediction, an S2p_{3/2} XPS spectrum was also collected for CC@0.5MnO₂@Na₂S₆, as shown in figure 3.7b. The S2p_{3/2} XPS spectrum contains five peaks, centered at different binding energies, implying five different sulfur environments. The most intense peak, at binding energy of

168.0 eV, corresponds to the central (or S=O) sulfur of thiosulfate ($\text{S}_2\text{O}_3^{2-}$) groups present in polythionate complexes, which may arise from a surface

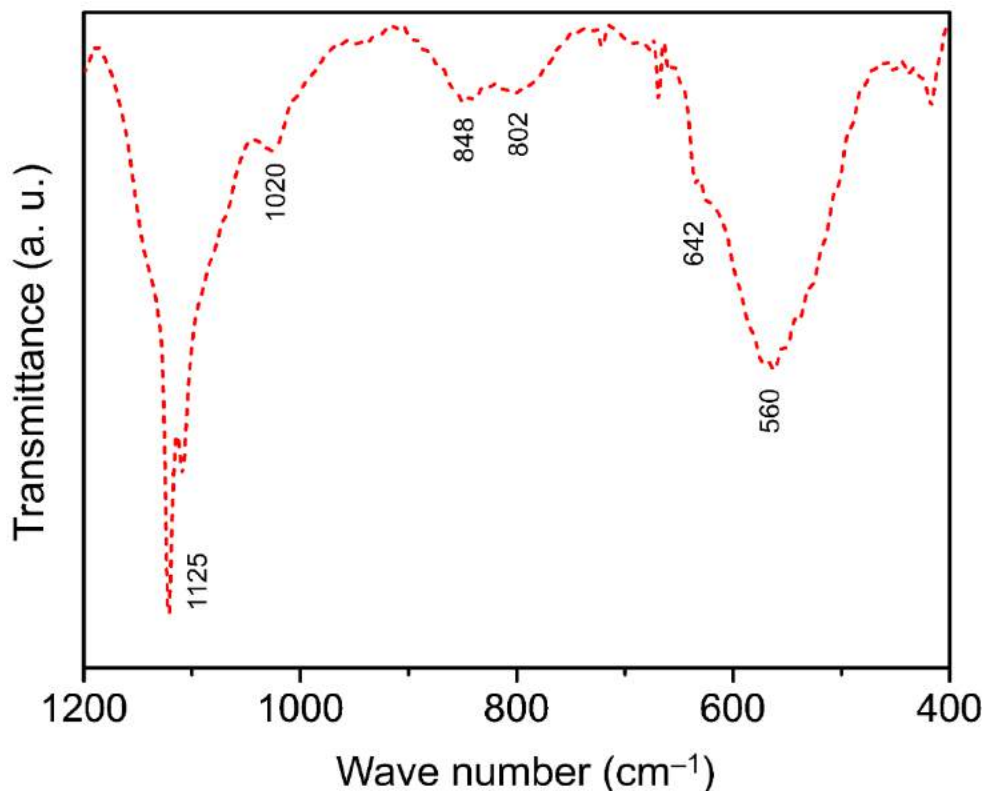


Figure 3.8: FTIR spectrum of Na_2S_6 adsorbed MnO_2 sample.

redox reaction between Na_2S_6 and MnO_2 ^{30,34}. The peaks at 164.6 and 163.5 eV are associated with the bridging sulfur(s) and terminal sulfur, respectively. All the bridging sulfur(s) in a polythionate complex can be considered identical, because they reside in a similar electronic environment. The peak at 162.2 eV can be attributed to the formation of Na_2S , while the peak at 169.0 eV is due to air-oxidized sulfur species. The formation of polythionate complexes containing thiosulfate group is also proven by Fourier transform infrared spectroscopy (FTIR) recorded on Na_2S_6 adsorbed MnO_2 sample. The FTIR spectrum (Figure 3.8) exhibits the characteristic peaks of $\text{S}_2\text{O}_3^{2-}$ at 642, 1020 and 1125 cm^{-1} as well as the characteristic bands of Mn–O bonds at 560, 802 and 848 cm^{-1} ³⁵. The presence of $\text{S}_2\text{O}_3^{2-}$ group proves the formation of polythionate complexes during the chemical reaction between MnO_2 and sodium polysulfide. The Mn 2p_{3/2} and S2p_{3/2} XPS results supported with FTIR spectrum are consistent with the previously-reported “lithium polysulfide (Li_2S_n)– MnO_2 interaction” described by Nazar et al. [30].

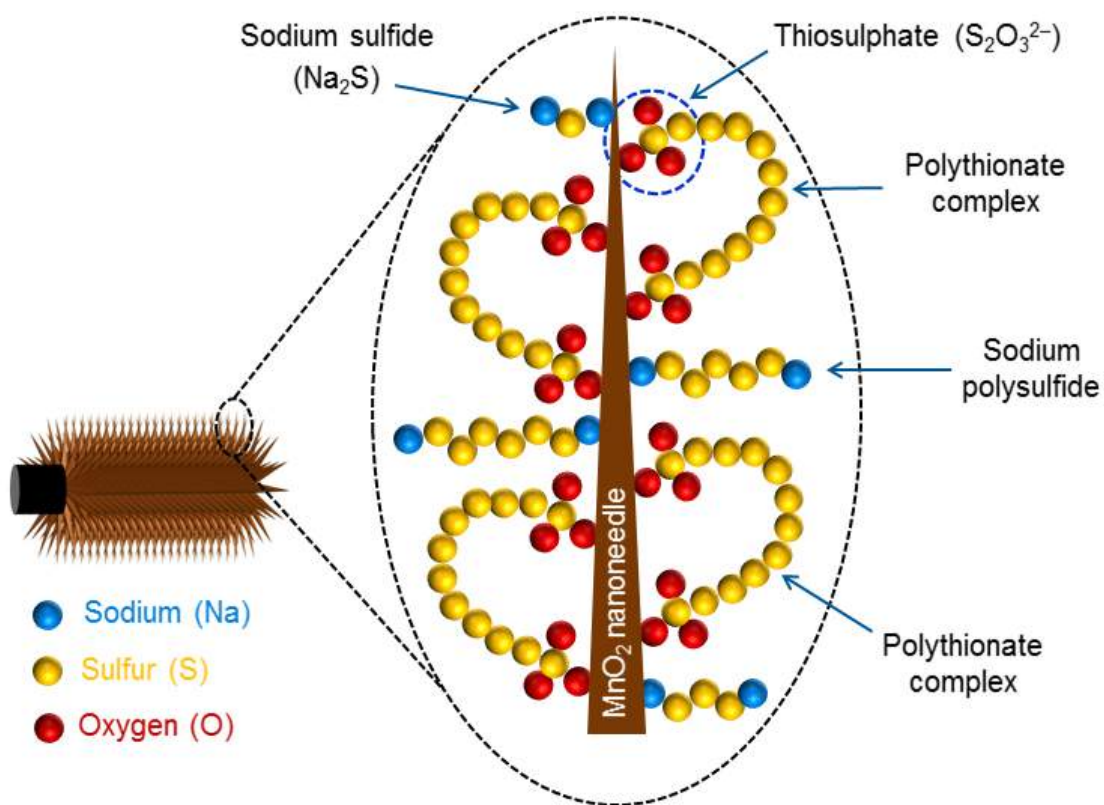


Figure 3.9: Schematic representation of the possible interactions of manganese oxide with different sodium polysulfides and polythionate complexes.

Briefly, the thiosulfate ($\text{S}_2\text{O}_3^{2-}$) group is first produced through surface oxidation of polysulfide (S_n^{2-}) by MnO_2 , with reduction of Mn^{4+} to Mn^{3+} and Mn^{2+} . The as-formed $\text{S}_2\text{O}_3^{2-}$ groups then behave as linkers to anchor the soluble, higher-order polysulfides from the electrolyte and convert them into less-soluble lower-order polysulfides. Therefore, the $\text{S}_2\text{O}_3^{2-}$ groups not only restrict the polysulfide dissolution, but also help convert intermediate discharge products to end-discharge products. Both these mechanisms lead to high energy density and improved cycle life. The interactions of MnO_2 with different polysulfides and polythionate complexes are schematically shown in Figure 3.9.

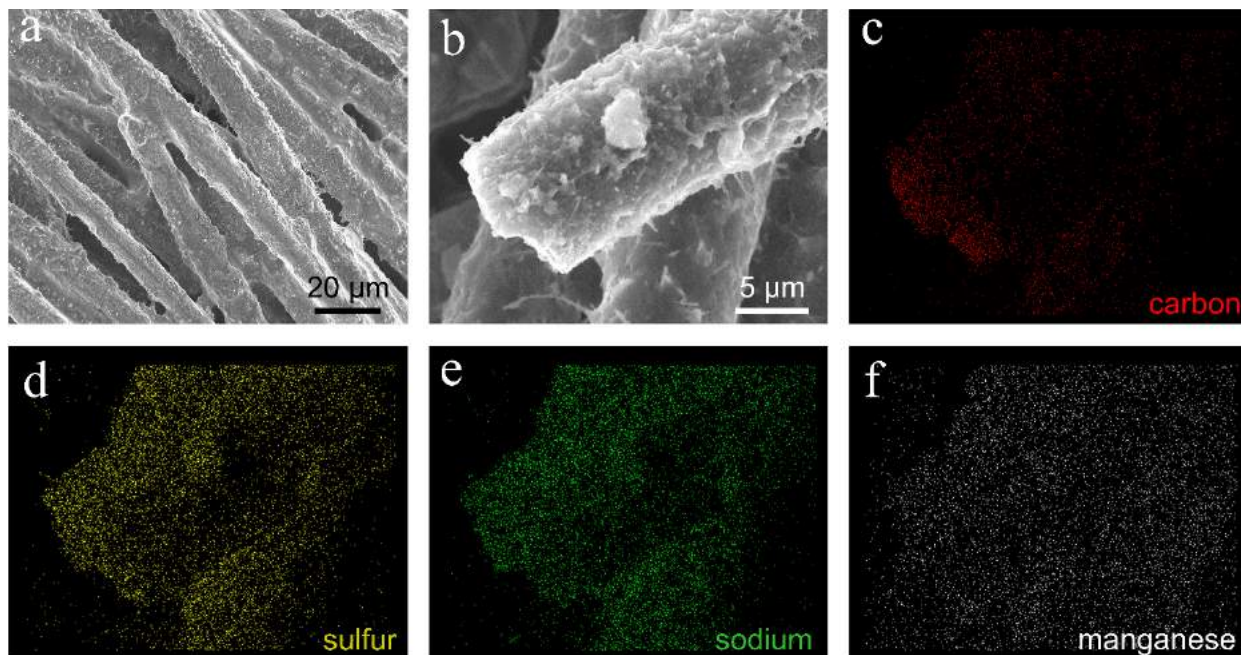


Figure 3.10: Post-mortem analyses of $\text{CC}@0.5\text{MnO}_2@\text{Na}_2\text{S}_6$ cathode after 150 cycles, at fully discharged state: low-resolution SEM image (a) and high-resolution SEM image (b) of cycled electrode. (c–f) Carbon, sulfur, sodium and manganese mapping on the cycled $\text{CC}@0.5\text{MnO}_2@\text{Na}_2\text{S}_6$ cathode.

3.2.4. Post-cycling analysis of Na-S cell after charge-discharge

To better understand the polysulfide adsorption efficacy of MnO_2 during cycling, the morphologies of the cathode and anode were examined with ex-situ scanning electron microscopy. Figure 3.10a is the SEM image of the $\text{CC}@0.5\text{MnO}_2@\text{Na}_2\text{S}_6$ cathode after 150 cycles, at fully discharged state. The carbon fibers remain intact, implying that the high mechanical integrity of carbon cloth helps to maintain the original structure of the $\text{CC}@0.5\text{MnO}_2@\text{Na}_2\text{S}_6$ cathode, even after prolonged charge-discharge processes. From the high-resolution SEM image, it is interesting to note that the surface of $\text{CC}@0.5\text{MnO}_2$ substrate was covered with dense discharged products (Figure 3.10b and Figure 3.11), indicating a high retention of active material even after extensive cycles.

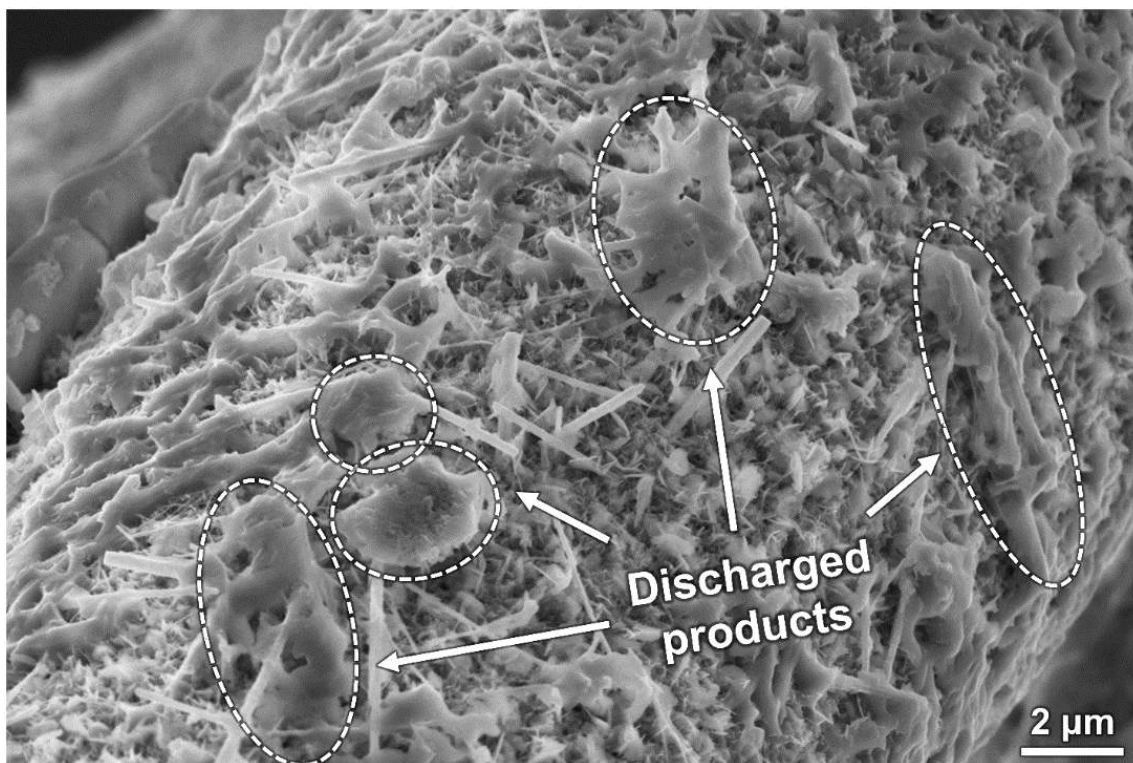


Figure 3.11: Ex-situ high-resolution SEM image of CC@0.5MnO₂@Na₂S₆ cathode after 150 cycles, at fully discharged state, showing a good adhesion of discharged products on the surface of CC@0.5MnO₂ substrate.

The sulfur and sodium mappings (Figure 3.10d & e) confirmed that the discharge products were homogeneously distributed on the surface of the CC@0.5MnO₂ substrate, where they are presumably attached through strong interaction with the surfaces of the MnO₂ nanoneedles, suggesting an excellent affinity towards discharge products.

Furthermore, the final discharged products observed on the surface of CC@0.5MnO₂ substrate was characterized through X-ray diffraction technique. The XRD pattern of CC@0.5MnO₂@Na₂S₆ cathode after 150 cycles, at fully discharged state (Figure 3.12), shows appearance of new peaks which could be assigned to the lower-order sodium polysulfides (i.e., Na₂S_n, 1 ≤ n ≤ 3) ³⁶.

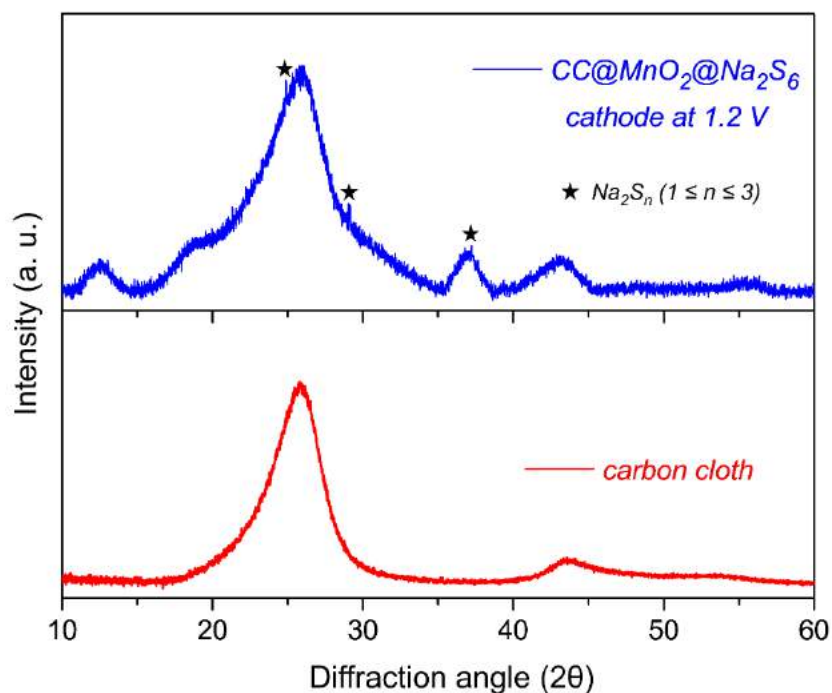


Figure 3.12: XRD patterns of pristine carbon cloth and $\text{CC@0.5MnO}_2\text{@Na}_2\text{S}_6$ cathode after 150 cycles, at fully discharged state. The appearance of the new peaks (marked with asterisks) seem to be appeared from insoluble lower-order sodium polysulfides (Na_2S_n , $1 \leq n \leq 3$) deposited on the surface of CC@0.5MnO_2 substrate.

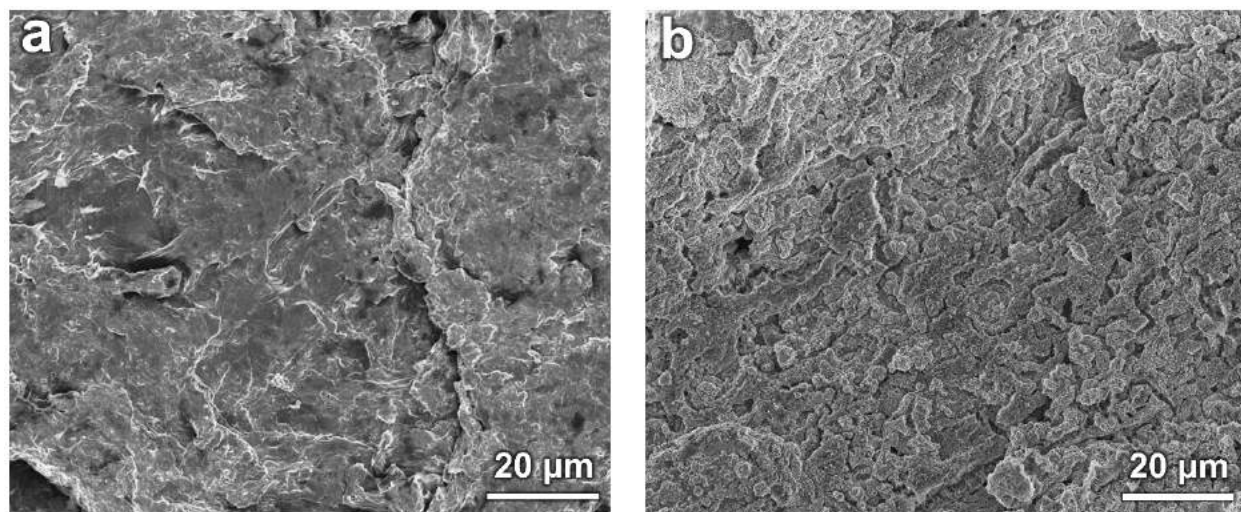


Figure 3.13: Ex-situ SEM images of the surfaces of sodium metal anode placed towards (a) $\text{CC@0.5MnO}_2\text{@Na}_2\text{S}_6$ cathode and (b) $\text{CC@Na}_2\text{S}_6$ cathode after 150 cycles.

To further understand the benefits of CC@MnO₂ substrate in terms of reduced shuttle behavior, the morphologies of cycled sodium metal anode surfaces with respect to CC@Na₂S₆ and CC@0.5MnO₂@Na₂S₆ cathodes were investigated. The ex-situ SEM images of the cycled sodium metal surfaces placed towards CC@0.5MnO₂@Na₂S₆ and CC@Na₂S₆ cathodes are shown in Figure 3.13. Apart from some cracks, the sodium anode placed towards the CC@0.5MnO₂@Na₂S₆ cathode exhibited a smooth surface. On contrary, the surface of metallic sodium against the CC@Na₂S₆ cathode became severely rough after cycling. This observation could be attributed to the fact that in Na-S cell, containing the cathode without MnO₂ polysulfide reservoirs, the as-formed polysulfides were not effectively trapped into the cathode scaffold. The soluble polysulfides then diffuse towards anode and chemically react with bare surface of sodium. However, in the CC@MnO₂@Na₂S₆ cathode, due to an effective confinement of the intermediates, the extent of potentially detrimental chemical reaction between sodium metal and Na₂S_n was lower, leading to comparatively smooth surface of sodium anode.

3.3 Conclusions

A high energy-density room-temperature Na-S battery has been practically realized by incorporating a CC@MnO₂ substrate containing Na₂S₆ catholyte as an efficient multifunctional cathode. The Na-S cell offered an initial energy density of 946 W h kg⁻¹, and retained 728 W h kg⁻¹ after 500 cycles. The mechanism of interaction between MnO₂ and intermediate products was investigated through XPS, which revealed *in-situ* formation of polythionate complexes through disproportionation reactions of higher-order polysulfides in the presence of thiosulfate surface species. The polythionate complexes anchored the polysulfides, restricting their rapid dissolution. We believe that the concept of employing a sodium polysulfide catholyte as active material, and CC@MnO₂ as both an electronically conductive substrate and a polysulfide reservoir, could encourage practical realization of room temperature sodium-sulfur batteries with high energy output.

References

1. B. Dunn, H. Kamath, J. M. Tarascon, *Science* 2011, 334, 928.
2. X. Lu, G. Xia, J. P. Lemmon, Z. Yang, *J. Power Sources* 2010, 195, 2431.
3. C.W. Park, J. H. Ahn, H.S. Ryu, K. W. Kim, H. J. Ahn, *Electrochem. Solid-State Lett.* 2006, 9, A123.
4. S. Wenzel, H. Metelmann, C. Reiß, C., A. K. Dürr, J. Janek, P. Adelhelm, *J. Power Sources*. 2013, 243, 758.
5. S. Xin, Y. X. Yin, Y. G. Guo, L. J. Wan, *Adv. Mater.* 2014, 26, 1261.
6. X. Yu, A. Manthiram, *J. Phys. Chem. C* 2014, 118, 22952.
7. I. Bauer, M. Kohl, H. Althues, S. Kaskel, *Chem. Commun.* 2014, 50, 3208.
8. X. Yu, A. Manthiram, *Adv. Energy Mater.* 2015, 5, 1500350.
9. X. Yu, A. Manthiram, *Chem. Eur. J.* 2015, 21, 4233.
10. A. Manthiram, X. Yu, *Small* 2015, 11, 2108.
11. I. Kim, J. Y. Park, C. H. Kim, J. W. Park, J. P. Ahn, J. H. Ahn, K.W. Kim, H.J. Ahn, *J. Power Sources* 2016, 301, 332.
12. I. Kim, C. H. Kim, S. H. Choi, J. P. Ahn, J. H. Ahn, K. W. Kim, E. J. Cairns, H. J. Ahn, *J. Power Sources* 2016, 307, 31.
13. S. Wei, S. Xu, A. Agrawal, S. Choudhury, Y. Lu, Z. Tu, L. Ma, L. A. Archer, *Nat. Commun.* 2016, 7, 11722.
14. Y.-X. Wang, J. Yang, W. Lai, S.-L. Chou, Q.-F. Gu, H. K. Liu, D. Zhao, S. X. Dou, *J. Am. Chem. Soc.* 2016, 138, 16576.
15. I. Kim, J. Y. Park, C.H. Kim, J. W. Park, J. P. Ahn, J. H. Ahn, K. W. Kim, H. J. Ahn, *J. Electrochem. Soc.* 2016, 163, 611.
16. X. Yu, A. Manthiram, *Chem. Mater.* 2016, 28, 896.
17. Y. M. Chen, W. Liang, S. Li, F. Zou, S. M. Bhaway, Z. Qiang, M. Gao, B. D. Vogt, Y. Zhu, *J. Mater. Chem. A* 2016, 4, 12471.
18. Z. Qiang, Y. M. Chen, Y. Xia, W. Liang, Y. Zhu, B. D. Vogt, *Nano Energy* 2017, 32, 59.
19. L. Fan, R. Ma, Y. Yang, S. Chen B. Lu, *Nano Energy* 2016, 28, 304.
20. Y.-X. Wang, B. Zhang, W. Lai, Y. Xu, S.-L. Chou, H.-K. Liu, S.-X. Dou, *Adv. Energy Mater.* 2017, 7, 1602829.
21. R. Carter, L. Oakes, A. Douglas, N. Muralidharan, A. P. Cohn, C. L. Pint, *Nano Lett.* 2017, 17, 1863.

22. A. Ghosh, S. Shukla, M. Monisha, A. Kumar, B. Lochab S. Mitra, *ACS Energy Lett.* 2017, 2, 2478.
23. S. Gope, D. K. Singh, M. Eswaramoorthy, A. J. Bhattacharyya, *ChemistrySelect* 2017, 2, 9249.
24. Y. Hao, X. Li, X. Sun, C. Wang, *ChemistrySelect* 2017, 2, 9425.
25. H. J. Peng, W. T. Xu, L. Zhu, D. W. Wang, J. Q. Huang, X. B. Cheng, Z. Yuan, F. Wei, Q. Zhang, *Adv. Energy Mater.* 2016, 26, 6351.
26. H. J. Peng, J. Q. Huang, X. Y. Liu, X. B. Cheng, W. T. Xu, C. Z. Zhao, F. Wei, Q. Zhang, *J. Am. Chem. Soc.* 2017, 139, 8458.
27. R. Xu, I. Belharouak, J. C. M. Li, X. Zhang, I. Bloom, J. Bareño, *Adv. Energy Mater.* 2013, 3, 833.
28. H. Jie, P. J. Q. Huang, Q. Zhang, *Chem. Soc. Rev.* 2017, 46, 5237.
29. D. Ma, Y. Li, J. Yang, H. Mi, S. Luo, L. Deng, C. Yan, M. Rauf, P. Zhang, X. Sun, X. Ren, J. Li, H. Zhang, *Adv. Funct. Mater.* 2018, 28, 1705537.
30. X. Liang, C. Hart, Q. Pang, A. Garsuch, T. Weiss, L. F. Nazar, *Nat. Commun.* 2015, 6, 5682.
31. D. Guo, X. Yu, W. Shi, Y. Luo, Q. Li, T. Wang, *J. Mater. Chem. A* 2014, 2, 8833.
32. X. Yu, A. Manthiram, *ChemElectroChem* 2014, 1, 1275.
33. H. W. Nesbitt, D. Banerjee, *Amer. Miner.* 1998, 83, 305.
34. B. J. Lindberg, K. Hamrin, G. Johansson, U. Gelius, A. Fahlman, C. Nordling, K. S. Lindberg, *Phys. Scr.* 1970, 1, 286.
35. F. Miller, C. Wilkins, *Anal. Chem.* 1952, 24, 1253.
36. I. Kim, J. Y. Park, C. Kim, J. W. Park, J. P. Ahn, J. H. Ahn, K. W. Kim, H. J. Ahn, *J. Electrochem. Soc.* 2016, 163, A611.

Chapter 4

A Robust Cathode Scaffold for Room-Temperature Sodium-Sulfur Batteries

Chapter 4

4.1. Introduction

Even though Na-S batteries have many advantages in terms of high capacity¹⁻², the RT Na-S batteries suffer from rapid capacity fading due to gradual dissolution of sodium-polysulfides (Na_2S_n , $4 \leq n \leq 8$) into the liquid electrolyte, poor electronic conductivity of active material and chance of cathode pulverization during insertion/extraction of bigger sized Na^+ ions into sulfur¹⁻²³. Several strategies have been reported to mitigate the aforementioned problems. However, the remedies for polysulfide dissolution in terms of physical confinement, strong chemical attachment (elaborated in detail in Chapter 3) are found to be effective and successful achievement of long-term cyclability for the RT Na-S batteries still persists in previous studies. One of the main reasons behind the short-term cyclability of RT Na-S batteries is electrode pulverization during repeated Na^+ ion insertion/extraction during cycling. We believe that to extend the life cycling of the RT Na-S batteries, it is important to design a multifunctional cathode with the following features: (1) essential continuous electronic conduction throughout the entire electrode, (2) availability of strong binding sites to effectively immobilize the intermediate polysulfides, (3) sufficient elasticity to buffer well against large volume change of the sulfur particles during repeated insertion/extraction of Na^+ ions.

In this chapter, we introduce an effective cathode scaffold consisting of sodium-alginate wrapped MnO_2 nanoarrays decorated carbon cloth ($\text{CC}@\text{MnO}_2@\text{Na-alg}$) and demonstrated as a multifunctional polysulfide reservoir to improve the energy density and extend the cycle life of the RT Na-S batteries. Here, the carbon cloth provides the necessary 3D electronic conductive pathway for the electrons. Where Na-alginate confine the polysulfides physically owing to its abundant anchoring sites, manganese dioxide chemically anchors the higher-order polysulfides and promotes their redox conversion through formation of the polythionate complexes²⁴. However, besides the poor electronic conductivity of the active material and polysulfide dissolution problems, another serious issue related to the conversion-based electrode materials is the tendency to be pulverized due to the catastrophic effect of large volume expansion/contraction of the sulfur particles during insertion/extraction of metal cations²⁵. Due to larger size of Na^+ ion, the stress induced in the electrode during repeated charge-discharge cycling becomes more severe in the RT Na-S batteries. It has been demonstrated that the polysaccharide binders containing electronegative polar functional groups could effectively interact with the active material in electrode and thus

provide sufficient mechanical integrity to maintain the steady attachment of sulfur with current collector during cycling^{26,27}. Therefore, considering this excellent mechanical feature, sodium-alginate (one of the biopolymers) has been incorporated as a binder in our cathode to avoid structural pulverization during volume change. Moreover, the polar oxygenic functional groups (i.e., $-\text{OH}$, $\text{C}-\text{O}-\text{C}$ and $-\text{COONa}$) present in sodium-alginate could further interact with the sodium-polysulfides to restrict their dissolution^{26–28}. The interaction between sodium-alginate and different sodium-polysulfides has been investigated through density functional theory (DFT) calculation. The possible anchoring sites in alginate molecule based on the electron donation property of the functional groups and the variation of the charge density upon polysulfide intake have been discussed thoroughly using theoretical simulation. Here we provide an effective strategy to design a mechanically robust electrodes for the next generation RT Na-S batteries.

4.2. Results and discussion

4.2.1. Synthesis and characterization

In order to prepare sodium-alginate wrapped MnO_2 nanoarrays decorated carbon cloth (i.e., $\text{CC}@\text{MnO}_2@\text{Na-alg}$) as a freestanding substrate, MnO_2 nanoarrays were first grown on the carbon cloth surface with an optimized loading of $0.5 \text{ mg MnO}_2 \text{ cm}^{-2}$ ²⁴. The MnO_2 nanoarrays decorated carbon cloth ($\text{CC}@\text{MnO}_2$) substrate was then immersed into an aqueous solution of sodium-alginate and subsequently freeze-dried to wrap with the sodium-alginate nanofibers. After successful preparation of the $\text{CC}@\text{MnO}_2@\text{Na-alg}$ substrate, Na_2S_6 catholyte was added dropwise and allowed to be adsorbed effectively. The Na_2S_6 catholyte adsorbed $\text{CC}@\text{MnO}_2@\text{Na-alg}$ ($\text{CC}@\text{MnO}_2@\text{Na}_2\text{S}_6@\text{Na-alg}$) was directly employed as cathode in the RT Na-S batteries. Figure 4.1 illustrates the preparation of the $\text{CC}@\text{MnO}_2@\text{Na}_2\text{S}_6@\text{Na-alg}$ cathode in stepwise manner. Microstructures and morphologies of the synthesized $\text{CC}@\text{MnO}_2$ and $\text{CC}@\text{MnO}_2@\text{Na-alg}$ were characterized using scanning electron microscopy (SEM) technique. The SEM images of the $\text{CC}@\text{MnO}_2$ confirms a conformal growth of highly dense MnO_2 nanoarrays on the surface of carbon cloth (Figure 4.2a-c). The highly ordered array of MnO_2 nano-needles on carbon cloth could be effective to immobilize and retain the catholyte into the cathode scaffold. Moreover, the high-resolution SEM image of the $\text{CC}@\text{MnO}_2$ reveals that the conformal MnO_2 nanoarrays creates plenty of 3D open spaces (Figure 4.2c), which could not only facilitate the electrolyte accessibility but also serve as a reservoir to accommodate a large amount of catholyte.

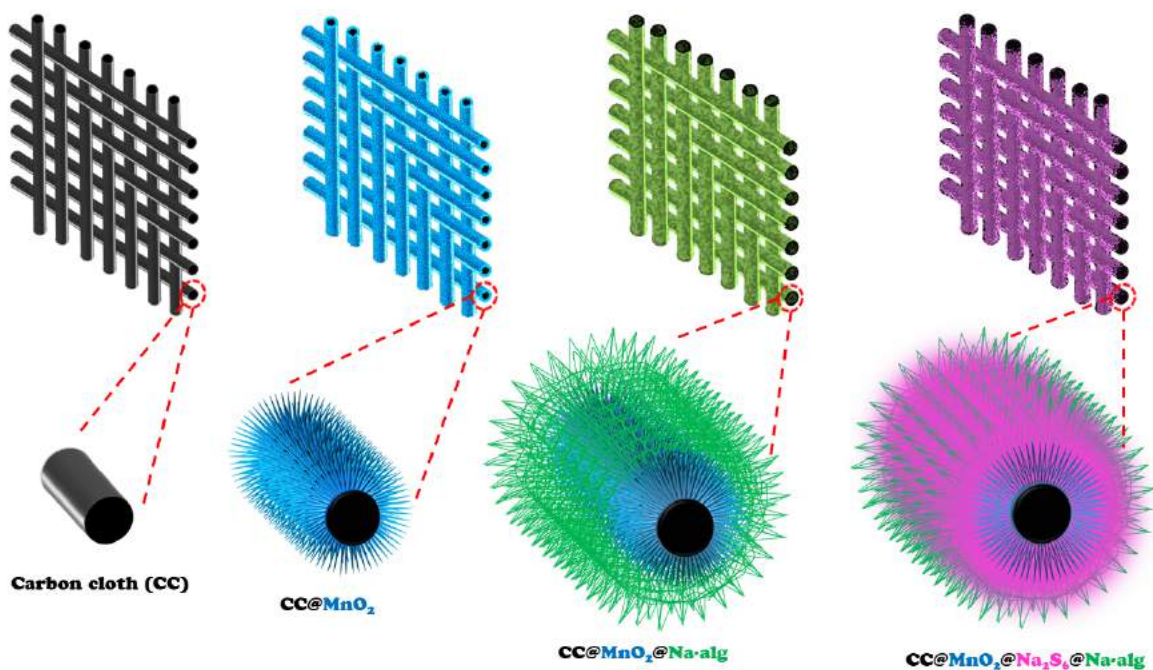


Figure 4.1: Schematic representation of $\text{CC@MnO}_2\text{@Na}_2\text{S}_6\text{@Na-alg}$ cathode preparation.

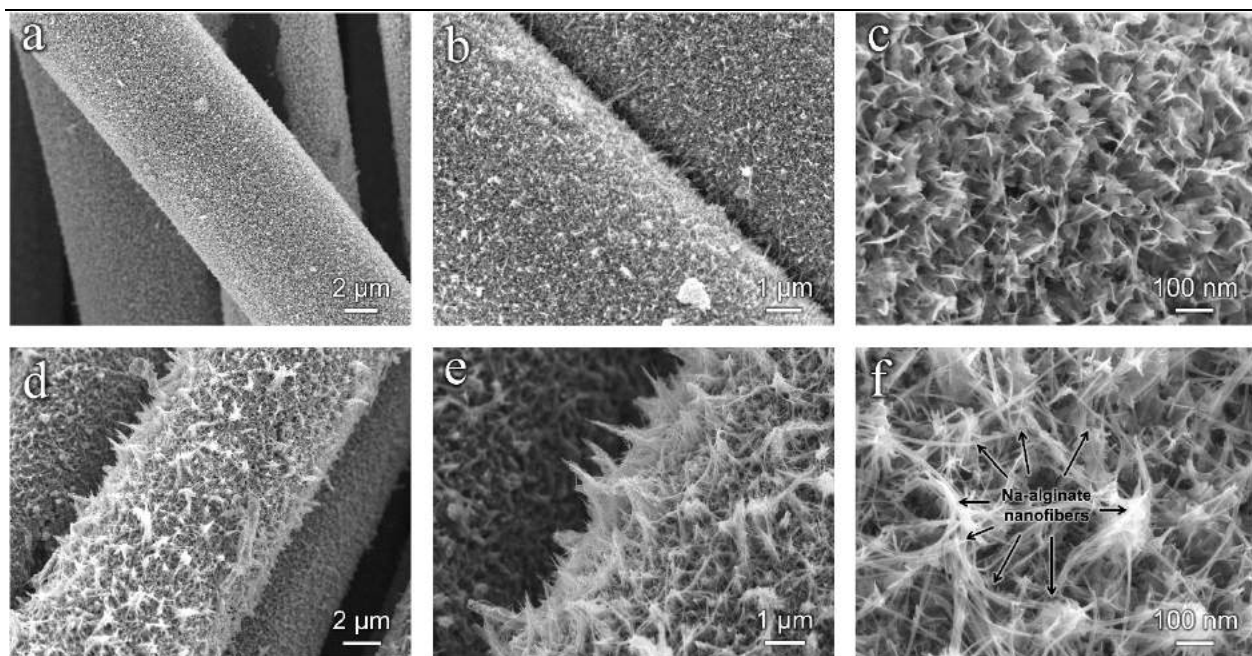


Figure 4.2: (a-c) SEM images of the CC@MnO_2 substrate at different magnifications; (d-f) SEM images of the $\text{CC@MnO}_2\text{@Na-alg}$ substrate at different magnifications.

Hence, the 3D open space not only offers a high loading of active material (catholyte) into the electrode, thus helping to increase the areal capacity of the RT Na-S batteries, but also serves as a buffer well against the large volume change of sulfur during cycling.

However, to enhance the mechanical properties of the MnO_2 nanoarrays further, a thin layer of sodium-alginate was coated over. The SEM images of $\text{CC@MnO}_2\text{@Na-alg}$ substrate exhibit a thin layer of sodium-alginate deposited on the surface of highly dense MnO_2 nanoarrays (Figure 4.2d–f). The high-resolution SEM image of the $\text{CC@MnO}_2\text{@Na-alg}$ indicates a homogeneous formation of sodium-alginate nanofibers (Figure 4.2f). The SEM image of $\text{CC@MnO}_2\text{@Na-alg}$ (Figure 4.3a) and the elemental mapping shows homogeneous coexistence of the constituent elements (i.e., Mn, Na and O) on the $\text{CC@MnO}_2\text{@Na-alg}$ substrate (Figure 4.3b–d). Sulfur loading has been estimated by using equivalent amount of Na_2S_6 catholyte.

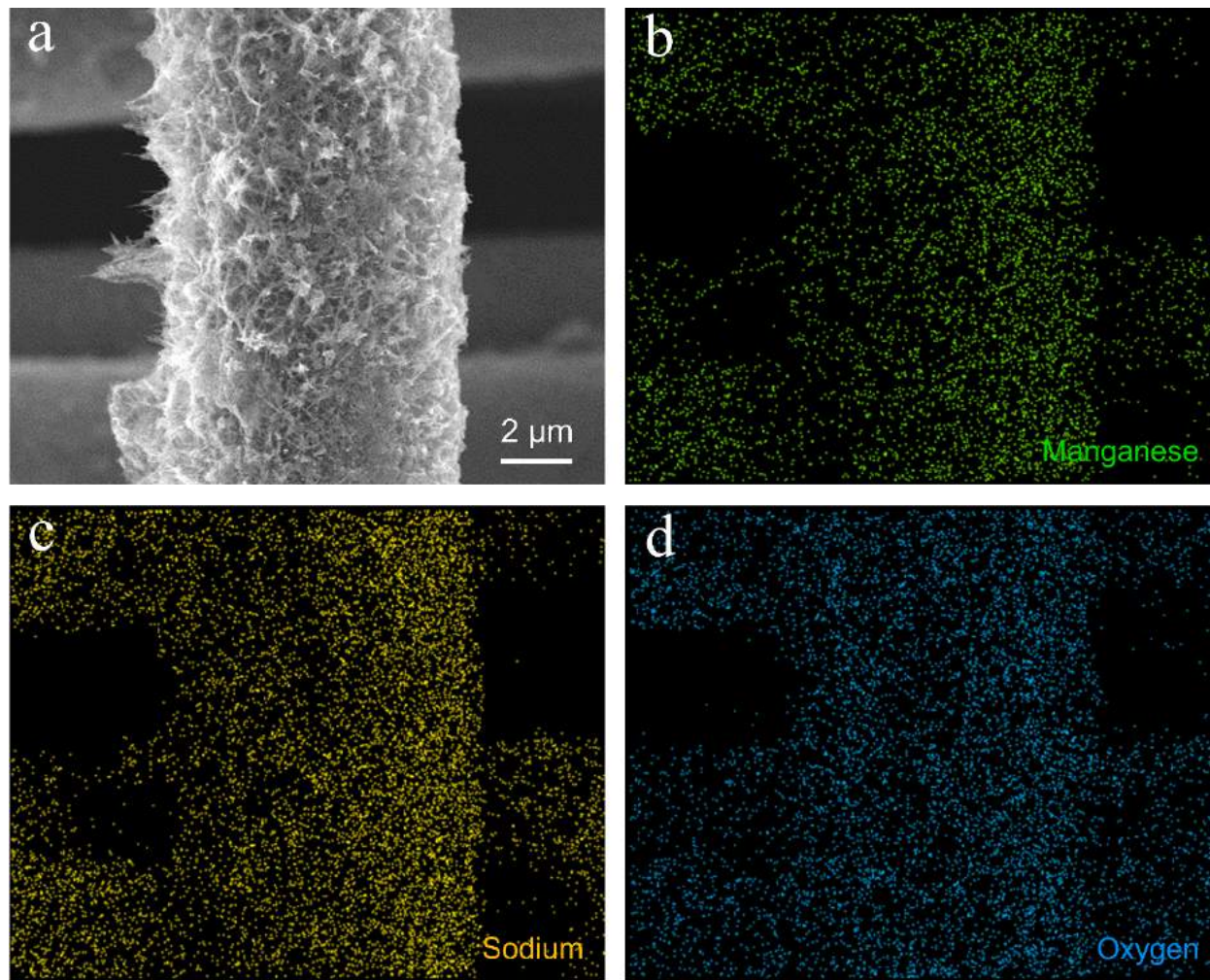


Figure 4.3: (a-d) Elemental mapping acquired on the $\text{CC@MnO}_2\text{@Na-alg}$ substrate.

4.2.2. Electrochemical performance

The electrochemical performance of the CC@MnO₂@Na₂S₆@Na-alg cathode has been evaluated with coin cells assembled using sodium metal as anode and reference. Figure 4.4a represents the CV curves of the CC@MnO₂@Na₂S₆@Na-alg cathode with sulfur loading of 1.7 mg cm⁻² at a scan rate of 0.1 mV s⁻¹. During the initial cathodic scan, the cell exhibited a small reduction peak at 1.95 V followed by an intense reduction peak at 1.67 V, corresponding to the stepwise reduction of Na₂S₆ to lower-order sodium polysulfides (Na₂S_n; 1 ≤ n ≤ 2)²⁴. However, during anodic scan reduction, two oxidation peaks were observed which could be attributed to the complete conversion of lower-order sodium polysulfides (Na₂S_n; 1 ≤ n ≤ 2) to elemental sulfur²⁴. During the CV scan, the unchanged shape and potential of the redox peaks reveal a facile sodiation/de-sodiation kinetics in the CC@MnO₂@Na₂S₆@Na-alg cathode. Figure 4.4b compares the second cycle discharge profiles of the CC@Na₂S₆ cathode, the CC@MnO₂@Na₂S₆ cathode and the CC@MnO₂@Na₂S₆@Na-alg cathode with sulfur loading of 1.7 mg cm⁻² at 0.2C rate respectively. The CC@Na₂S₆ cathode exhibits two small reduction plateaus during the discharge process, resulting in low specific capacity of around 300 mA h g⁻¹. In contrast, both the CC@MnO₂@Na₂S₆ and CC@MnO₂@Na₂S₆@Na-alg cathode exhibit two distinct and prominent discharge plateaus. Both the cathodes exhibit the first discharge plateau at an identical potential of 2.3 V (vs Na⁺/Na). However, it is interesting to note that the second discharge reaction plateau for the CC@MnO₂@Na₂S₆@Na-alg cathode appears at slightly higher potential and contributes to higher specific capacity in comparison with the CC@MnO₂@Na₂S₆ cathode, indicating a beneficial influence of sodium-alginate nanofibers to facilitate the redox conversion of middle-order sodium polysulfides to lower-order polysulfides. Figure 4.4c illustrates the charge-discharge profiles of the CC@MnO₂@Na₂S₆@Na-alg cathode (sulfur loading of 1.7 mg cm⁻²) at 0.2 C for the first, second and fifth cycles, respectively. A large amount of capacity mismatch between the specific capacity values obtained during the initial discharge process and subsequent charge process is attributed to pre-sodiated form of the starting material (i.e., Na₂S₆). However, after first cycle of charge-discharge the CC@MnO₂@Na₂S₆@Na-alg cathode exhibited two distinct discharge plateaus at 2.3 V and 1.67 V (vs Na⁺/Na) respectively, corresponding to two-steps reduction of sulfur to sodium sulfide. Each of the charge profiles for the CC@MnO₂@Na₂S₆@Na-alg cathode exhibits two prominent oxidation reaction plateaus at 1.8 V and 2.35 V, respectively.

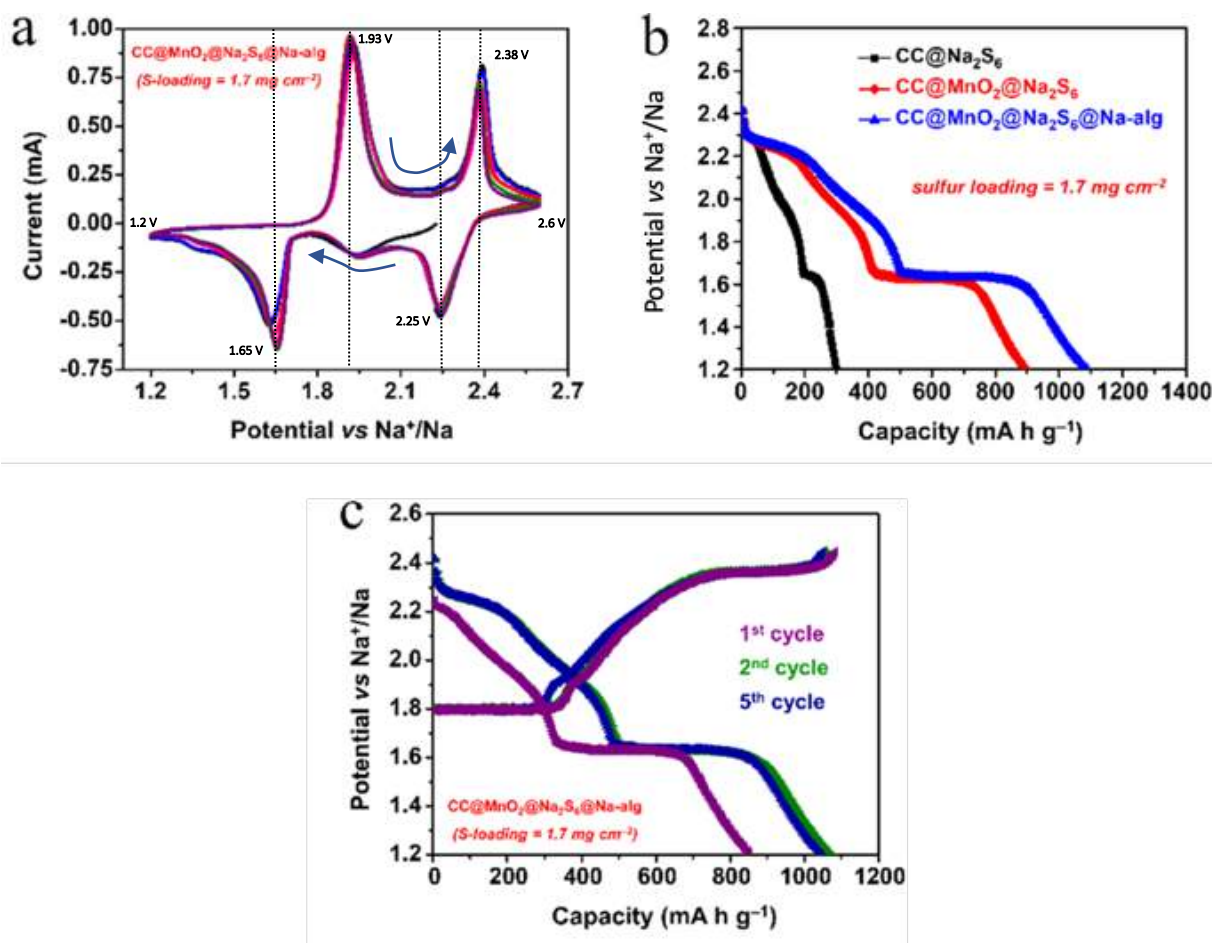


Figure 4.4: (a) Cyclic voltammograms of the CC@MnO₂@Na₂S₆@Na-alg cathode (sulfur loading = 1.7 mg cm⁻²) at the scan rate of 0.1 mV s⁻¹; (b) second cycle discharge profiles of CC@Na₂S₆, CC@MnO₂@Na₂S₆ and CC@MnO₂@Na₂S₆@Na-alg cathodes with sulfur loading of 1.7 mg cm⁻² at 0.2C; (c) charge-discharge profiles of the CC@MnO₂@Na₂S₆@Na-alg cathode (sulfur loading = 1.7 mg cm⁻²) at 0.2C for first, second and fifth cycles at 20°C ± 2°C.

Figure 4.5a shows the cycling performances of the CC@MnO₂@Na₂S₆ and CC@MnO₂@Na₂S₆@Na-alg cathodes with different sulfur loading at 0.2C rate. The CC@MnO₂@Na₂S₆ cathode with sulfur loading of 1.7 mg cm⁻² delivered an initial specific capacity of 892 mA h g⁻¹ and retained a specific capacity up to 628 mA h g⁻¹ after 300 cycles, with an average capacity decay rate of 0.1% per cycle. Maintaining identical areal loading of sulfur, the CC@MnO₂@Na₂S₆@Na-alg cathode exhibited an initial reversible specific capacity of 1087 mA h g⁻¹ and retained a specific capacity of 1005 mA h g⁻¹ after 300 cycles, with a remarkably low rate of capacity decay (0.02%) per cycle.

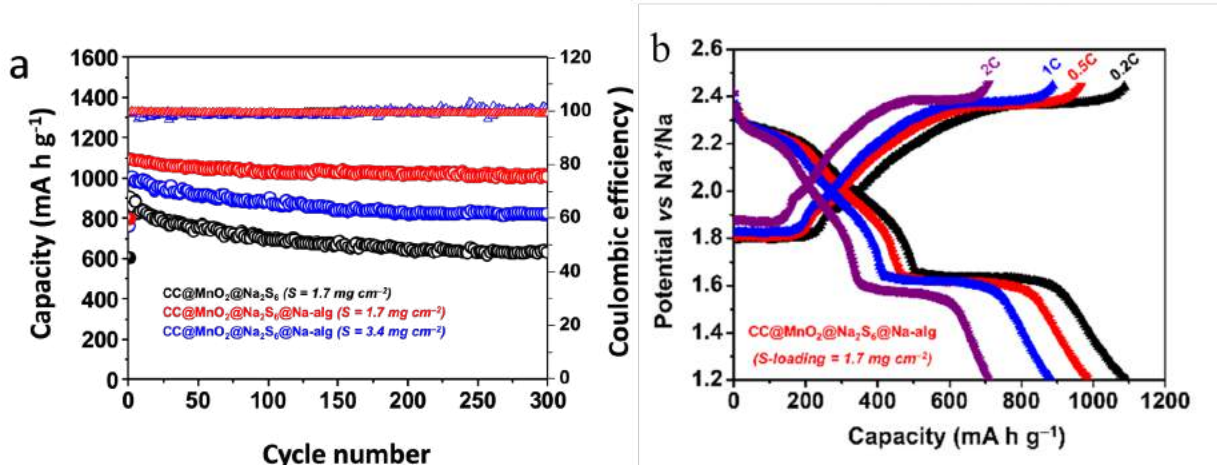


Figure 4.5: (a) cycling performance and coulombic efficiency versus cycle number of CC@MnO₂@Na₂S₆ cathode (sulfur loading = 1.7 mg cm⁻²), CC@MnO₂@Na₂S₆@Na-alg cathode (sulfur loading = 1.7 mg cm⁻² and 3.4 mg cm⁻²) at 0.2C; (b) charge-discharge profiles of CC@MnO₂@Na₂S₆@Na-alg cathode (sulfur loading = 1.7 mg cm⁻²) cathode at different C-rates at 20°C ± 2°C.

The substantial improvement in the cycling performance of RT Na-S batteries containing the CC@MnO₂@Na₂S₆@Na-alg cathode can be ascribed to the incorporation sodium-alginate as an additional component to the electrode architecture. Besides its excellent mechanical properties, the unique nanofiber morphology of sodium-alginate offers essential substructure to the cathode to sustain for longer time under constant charge-discharge condition. Moreover, the oxygenic functional groups (i.e., -OH, C-O-C and -COONa) in sodium-alginate could effectively interact with the sodium-polysulfides and eventually restrict their gradual dissolution into the electrolyte, thus significantly reducing the rate of capacity fading during cycling. In order to further explore the robustness of the CC@MnO₂@Na-alg scaffold, a cathode containing higher amount of catholyte (sulfur loading = 3.4 mg cm⁻²) was cycled at 0.2C rate. It is noteworthy to observe that the CC@MnO₂@Na₂S₆@Na-alg cathode containing twice the amount of sulfur (i.e., 3.4 mg cm⁻²) still exhibits higher specific capacity in comparison to the CC@MnO₂@Na₂S₆ cathode containing the sulfur loading of 1.7 mg cm⁻². The CC@MnO₂@Na₂S₆@Na-alg cathode, containing 3.4 mg cm⁻² areal loading of sulfur, delivered an initial reversible capacity of 1007 mA h g⁻¹ and retained a specific capacity up to 815 mA h g⁻¹ after 300 cycles, with an average capacity decay rate of 0.06% per cycle. Figure 4.5b represents charge-discharge profiles of the

CC@MnO₂@Na₂S₆@Na-alg cathode (sulfur loading = 1.7 mg cm⁻²) at different C-rates. With the sulfur mass loading of 1.7 mg cm⁻², the CC@MnO₂@Na₂S₆@Na-alg cathode delivered reversible specific capacities of 1082 mA h g⁻¹, 978 mA h g⁻¹, 867 mA h g⁻¹ and 712 mA h g⁻¹ at 0.2 C, 0.5 C, 1C, and 2C, respectively. Among three different electrodes, both the CC@MnO₂@Na₂S₆@Na-alg cathode containing the sulfur loading of 1.7 and 3.4 mg cm⁻² exhibited the excellent rate capability in terms of delivered specific capacities and better capacity retention at different C-rates (Figure 4.6a).

Long-term cycling was performed to further understand the robust substructure of the CC@MnO₂@Na₂S₆@Na-alg cathode. Figure 4.6b compares the prolonged cycling performance of cathodes with different loading factors for 1000 cycles at 1C rate. When the CC@MnO₂@Na₂S₆ cathode (sulfur loading = 1.7 mg cm⁻²) was cycled at 1C, 90% of initial reversible capacity of 642 mA h g⁻¹ was retained after 1000 cycles. However, maintaining similar sulfur loading of 1.7 mg cm⁻², the CC@MnO₂@Na₂S₆@Na-alg cathode exhibited much higher reversible capacity and relatively stable cycling performance at 1C (Figure 4.6b). The CC@MnO₂@Na₂S₆@Na-alg cathode with sulfur loading of 1.7 mg cm⁻² delivered an initial reversible capacity of 882 mA h g⁻¹ and retains 838 mA h g⁻¹ (i.e., 95% of initial reversible capacity) after 1000 cycles. The observed higher specific capacity and relatively stable cycling performance for the CC@MnO₂@Na₂S₆@Na-alg cathode (sulfur loading of 1.7 mg cm⁻²) further accredit to the robustness of the electrode, thanks to the excellent mechanical properties of sodium-alginate nanofibers. However, the CC@MnO₂@Na₂S₆@Na-alg cathode, with an average sulfur loading of 3.4 mg cm⁻², delivers an initial reversible capacity of 752 mA h g⁻¹ and retains 94% of the initial reversible capacity after 1000 cycles.

Herein, MnO₂ has been used as a polysulfide trapping element which also promotes the conversion kinetics of PS to elemental sulfur. MnO₂ is the primary component in the cathode structure which takes part in the charge transfer reaction towards the conversion and confinement owing to its polar nature. Na-alginate has been used as a binder as well as an additional component coated over MnO₂ to accommodate more amount of the active material and promotes the diffusion of PS as well as Na⁺ during the cell operation. The fibrous structure of alginate consists of abundant number of functional groups which are also believed to be efficient anchoring sites for PS. But unlike MnO₂, Na-alginate does not participate in charge transfer reaction with the PS, it only

anchors the PS and makes the PS more accessible to MnO_2 . This argument has been probed with the theoretical calculation (DFT).

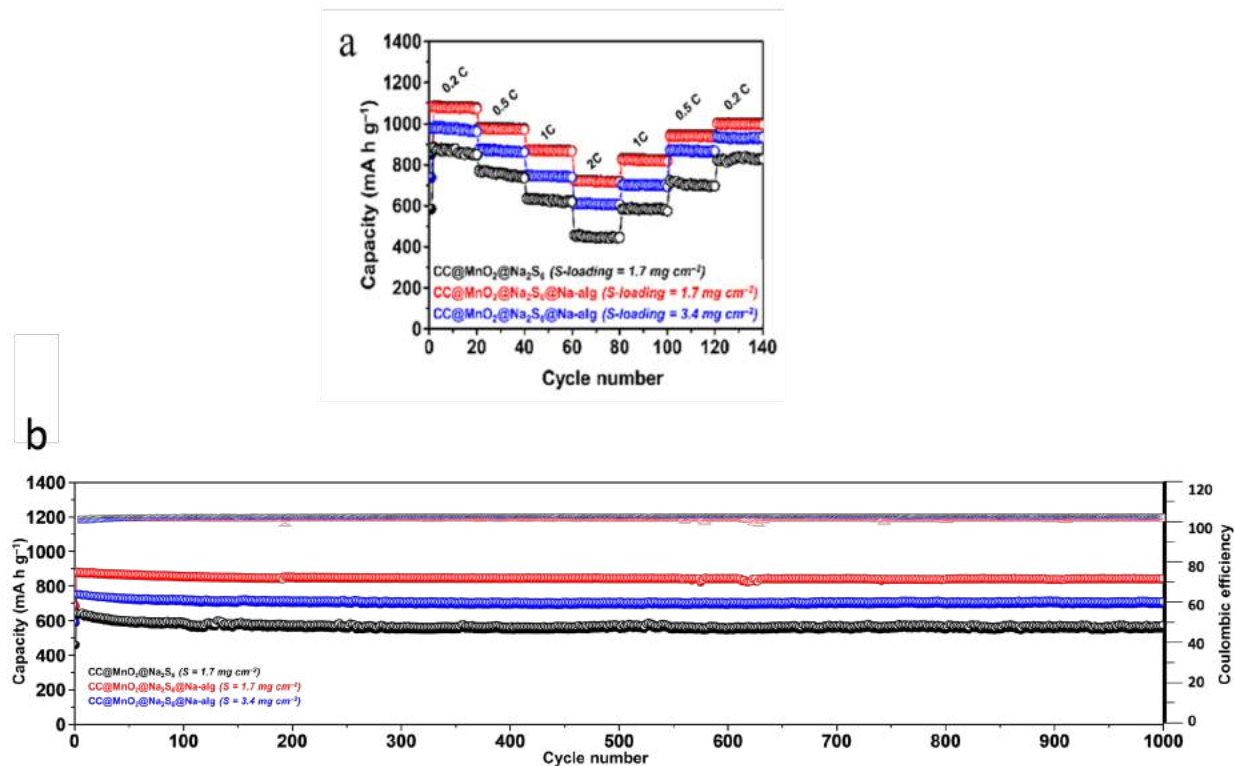


Figure 4.6: (a) rate performance and (b) long-term cycling performance and coulombic efficiency versus cycle number of $\text{CC@MnO}_2\text{@Na}_2\text{S}_6$ cathode (sulfur loading = 1.7 mg cm^{-2}), $\text{CC@MnO}_2\text{@Na}_2\text{S}_6\text{@Na-alg}$ cathodes (sulfur loading = 1.7 mg cm^{-2} and 3.4 mg cm^{-2}) at 1C at $20^\circ\text{C} \pm 2^\circ\text{C}$.

4.2.3. DFT simulation

To offer significant insight into the superior polysulfide adsorption efficiency of sodium-alginate, theoretical calculations based on density functional theory (DFT) were carried out. In the present study, sodium-alginate has been used as an efficient binder as well as polysulfide immobilizer. Sodium-alginate is a bio-polymer, enriched in carboxylate and hydroxyl groups²⁷. Due to the presence of plenty of polar functional groups, sodium-alginate looks promising promising to anchor the higher-order sodium-polysulfides. Sodium-alginate nanofibers over the MnO_2 nanoarrays help the soluble intermediates to access MnO_2 more easily and thus increase the reaction kinetics as well as effective utilization of active material in the $\text{CC@MnO}_2\text{@Na}_2\text{S}_6\text{@Na-}$

alg cathode. The O-atoms in hydroxyl and carboxylate moieties strongly anchor the sodium-polysulfides through Lewis acid-based interaction. The lone pair of electrons on O interact with the positively charged Na in sodium-polysulfides by means of electrostatic attraction²⁷. The optimized structures of different sodium-polysulfides are shown in Figure 4.7. Figure 4.9a shows Mulliken charge distribution on carboxylate ($-\text{COONa}$, site 1) and hydroxyl group ($-\text{OH}$, site 2) in sodium-alginate, before Na_2S adsorption. Upon interacting with carboxylate moiety in sodium-alginate, Na_2S withdraws 0.412 and 0.053 amount of charge from Na atom and O atom (site 1, highlighted with blue dotted circle), respectively (Figure 4a). The amount of charge transfer for the O atom at Site 2 (highlighted with dotted circle) is around 0.053, which is similar to the O atom at Site 1 (Figure 4a). Hence, it can be inferred that both Na and O atoms in sodium-alginate serve as anchoring sites and play a significant role in polysulfides adsorption. Due to high electronegativity of oxygen, the carboxylate (site 1) and hydroxyl (site 2) groups possess highest electron density, as indicated by the electron density mapping (inset, Figure 4.9b). Hence, both the oxygen-containing sites have been investigated as anchoring sites for the adsorption of sodium-polysulfides. Figure 4.9b depicts the calculated binding energies of various sodium-polysulfide species at two different anchoring sites (site 1 and site 2). The adsorption energies of Na_2S_6 , Na_2S_4 and Na_2S over both site 1 and site 2 are estimated to be within the range of -1.85 eV to -2.85 eV (negative binding energy indicates preferable adsorption), which are much higher than the binding energies between NaPS and nonpolar carbon²⁷. The abundant number of anionic as well as cationic anchoring sites results in such intense polysulfides adsorption. However, for both the anchoring sites, Na_2S_4 showed strongest binding affinity; while Na_2S_6 exhibited the weakest binding affinity.

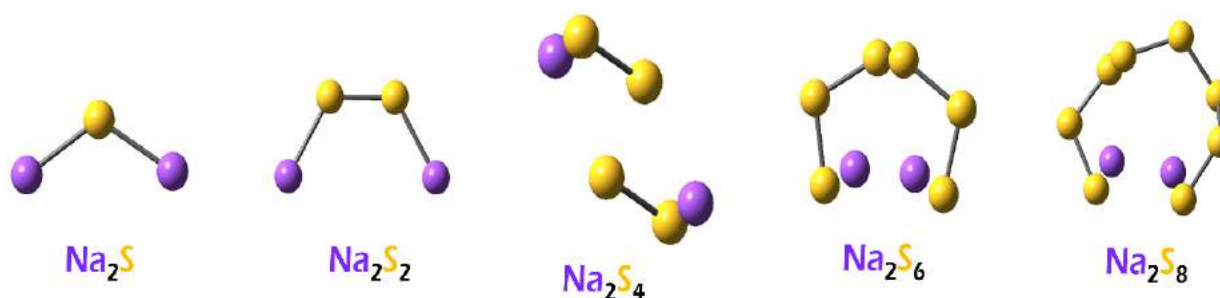


Figure 4.7: Optimized structures of different sodium-polysulfides.

The optimized geometries of different polysulfide-adsorbed systems have been represented in Figure 4.8. The DOS plots of sodium-alginate before and after Na_2S_4 (for both the anchoring sites) depict no significant change near the Fermi energy (indicated with dotted line, E_F) (Figure 4.9c), indicating that sodium-alginate binds the polysulfides without participating in the charge transfer process.

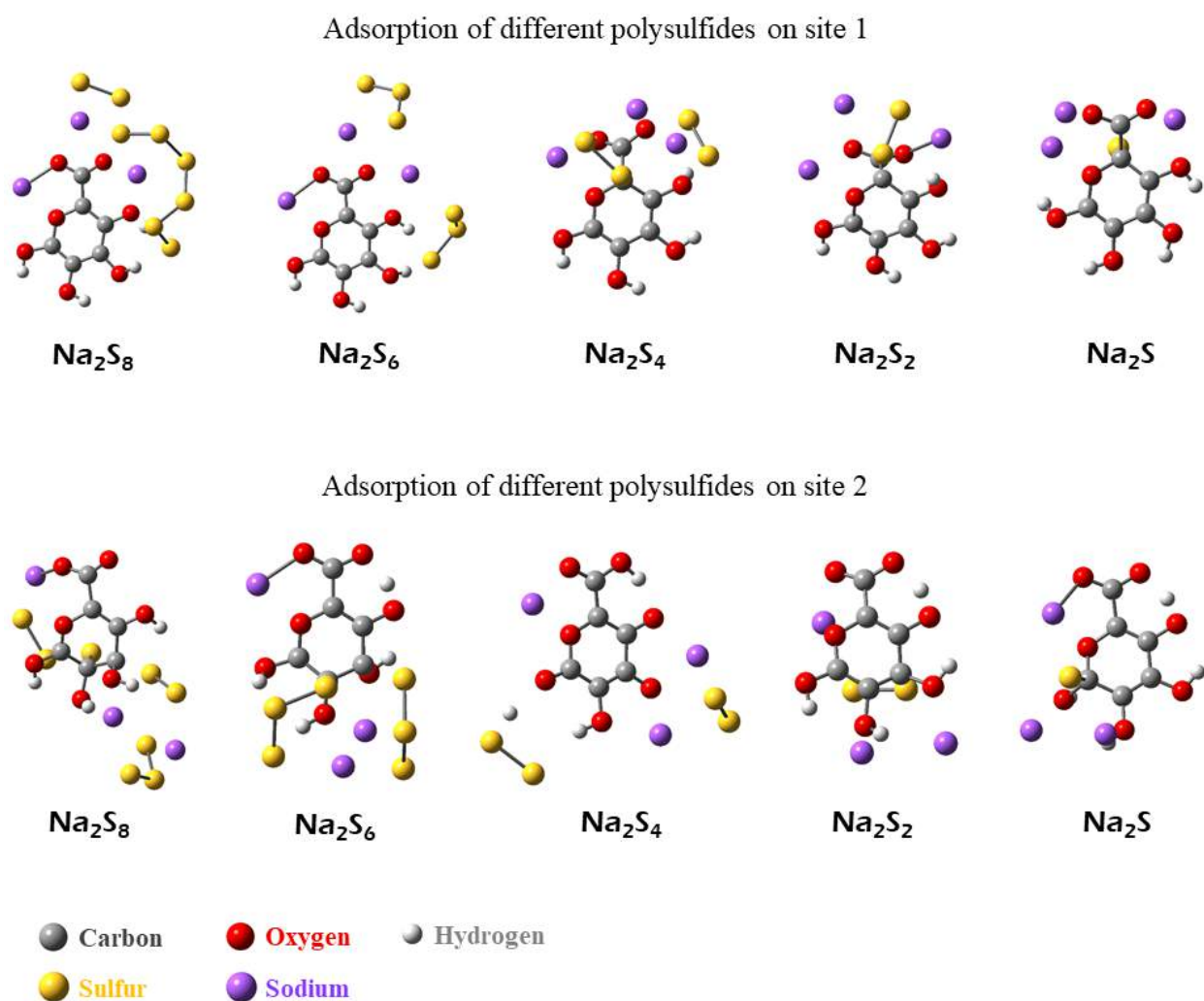


Figure 4.8: Optimized geometries of different polysulfide-adsorbed systems.

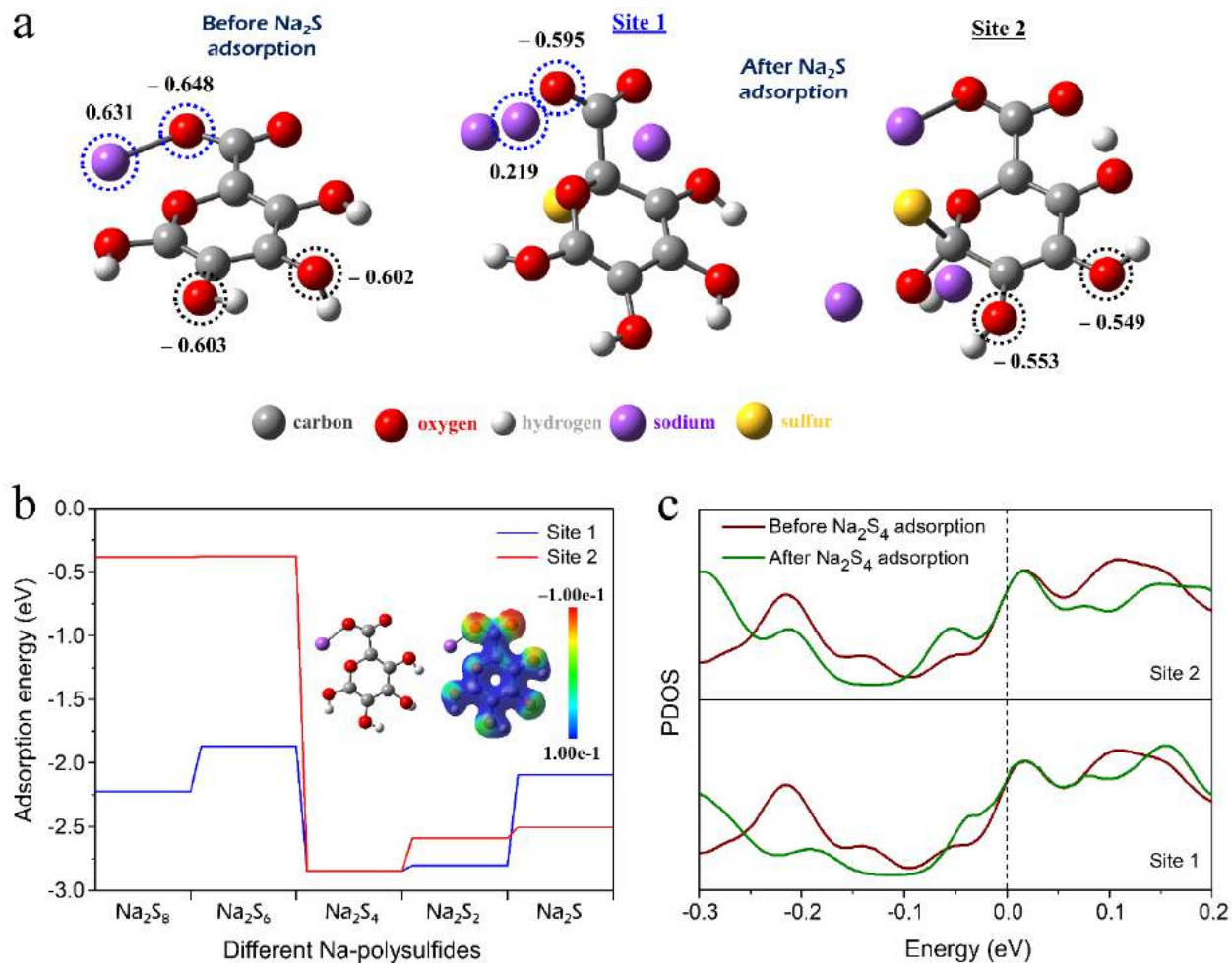


Figure 4.9: (a) Mulliken charge distribution before and after adsorption of Na_2S for site 1 and site 2; (b) binding energies of different Na-polysulfides on sodium-alginate, inset shows optimized geometry and electron density mapping of a sodium-alginate unit; (c) partial density of states of sodium-alginate before and after Na_2S_4 adsorption.

4.2.4. Post-cycling analysis of $\text{CC@MnO}_2@\text{Na}_2\text{S}_6@\text{Na-alg}$ cathode

To obtain further insight into the polysulfide adsorption and retention efficiency of $\text{CC@MnO}_2@\text{Na-alg}$ substrate, ex-situ SEM characterization was carried out on a cycled $\text{CC@MnO}_2@\text{Na}_2\text{S}_6@\text{Na-alg}$ cathode.

Figure 4.10a represents the SEM image of cathode after 1000 cycles at a fully discharged state. It is noteworthy to observe that the $\text{CC@MnO}_2@\text{Na-alg}$ substrate maintained its original mechanical

integrity even after prolonged charge-discharge cycles. The elemental mapping exhibits a uniform coexistence of the constituent elements (i.e., C, O, Mn, Na, and S) on the $\text{CC@MnO}_2\text{@Na}_2\text{S}_6\text{@Na-alg}$ cathode.

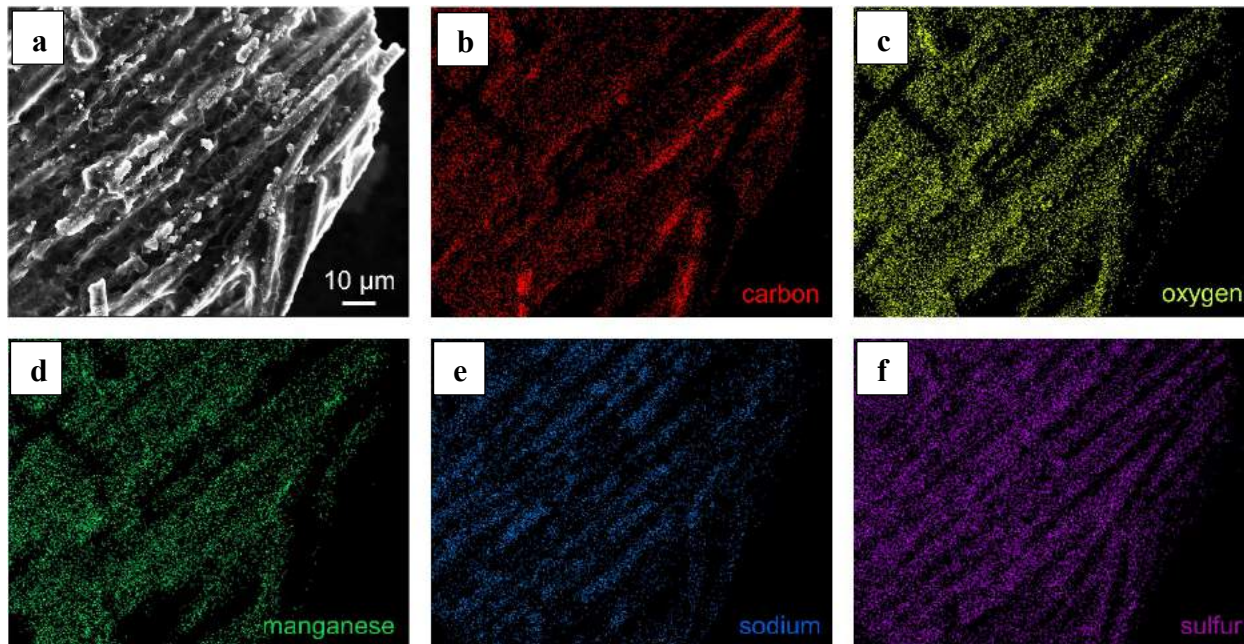


Figure 4.10: (a) Scanning electron microscopy image of $\text{CC@MnO}_2\text{@Na}_2\text{S}_6\text{@Na-alg}$ cathode after 1000 cycles, at fully discharged state; (b–f) mapping of different elements taken on the cycled electrode.

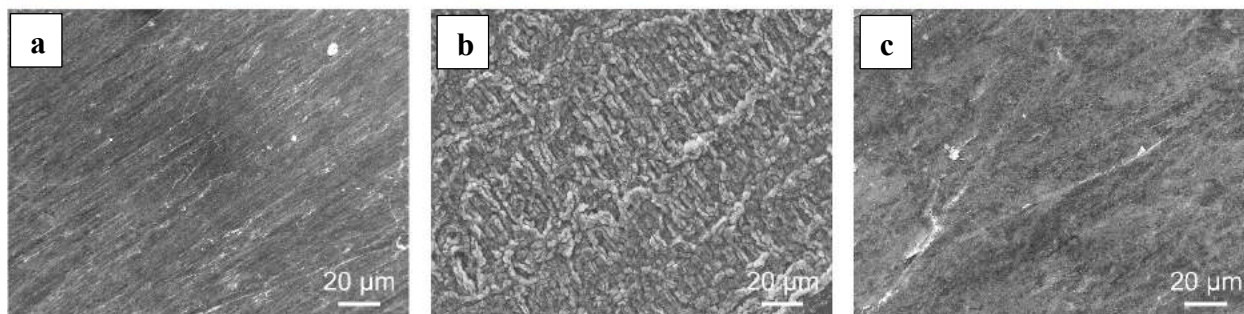


Figure 4.11: (a) SEM image of fresh sodium metal surface before cycling; (b, c) SEM images of cycled sodium anode surface placed towards $\text{CC@Na}_2\text{S}_6$ cathode after 50 cycles and $\text{CC@MnO}_2\text{@Na}_2\text{S}_6\text{@Na-alg}$ cathode after 300 cycles.

Sulfur and sodium mapping (Figure 4.10e & 4.10f) confirm that a mixed phase of different sodium-polysulfides was uniformly distributed throughout the CC@MnO₂@Na-alg substrate, suggesting excellent affinity of both MnO₂ and sodium-alginate towards the intermediate products which leads to an extremely stable cycling performance. To further enlighten the effective entrapment of sodium-polysulfides and reduced shuttle effect in RT Na-S batteries containing the CC@MnO₂@Na₂S₆@Na-alg cathode, surface morphology of the cycled sodium metal anode placed towards this cathode was investigated. For better understanding, the surface morphology of a cycled sodium metal anode placed against the control CC@Na₂S₆ cathode was also examined. The ex-situ SEM image of the cycled sodium anode surface placed against the CC@MnO₂@Na₂S₆@Na-alg cathode exhibited a smooth surface similar to the sodium metal before cycling (Figure 4.11a & 4.11c). This observation strongly suggests that due to an effective entrapment of the sodium-polysulfide species in the CC@MnO₂@Na₂S₆@Na-alg cathode, the undesired side reaction between sodium metal and soluble polysulfides associated with shuttle phenomenon was completely mitigated, leading smooth surface of sodium anode. On the contrary, the sodium metal anode placed against the control CC@Na₂S₆ cathode exhibited severely rough surface after cycling (Figure 4.11b), as also observed from our previous study. This suggests that bare carbon cloth was not enough to effectively immobilize the soluble intermediates, therefore, causing severe shuttle effect in RT Na-S batteries.

4.3 Conclusions

We have developed a mechanically robust, integrated cathode scaffold consisting of sodium-alginate wrapped MnO₂ nanoarrays decorated carbon cloth which synergistically increase the redox kinetics and mitigate fatal polysulfide shuttling and the electrode pulverization. Here, carbon cloth provides continuous electronic pathway, whereas, MnO₂ nanoarrays and sodium-alginate nanofibers offer enormous adsorption sites to bind the sodium-polysulfides chemically and physically and further accelerate the redox conversion. The CC@MnO₂@Na-alg substrate infiltrated with Na₂S₆ catholyte has delivered an initial reversible specific capacity of 882 mA h g⁻¹, retaining 838 mA h g⁻¹ after 1000 cycles. Addition of alginate results in an enhancement in specific capacity and capacity retention of CC@MnO₂ architecture by 37 % and 10 % respectively. This superior electrochemical performance has been attributed to the fibrous nature of alginate which promotes the faster transport of ions and complete utilization of active material.

Furthermore, a complete computational analysis estimates the possible binding sites and binding strength of alginate molecule towards PS confinement. Considering the intriguing electrochemical performance of the cathode structure, it is believed that the current proof of concept might open up a new direction in designing diverse sulfur-based cathodes for the high energy-density and stable RT Na-S batteries.

References

1. B. Dunn, H. Kamath, J. Tarascon, *Science* 2011, 334, 928–935.
2. X. Lu, G. Xia, J. P. Lemmon, Z. Yang, *J. Power Sources* 2010, 195, 2431–2442.
3. C. Park, J. Ahn, H. Ryu, K. Kim, H. Ahn, *Electrochem. Solid-State Lett.* 2006, 9, A123–A125.
4. A. Manthiram, X. Yu, *Small* 2015, 11, 2108–2114.
5. Y. Wang, B. Zhang, W. Lai, Y. Xu, S. Chou, H. Liu, S.-X. Dou, *Adv. Energy Mater.* 2017, 7, 1602829.
6. S. Xin, Y. Yin, Y. Guo, L. Wan, *Adv. Mater.* 2014, 26, 1261–1265.
7. X. Yu, A. Manthiram, *J. Phys. Chem. C* 2014, 118, 22952–22959.
8. X. Yu, A. Manthiram, *Adv. Energy Mater.* 2015, 5, 1500350.
9. Y. Wang, J. Yang, W. Lai, S. Chou, Q. Gu, H. K. Liu, D. Zhao, S.-X. Dou, *J. Am. Chem. Soc.* 2016, 138, 16576–16579.
10. S. Wei, S. Xu, A. Agrawal, S. Choudhury, Y. Lu, Z. Tu, L. Ma, L. A. Archer, *Nat. Commun.* 2016, 7, 11722.
11. Y. Chen, W. Liang, S. Li, F. Zou, S. M. Bhaway, Z. Qiang, M. Gao, B. D. Vogt, Y. Zhu, *J. Mater. Chem. A* 2016, 4, 12471–12478.
12. Z. Qiang, Y. Chen, Y. Xia, W. Liang, Y. Zhu, B. D. Vogt, *Nano Energy* 2017, 32, 59–66.
13. R. Carter, L. Oakes, A. Douglas, N. Muralidharan, A. P. Cohn, C. L. Pint, *Nano Lett.* 2017, 17, 1863–1869.
14. Q. Lu, X. Wang, J. Cao, C. Chen, K. Chen, Z. Zhao, Z. Niu, J. Chen, *Energy Storage Mater.* 2017, 8, 77–84.
15. B.-W. Zhang, T. Sheng, Y.-D. Liu, Y.-X. Wang, L. Zhang, W.-H. Lai, L. Wang, J. Yang, Q.-F. Gu, S.-L. Chou, H.-K. Liu, S.-X. Dou, *Nat. Commun.* 2018, 9, 4082.
16. Z. Yan, J. Xiao, W. Lai, L. Wang, F. Gebert, Y. Wang, Q. Gu, H. Liu, S.-L. Chou, H. Liu, S.-X. Dou, *Nat. Commun.* 2019, 10, 4793.
17. J. Wang, J. Yang, C. Wan, K. Du, J. Xie, N. Xu, *Adv. Funct. Mater.* 2003, 13, 487–492.
18. J. Fanous, M. Wegner, J. Grimming, A. Andresen, M. R. Buchmeiser, *Chem. Mater.* 2011, 23, 5024–5028.
19. T. H. Hwang, D. S. Jung, J.-S. Kim, B. G. Kim, J. W. Choi, *Nano Lett.* 2013, 13, 4532–4538.

20. I. Kim, C. H. Kim, S. H. Choi, J. P. Ahn, J. H. Ahn, K. Kim, E. Cairns, H. J. Ahn, *J. Power Sources* 2016, 307, 31–37.
21. A. Ghosh, S. Shukla, M. Monisha, A. Kumar, B. Lochab, S. Mitra, *ACS Energy Lett.* 2017, 2, 2478–2485.
22. L. Fan, R. Ma, Y. Yang, S. Chen, B. Lu, *Nano Energy* 2016, 28, 304–310.
23. D. Ma, Y. Li, J. Yang, H. Mi, S. Luo, L. Deng, C. Yan, M. Rauf, P. Zhang, X. Sun, X. Ren, J. Li, H. Zhang, *Adv. Funct. Mater.* 2018, 28, 1705537.
24. A. Kumar, A. Ghosh, A. Roy, M. R. Panda, M. Forsyth, D. R. MacFarlane, S. Mitra, *Energy Storage Mater.* 2019, 20, 196–202.
25. W. Bao, C. E. Shuck, W. Zhang, X. Guo, Y. Gogotsi, G. Wang, G. ACS Nano 2019, 13, 11500–11509.
26. A. Ghosh, A. Kumar, A. Roy, M. R. Panda, M. Kar, D. R. MacFarlane, S. Mitra, *ACS Appl. Mater. Interfaces* 2019, 11, 14101–14109.
27. Q. Guo, Z. Zheng, *Adv. Funct. Mater.* 2019, 30, 1907931.
28. A. Ghosh, R. Manjunatha, R. Kumar, S. Mitra, *ACS Appl. Mater. Interfaces* 2016, 8, 33775–33785.
29. G. A. Ayoko, *RSC Adv.* 2018, 8, 2271–2279.

Chapter 5

Free-radical catalysis enhances the redox kinetics of room-temperature
sodium-sulfur batteries

Chapter 5

5.1. Introduction

The different remedies for polysulfide dissolution in terms of physical encapsulation and/or strong chemical confinement have proven to be effective to some extent, unfortunately these cathode architectures still suffer from poor redox kinetics of the sulfur/polysulfides interconversion, leading to a lower than theoretical cell potential (~ 1.5 V), resulting in low practical energy density¹⁻²⁶. Therefore, a sulfur host which offers strong binding sites for polysulfides, along with continuous electron transport pathway, and that also promotes the reaction kinetics between sulfur and the polysulfides, so that a higher cell energy density could be achieved, would represent a significant step towards practical RT Na-S batteries.

In this work, we introduce a highly activated, high internal surface area carbon cloth as a conductive sulfiphilic host to support the reversible redox conversion between sulfur and the discharge products. A liquid-phase sodium polysulfide (Na_2S_6) catholyte is used as the active material in our cell design. The use of carbon cloth as current collector significantly enhances the electronic conductivity pathway throughout the cathode scaffold and hence improves the active sulfur utilization. An extra reduction peak at 1.97 V with good reversibility is observed, being reported and studied here for the first time. The cyclic voltammetry study, coupled with electron spin resonance (ESR) experiment, reveals that the activated carbon cloth substrate catalyses the redox conversion of intermediate polysulfide radical monoanions to lower-order polysulfides ($\text{S}_3^{\bullet-} \rightarrow \text{S}_2^{2-}$) through a free-radical mechanism. At a current rate of 0.2 C ($C = 1672 \text{ mA h g}_{(\text{S})}^{-1}$), a RT Na-S battery containing the $\text{Na}_2\text{S}_6@\text{ACC}$ cathode with high sulfur loading (3.4 mg cm^{-2}) operates at a high nominal discharge potential of 1.85 V, delivering an initial reversible specific capacity of $982 \text{ mA h g}_{(\text{S})}^{-1}$. At a higher current rate of 0.5 C, the $\text{Na}_2\text{S}_6@\text{ACC}$ cathode delivers a high specific capacity of $866 \text{ mA h g}_{(\text{S})}^{-1}$ and retains $678 \text{ mA h g}_{(\text{S})}^{-1}$ after 700 cycles, yielding a capacity decay rate of only 0.03% per cycle.

5.2. Results and discussion

5.2.1 Synthesis and characterization

To fabricate the catholyte infiltrated activated carbon cloth as a freestanding cathode, a commercially available polyacrylonitrile based carbon cloth was first chemically activated by an alkaline treatment at elevated temperatures (800°C).^{27,28} The average areal mass density of the activated carbon cloth (ACC) is estimated to be 99.7 g m⁻², compared to that of the pristine carbon cloth (~125 g m⁻²). The lower areal mass density of ACC indicates severe corrosion of carbon fibers under vigorous chemical treatment. The Brunauer–Emmett–Teller (BET) surface area of activated carbon cloth (ACC) is calculated to be approximately 178 m² g⁻¹, which is much larger than the pristine carbon cloth (PCC) (~45 m² g⁻¹). After successful activation of the carbon cloth, sodium polysulfide (Na₂S₆) catholyte was added dropwise and allowed to be absorbed into it. This catholyte-adsorbed activated carbon cloth (i.e., Na₂S₆@ACC) was then used as the cathode in our Na-S batteries. The stepwise process of fabrication of this Na₂S₆@ACC cathode is schematically represented in Figure 5.1.

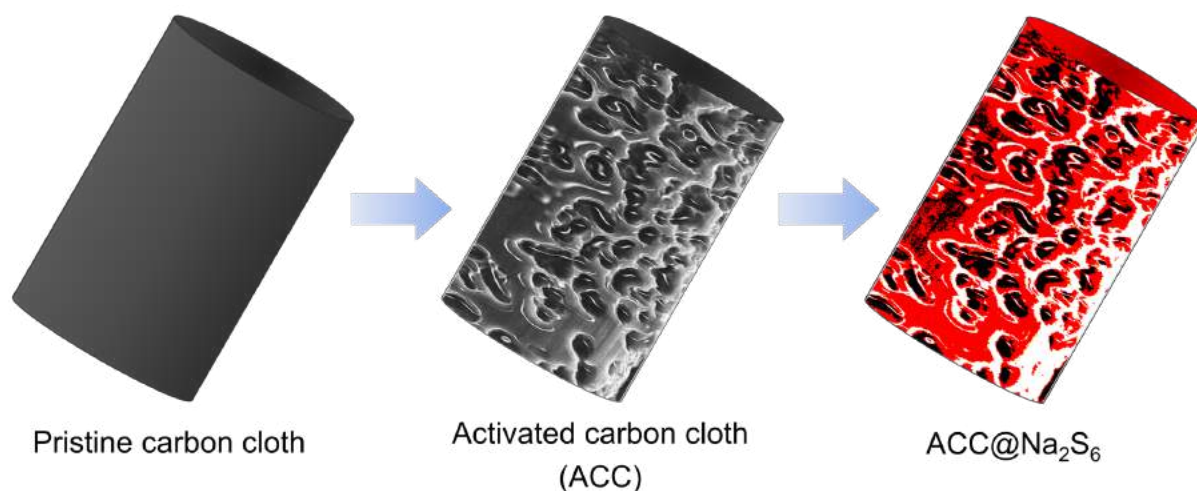


Figure 5.1: Schematics of pristine carbon cloth, activated carbon cloth and ACC@Na₂S₆ cathode

Microstructures of the pristine carbon cloth, the activated carbon cloth (ACC) and the polysulfide adsorbed activated carbon cloth (Na₂S₆@ACC) were investigated through electron microscopy techniques in different modes. The SEM and TEM images of the pristine carbon cloth fibers exhibit smooth surfaces, with an average diameter of 7 μm (Figure 5.2a and d).

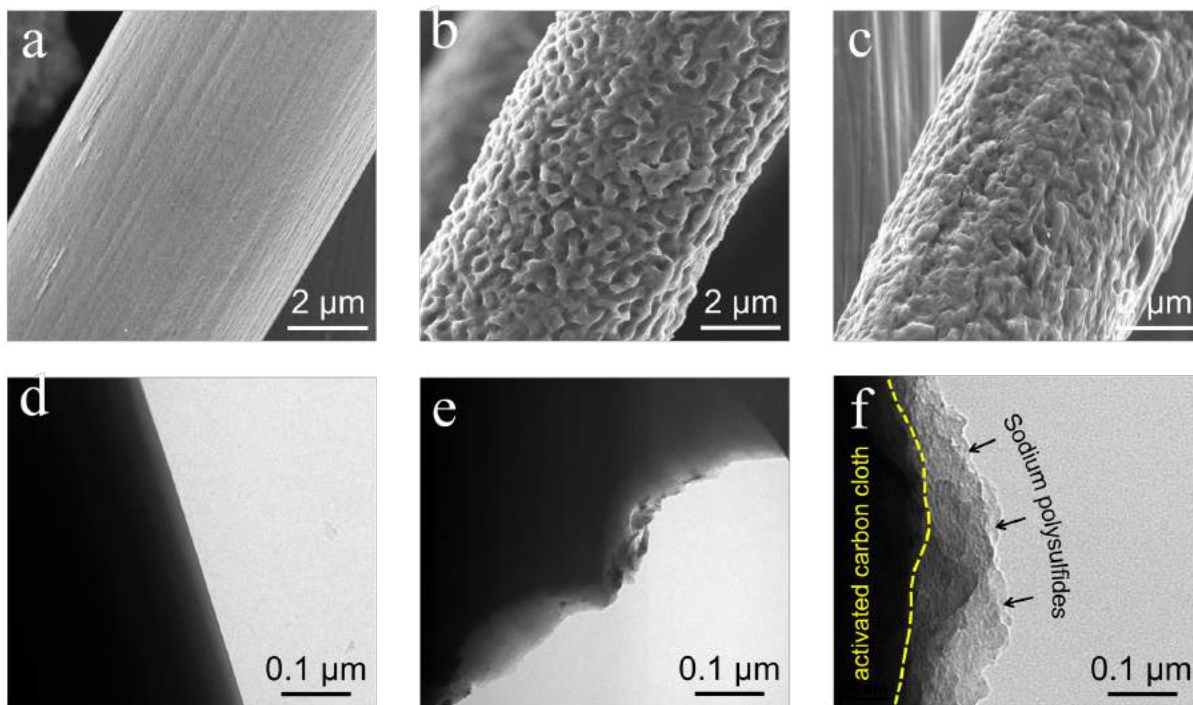


Figure 5.2: (a–c) SEM images and (d–f) TEM images of pristine carbon cloth (a, d), activated carbon cloth (d, e) and ACC@Na₂S₆ cathode (c, f).

In sharp contrast, the SEM image of ACC shows the generation of many pits on the carbon fibers after the chemical treatment (Figure 5.2b). This observation indicates the strong corrosive nature of NaOH towards this polyacrylonitrile-based carbon cloth at high temperatures (800 °C). The high-resolution SEM and TEM image of the activated carbon reveals the formation of pits with diameter in the range of 100–150 nm (Figure 5.3 and Figure 5.2e). Due to the homogeneity and facile dispersibility of the catholyte, it is expected that the submicron-sized pits generated on the surface of the carbon cloth fibers can accommodate large amounts of active material; the SEM image of Na₂S₆@ACC cathode shows that the pits were well covered with Na₂S₆ active material (Figure 5.2c). TEM image of the Na₂S₆@ACC substrate further indicates the accumulation of the Na₂S₆ on the surface of ACC (Figure 5.2f).

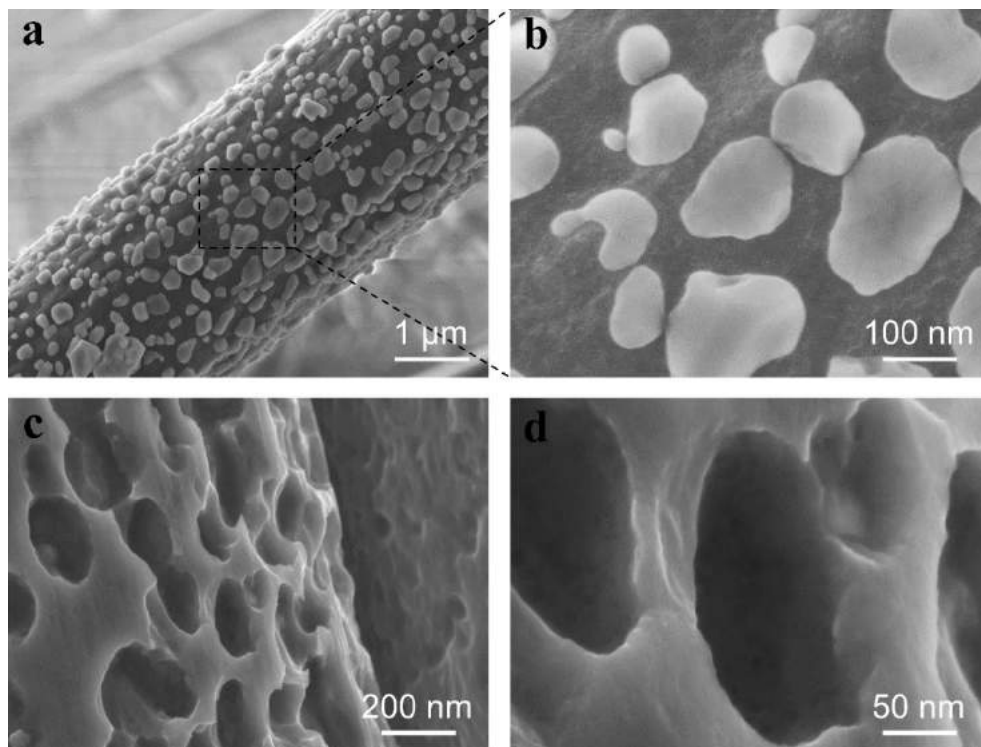


Figure 5.3: SEM images of activated carbon cloth before washing (a, b) and after washing with de-ionized water (c, d).

5.2.2 Electrochemical performance of $\text{Na}_2\text{S}_6@\text{ACC}$ cathode

The $\text{Na}_2\text{S}_6@\text{ACC}$ substrate was used as the freestanding cathode along with a sodium metal anode to construct Na-S coin cells. To demonstrate the superiority of the activated carbon cloth as a current collector and sulfur host, electrochemical responses of a pristine carbon cloth infiltrated with Na_2S_6 catholyte (i.e., $\text{Na}_2\text{S}_6@\text{PCC}$) were also recorded and compared. In both the cases, the RT Na-S cells were discharged (i.e., the Na_2S_6 was first reduced) in the first cycle. Figure 5.4a illustrates the cyclic voltammograms of the $\text{Na}_2\text{S}_6@\text{PCC}$ cathode for the initial three cycles at a scan rate of 0.1 mV s^{-1} . During initial reduction, as expected the $\text{Na}_2\text{S}_6@\text{PCC}$ cathode exhibits one obvious reduction peak at 1.62 V, corresponding to conversion of Na_2S_6 to lower-order sodium polysulfides (Na_2S_n , $1 \leq n \leq 2$).²⁹ On the reverse scan, two distinguishable anodic peaks are observed at 1.92 V and 2.38 V, corresponding to a two-step oxidation of lower-order polysulfides to elemental sulfur (S_8).²⁹ From the second cycle onwards, the $\text{Na}_2\text{S}_6@\text{PCC}$ cathode displays two cathodic peaks at 2.27 V and 1.62 V, corresponding to the two-step reduction of elemental sulfur to lower-order polysulfides. From the cyclic voltammograms of the $\text{Na}_2\text{S}_6@\text{PCC}$ cathode it can be noticed

that after the first cycle, there is a severe decline in the current density of the reduction peak located at 1.62 V, indicating the poor kinetics associated with the formation of insoluble end-discharged products.

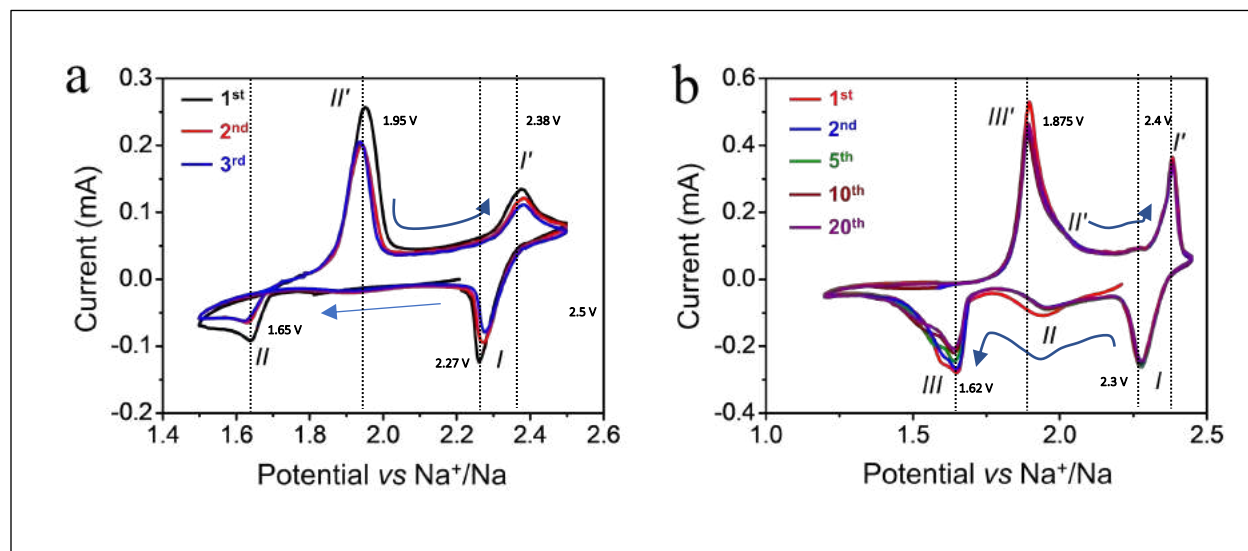


Figure 5.4: (a) Cyclic voltammograms of the Na₂S₆@CC cathode at a scan rate of 0.1 mV s⁻¹; (b) cyclic voltammograms of the Na₂S₆@ACC cathode at a scan rate of 0.1 mV s⁻¹ at 20°C ± 2°C.

Figure 5.4b shows the cyclic voltammograms of the Na₂S₆@ACC cathode at the scan rate of 0.1 mV s⁻¹ for the first, second, fifth, tenth and twentieth cycles. In contrast to Na₂S₆@PCC cathode, the Na₂S₆@ACC cathode exhibits three reduction peaks and three oxidation peaks, maintaining their reversibility in each cycle. Appearance of an additional pair of redox peaks (peaks II and II') at 1.97 V (during the cathodic scan) and 2.05 V (during the anodic scan) suggests involvement of a new redox process in the Na₂S₆@ACC cathode.

Figure 5.5a displays the representative first, fifth, and tenth cycle charge-discharge profiles of the Na₂S₆@ACC cathode at a 0.2 C current rate (C = theoretical capacity of sulfur = 1672 mA h g_(s)⁻¹). Due to existing reduced state of starting material (Na₂S₆), there is a large mismatch between the initial discharge capacity and the capacity obtained during the subsequent charge process. After the first cycle, the cell exhibits three discharge plateaus, beginning at 2.27 V, 1.97 V, and 1.65 V, respectively.

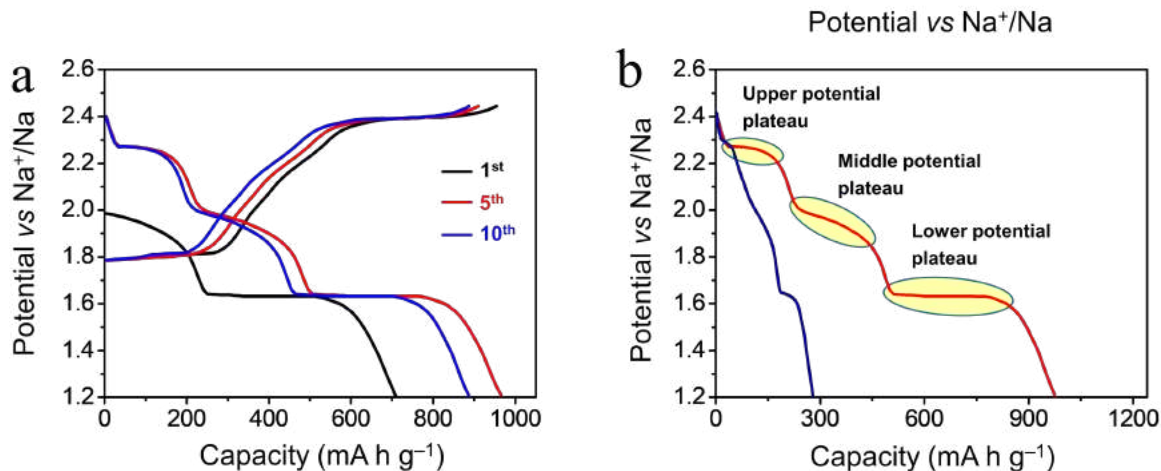


Figure 5.5: (a) Charge discharge profile of the Na₂S₆@ACC cathode 0.2 C; (b) Second cycle discharge profiles of Na₂S₆@CC and Na₂S₆@ACC at 0.2 C at 20°C ± 2°C.

The potential regions of the discharge plateaus exactly correspond to potential ranges of the three reduction peaks observed during the cyclic voltammetry scans. Figure 5.5b highlights the difference between the shape of the discharge curves of the Na₂S₆@PCC and Na₂S₆@ACC based cells, the additional plateau at 1.97 and the extended plateau at 1.65V considerably adding to the overall discharge capacity.

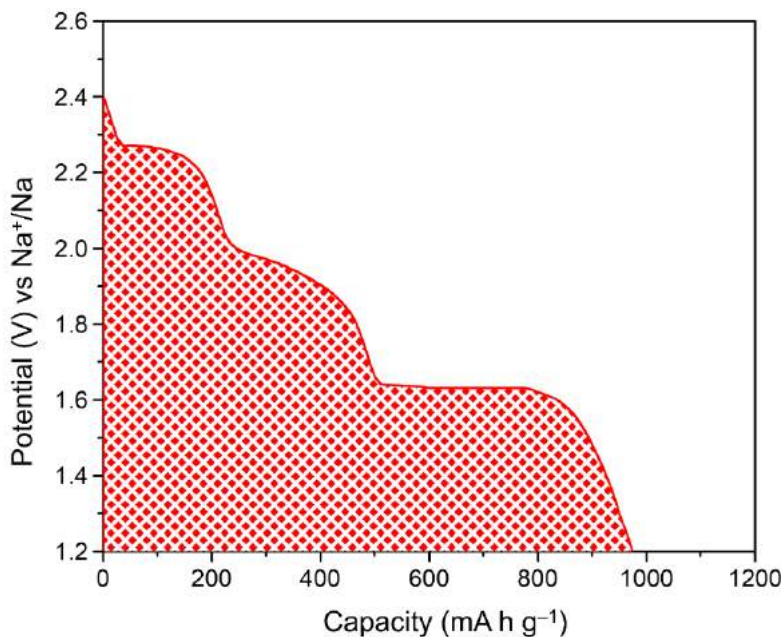


Figure 5.6: Second cycle discharge profile of Na₂S₆@ACC cathode at 0.2 C current rate.

Calculating the “nominal cell potential” via the integral approach (Figure 5.6), as recommended by Goodenough and coworkers,³⁴ indicates a nominal cell potential of 1.85V in this case (this process provides a capacity-weighted average potential across the multistep discharge profile).

Figure 5.7a demonstrates the cycling performance of Na₂S₆@PCC and Na₂S₆@ACC cathodes at 0.2 C. The Na₂S₆@PCC cathode exhibits poor cycling performance in terms of low specific capacity and high rate of capacity decay. The Na₂S₆@ACC cathode delivers an initial reversible capacity of 398 mA h g_(s)⁻¹ in the second cycle and maintains a capacity of 237 mA h g_(s)⁻¹ (i.e., 59.5% retention of initial reversible capacity) after 50 cycles.

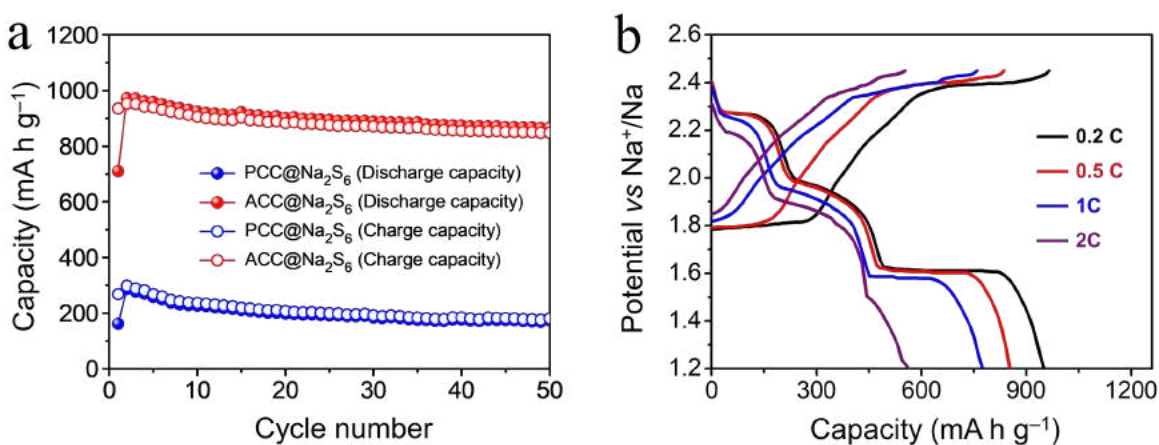


Figure 5.7: (a) cycling performance of Na₂S₆@CC and Na₂S₆@ACC cathodes at 0.2 C; (b) charge-discharge profiles of Na₂S₆@ACC cathode at different current rates at 20°C ± 2°C.

The Na₂S₆@ACC cathode showed much improved capacity and stable cycling performance, delivering an initial reversible specific capacity of 982 mA h g_(s)⁻¹ (areal capacity = 3.34 mA h cm⁻²) and retaining 867 mA h g_(s)⁻¹ (areal capacity = 2.95 mA h cm⁻²) after 50 cycles. The charge-discharge profiles of the Na₂S₆@ACC cathode at 0.2 C, 0.5 C, 1C, and 2C are shown in Figure 5.7b. The corresponding specific capacities obtained at different current rates are plotted against cycle number in Figure 5.8a.

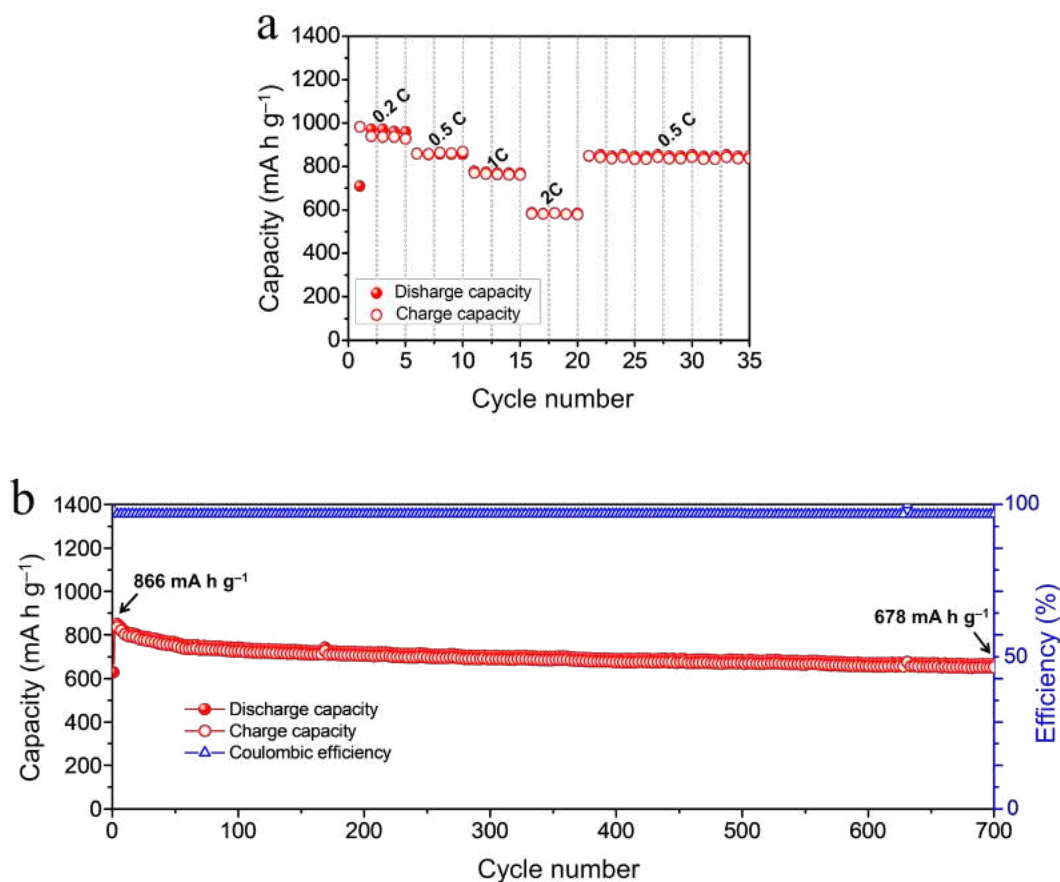


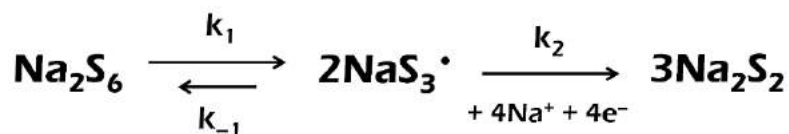
Figure 5.8: (a) rate capability of Na₂S₆@ACC cathode at different current rates; and (b) long-term cycling performance of Na₂S₆@ACC cathode at 0.5 C at 20°C ± 2°C.

The Na₂S₆@ACC cathode exhibits high specific capacities of 980, 864, 771, and 592 mA h g_(S)⁻¹ at 0.2 C, 0.5 C, 1C, and 2C, respectively. Figure 5.8b shows the long-term cycling performance of the Na₂S₆@ACC cathode at 0.5 C, delivering an initial specific capacity of 866 mA h g_(S)⁻¹ and retaining 678 mA h g_(S)⁻¹ after 700 cycles, indicating a capacity decay rate of only 0.03% per cycle.

5.2.3 Understanding the catalytic behaviour of Na₂S₆@ACC cathode

During repeated cyclic voltammetry scanning (Figure 5.4b), the Na₂S₆@ACC cathode exhibits a new cathodic peak at 1.97 V, along with a higher current density during the transition of middle-order sodium polysulfides to lower-order sodium polysulfides at 1.65 V. This suggests a catalytic activity of the activated carbon cloth (ACC) to accelerate the

redox conversion of the intermediate products. Activation of carbon, as carried out in this work, is well known to generate many surface carbon atoms containing unpaired electrons (also called dangling bonds), at the edge of basal planes where bonding in the plane is terminated.^{35–38} These radical species can act as active sites to chemically interact with reactant species.^{37,38} We hypothesize that this prominent additional redox process is observed due to the facile kinetics of electrochemical conversion of the higher-order polysulfides to the lower-order polysulfides (Na_2S_2), as described in Scheme 5.1. We propose that the activated carbon cloth anchors the trisulfur radical-monoanions from the electrolyte through free-radical coupling process and immediately converts them to the lower-order sodium polysulfides.



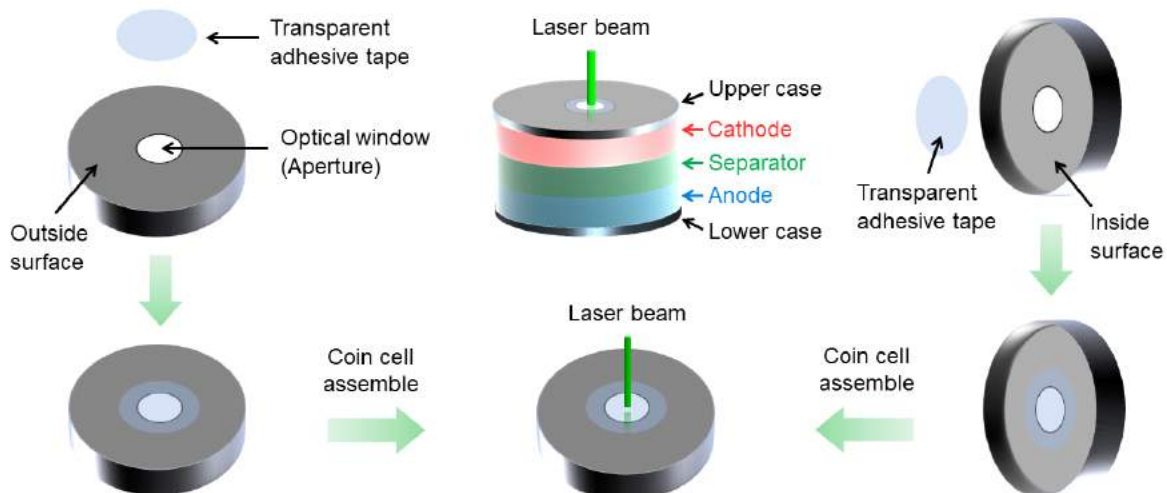
Scheme 5.1: Proposed impact of ACC on the reaction mechanism during discharge of Na_2S_6 .

During charge-discharge operation, lithium-sulfur (Li-S) batteries are well understood to involve several intermediates including the polysulfide dianions (S_n^{2-}) and the sulfur radical monoanions ($\text{S}_n^{\bullet-}$).^{31,32,39–45} A major fraction of higher- and middle-order polysulfides (i.e., S_n^{2-} , $4 \leq n \leq 6$) readily undergo an entropy driven dissociation process to generate $\text{S}_n^{\bullet-}$ species.³¹ Assuming the formation of similar sulfur radical monoanions in the Na-S discharge, it is therefore possible that a catalytic behaviour of the $\text{Na}_2\text{S}_6@\text{ACC}$ cathode may arise from free-radical coupling between ACC and these $\text{S}_n^{\bullet-}$ species. To validate this hypothesis, we carried out an *in-situ* Raman study during discharge to first confirm the formation of sulfur radical monoanions as one of the major intermediate products. The fabrication of a coin cell containing an optical window for *in-situ* Raman experiment is schematically described in Figure 5.9a. The acquired Raman spectra for an Na-S battery containing $\text{Na}_2\text{S}_6@\text{ACC}$ cathode are collectively shown in Figure 5.9b. At open circuit voltage, the RT Na-S batteries showed two major peaks at 441 and 477 cm^{-1} , which are related to the starting material, Na_2S_6 .^{46–48} The appearance of a characteristic peak at 518 cm^{-1} could be ascribed to the presence of $\text{S}_3^{\bullet-}$ radical monoanions in the catholyte.^{44,49} In aprotic

solvents with high donor number (such as TEGDME), the dissolved S_6^{2-} can produce $S_3^{\bullet-}$ radical monoanions through a disproportionation reaction.³¹ During discharge, the intensity of the characteristic peaks of Na_2S_6 reduced, while the peak intensity of the $S_3^{\bullet-}$ species was found to reach a maximum at 1.85 V. This indicates that the conversion of S_6^{2-} dianions to the $S_3^{\bullet-}$ radical monoanions becomes energetically favourable at lower potentials. However, during continuous discharge, intensity of the Raman peak at 518 cm^{-1} due to the $S_3^{\bullet-}$ radical-monoanions gradually decreases, suggesting a further reduction and consumption of $S_3^{\bullet-}$ species. Appearance of a new pair of broad peaks at 377 and 418 cm^{-1} at 1.6 V could be assigned to the formation of lower-order sodium sulfides (Na_2S_n , $1 \leq n \leq 2$) as deep discharged products.⁴⁸ It can be noticed that due to insolubility of the lower-order sodium polysulfides in the electrolyte, these intermediates become less Raman-active, showing weak and broad characteristic peaks.

After confirming the formation of $S_3^{\bullet-}$ radical monoanions from *in-situ* Raman spectra analysis, electron spin resonance (ESR) spectroscopy was employed to further confirm the existence of polysulfide radical monoanions in the as-prepared catholytes, as well as to investigate the generation of dangling bonds in activated carbon cloth upon chemical treatment. Figure 5.10a represents the ESR spectra of the pristine carbon cloth, partially activated carbon cloth and strongly activated carbon cloth. The pristine carbon cloth shows no ESR signal, indicating absence of free-radicals. Interestingly, the partially activated carbon cloth exhibited a small and broad signal. The origin of the ESR signal is attributed to the formation of the dangling bonds containing unpaired electrons in the carbon structure during chemical activation. The ESR signal was found to be strong and sharp with increasing the extent of activation of carbon cloth, presumably due to the formation of a higher number of the dangling bonds.^{35,36} Figure 5.10b shows the ESR activity of two different chemically synthesized representative catholytes (i.e., Na_2S_4 and Na_2S_6). Both the catholytes show strong ESR signals, which indicate that the polysulfide dianions tend to undergo homolytic bond cleavage to generate paramagnetic polysulfide radical monoanions.

a) In-situ coin cell structure



b) Raman spectra of Na-S cell during discharge

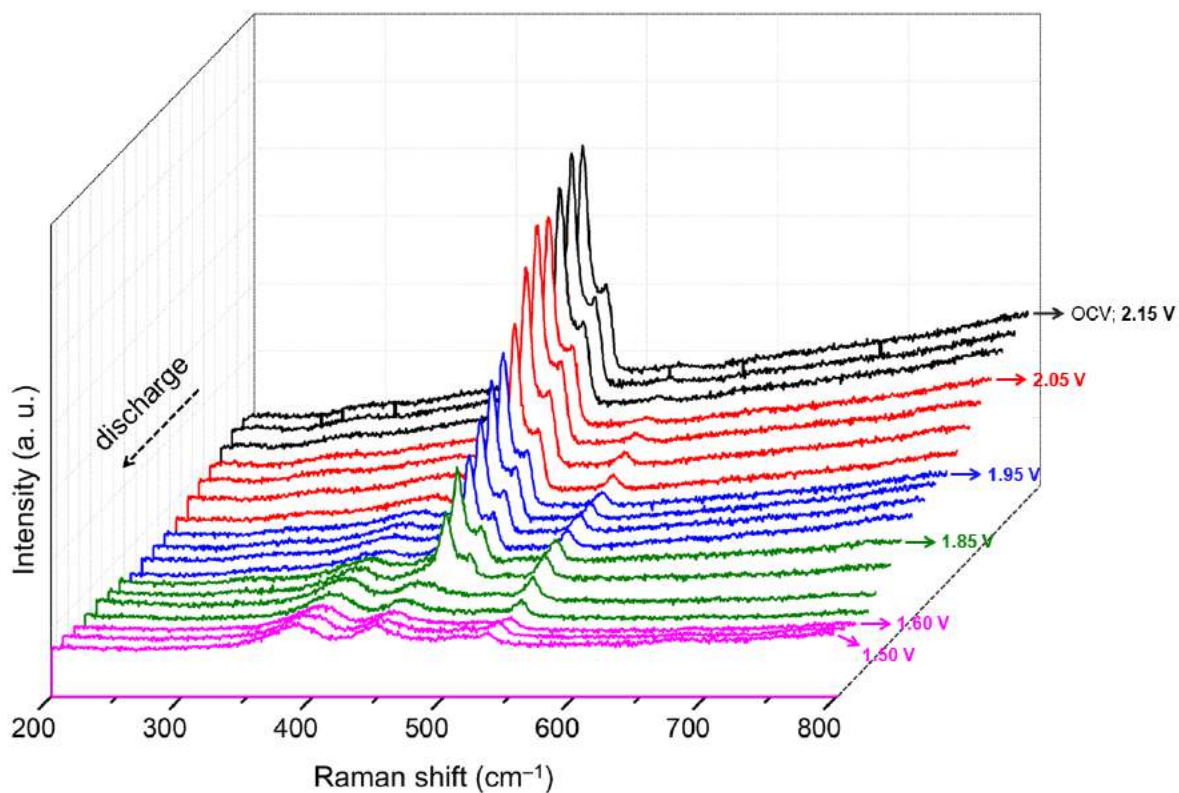


Figure 5.9: (a) Schematic of *in-situ* coin cell fabrication; (b) *in-situ* Raman spectra of the RT Na-S battery containing $\text{Na}_2\text{S}_6@\text{ACC}$ cathode at 0.1C.

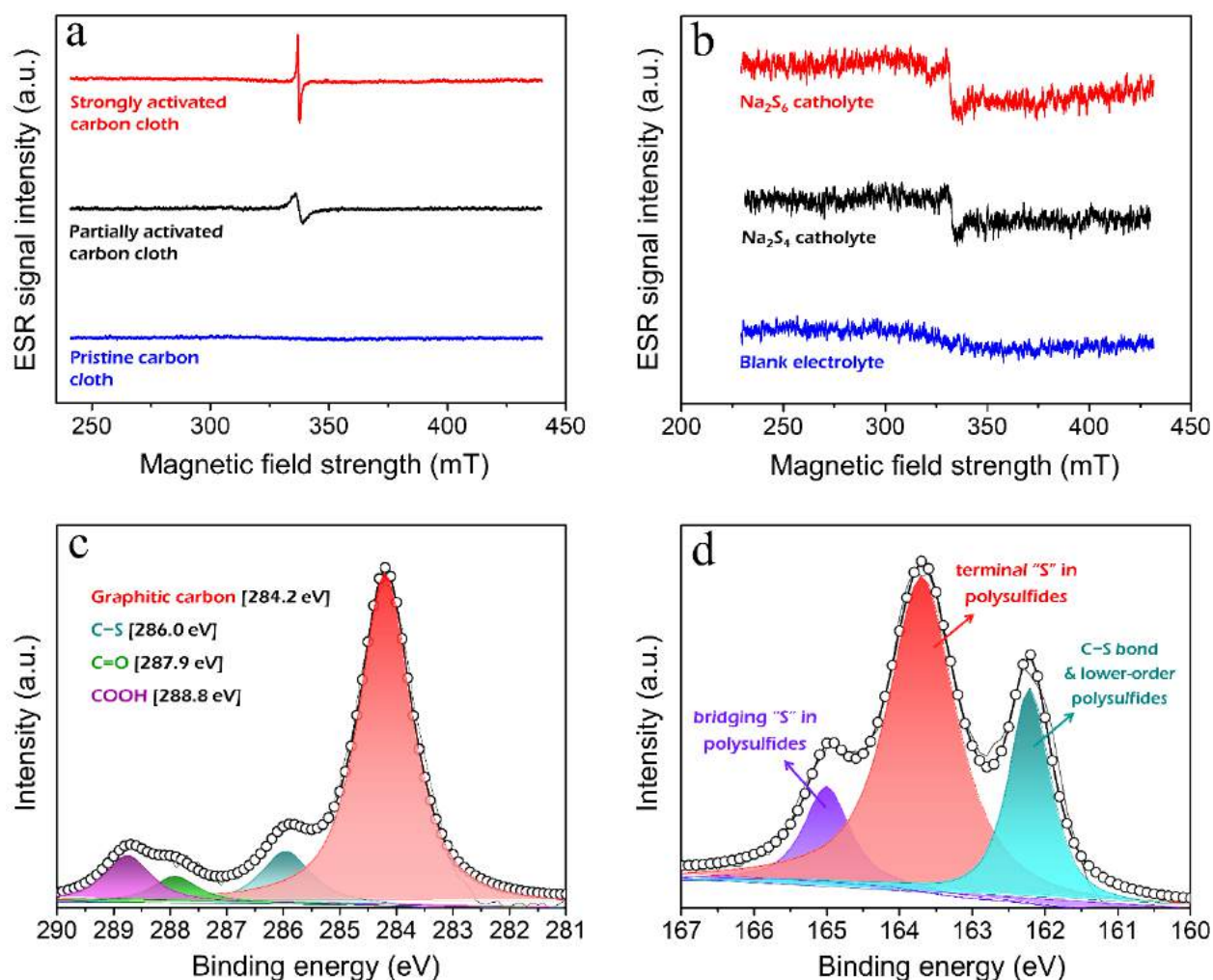


Figure 5.10: (a) ESR spectra of pristine carbon cloth, partially activated carbon cloth and strongly activated carbon cloth; (b) ESR spectra of blank electrolyte, Na_2S_4 and Na_2S_6 catholytes; (c) deconvoluted $\text{C}1\text{s}$ spectrum; and (d) deconvoluted $\text{S } 2\text{p}_{3/2}$ spectrum of $\text{Na}_2\text{S}_6@\text{ACC}$ cathode after discharged to 1.8 V.

To further gain insight into the chemical bond formation between the unsaturated carbon atoms present in the activated carbon cloth and the $\text{S}_3^{\cdot-}$ radical monoanions through free-radical coupling, ex-situ XPS spectra were acquired on the $\text{Na}_2\text{S}_6@\text{ACC}$ cathode, after discharging the Na-S@ACC battery to 1.8 V (i.e., after completion of the middle discharge reaction plateau). Figure 5.10c depicts the deconvoluted $\text{C}1\text{s}$ spectrum of the discharged $\text{Na}_2\text{S}_6@\text{ACC}$ cathode. The $\text{C}1\text{s}$ spectrum of the $\text{Na}_2\text{S}_6@\text{ACC}$ cathode exhibits an additional peak at 286.0 eV, corresponding to formation of C-S bond.^{20,50} The formation of C-S bond is only possible through coupling of the unpaired electrons present on

activated carbon cloth and $S_3^{\cdot-}$ radical monoanions. The deconvoluted S 2p_{3/2} spectrum of the Na₂S₆@ACC cathode after discharging to 1.8 V, consists of three major peak components at different binding energies (Figure 5.10d). The peaks at the binding energies of 163.7 and 164.9 eV are due to the terminal and bridging sulfur atoms, respectively, in higher-order polysulfides. The S2p_{3/2} XPS peak at the lower binding energy of 162.2 eV could be ascribed to the formation of C–S bond along with formation of lower-order sodium polysulfides, suggesting a catalytic conversion of high-order polysulfides to lower-order polysulfides by the ACC current collector. To confirm the phase of the product formed at 1.8 V, XRD patterns were recorded on both the Na₂S₆@PCC and Na₂S₆@ACC cathodes after discharging to 1.8 V. The XRD pattern of the Na₂S₆@ACC cathode shows the characteristic diffraction peaks of the insoluble Na₂S₂ product phase,⁵¹ indicating the catalytic conversion of higher- and middle-order sodium polysulfides by the ACC current collector (Figure 5.11).

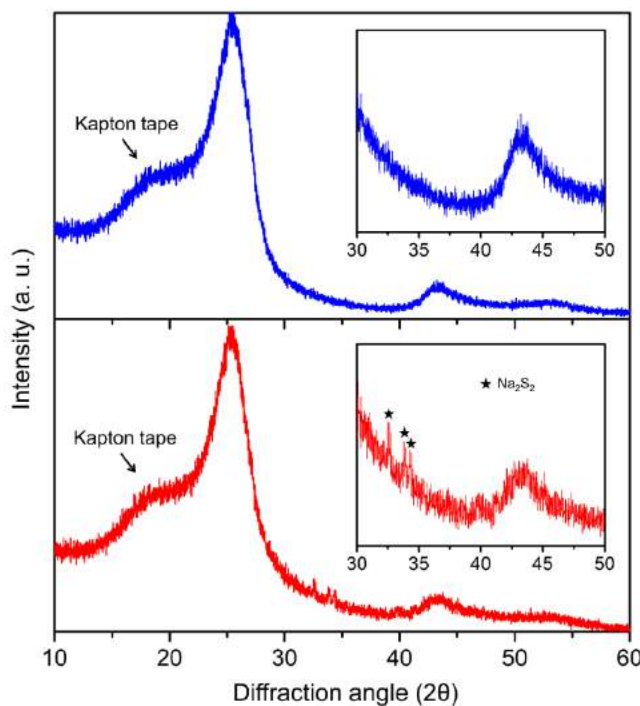


Figure 5.11: XRD pattern of Na₂S₆@PCC cathode (blue) and Na₂S₆@ACC cathode (red) after discharge to 1.8 V.

However, the $\text{Na}_2\text{S}_6@\text{PCC}$ cathode after discharge to 1.8 V, did not exhibit any diffraction peak of the insoluble product phase of lower-order sodium sulfides (Figure 5.11). This suggests that PCC is unable to promote the conversion of higher- and middle-order sodium polysulfides to the lower-order sodium sulfides (Na_2S_n , $1 \leq n \leq 2$).

To investigate whether the dangling bonds in ACC can be regenerated through homolytic bond cleavage of the C–S bonds during re-charge, the C1s XPS spectrum was recorded on the $\text{Na}_2\text{S}_6@\text{ACC}$ cathode at different states of charge (Figure 5.12).

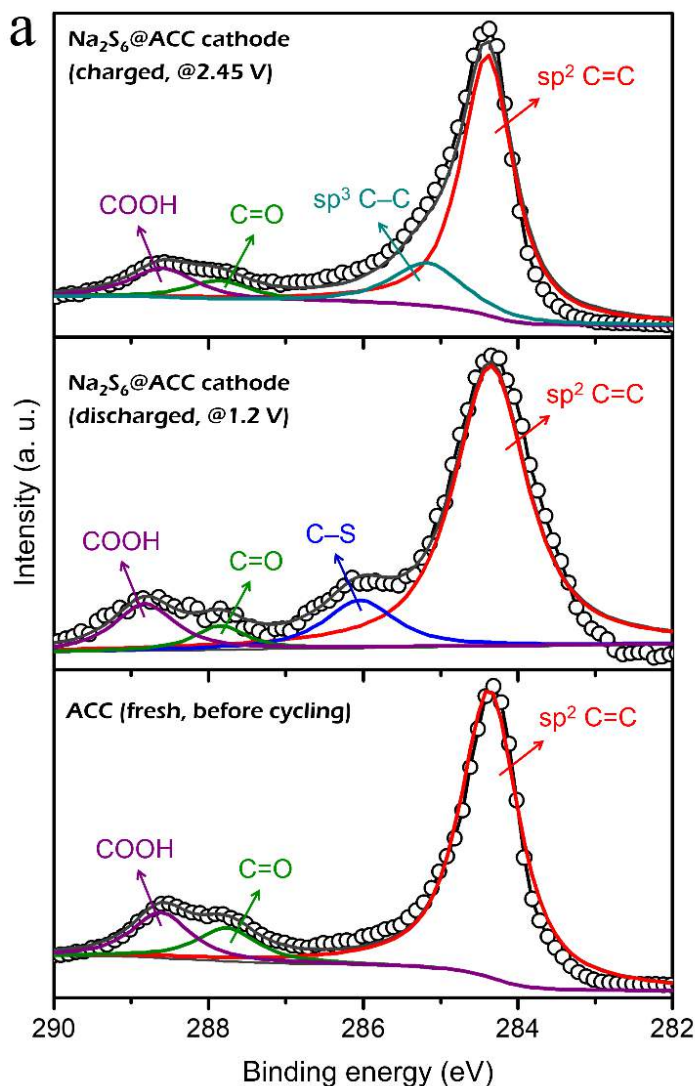


Figure 5.12: C1s XPS spectra of fresh ACC, fully discharged $\text{Na}_2\text{S}_6@\text{ACC}$ cathode and fully re-charged $\text{Na}_2\text{S}_6@\text{ACC}$ cathode

The fresh ACC shows the characteristic C1s XPS peaks of sp^2 C=C (284.3 eV), C=O (287.7 eV) and COOH (288.6 eV) (Figure 5.12). The fully discharged $Na_2S_6@ACC$ cathode exhibits an additional C1s XPS peak at 286.0 eV, indicating that the C–S bonds still exist at 1.2 V (Figure 5.12). This peak disappeared after recharging the Na-S@ACC cell to 2.45 V (Figure 5.12). This indicates that during recharging the Na-S battery, the C–S bonds are dissociated to regenerate the dangling bonds in ACC, which become available to take part free-radical catalysis process during subsequent discharge processes.

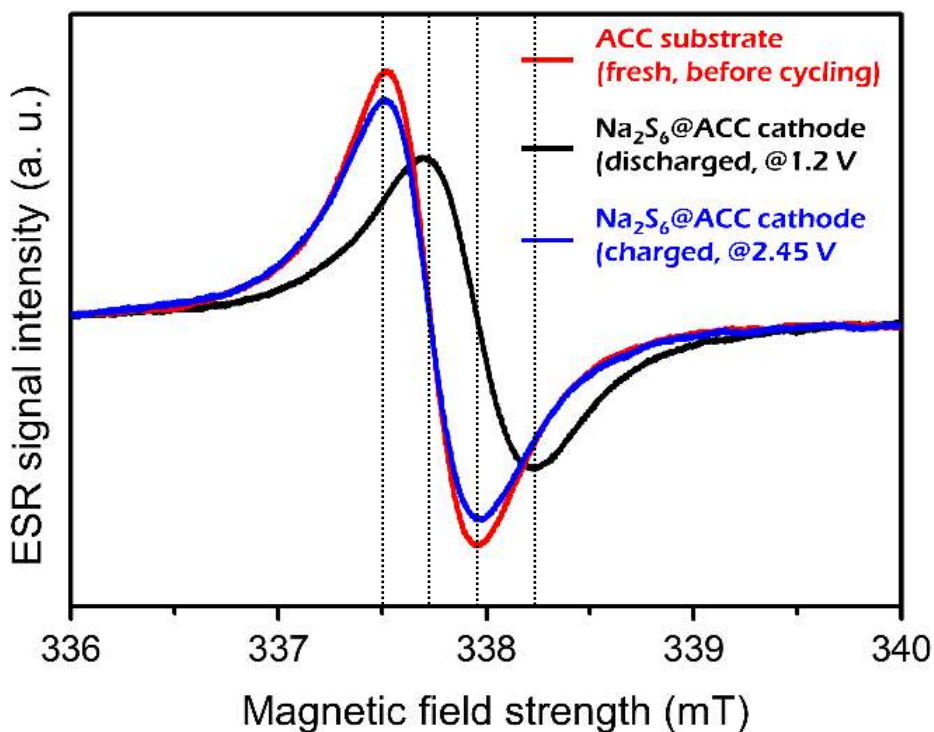


Figure 5.13: ESR spectra of fresh ACC (red), fully discharged $Na_2S_6@ACC$ cathode (black) and fully re-charged $Na_2S_6@ACC$ cathode (blue).

To provide further evidence of this mechanism we have collected the ESR spectra of the $Na_2S_6@ACC$ cathode at various states of charge/discharge. The ESR spectrum of activated carbon cloth (ACC) before cycling exhibits sharp peaks with g -value = 2.0008 (Figure 5.13). All the preliminary features of the ESR spectrum (i.e., peak intensity, g -value, peak position and linewidth) were altered significantly in the deep discharged $Na_2S_6@ACC$ cathode (Figure 5.13). The suppressed peak intensity, shift in peak position

with characteristic broader linewidth, and lower g-value, all strongly indicate the possible formation of C–S bonds through free-radical coupling. This can be expected to decrease the intensity of the ACC ESR signal (Figure 5.13). Changes in the chemical environment causes the peak position shift, broadening of linewidth and decreasing g-value. The ESR spectrum of the fully re-charged $\text{Na}_2\text{S}_6@\text{ACC}$ cathode is similar to that of the fresh ACC current collector, indicating the regeneration of paramagnetic dangling bonds in the ACC during charge process (Figure 5.13).

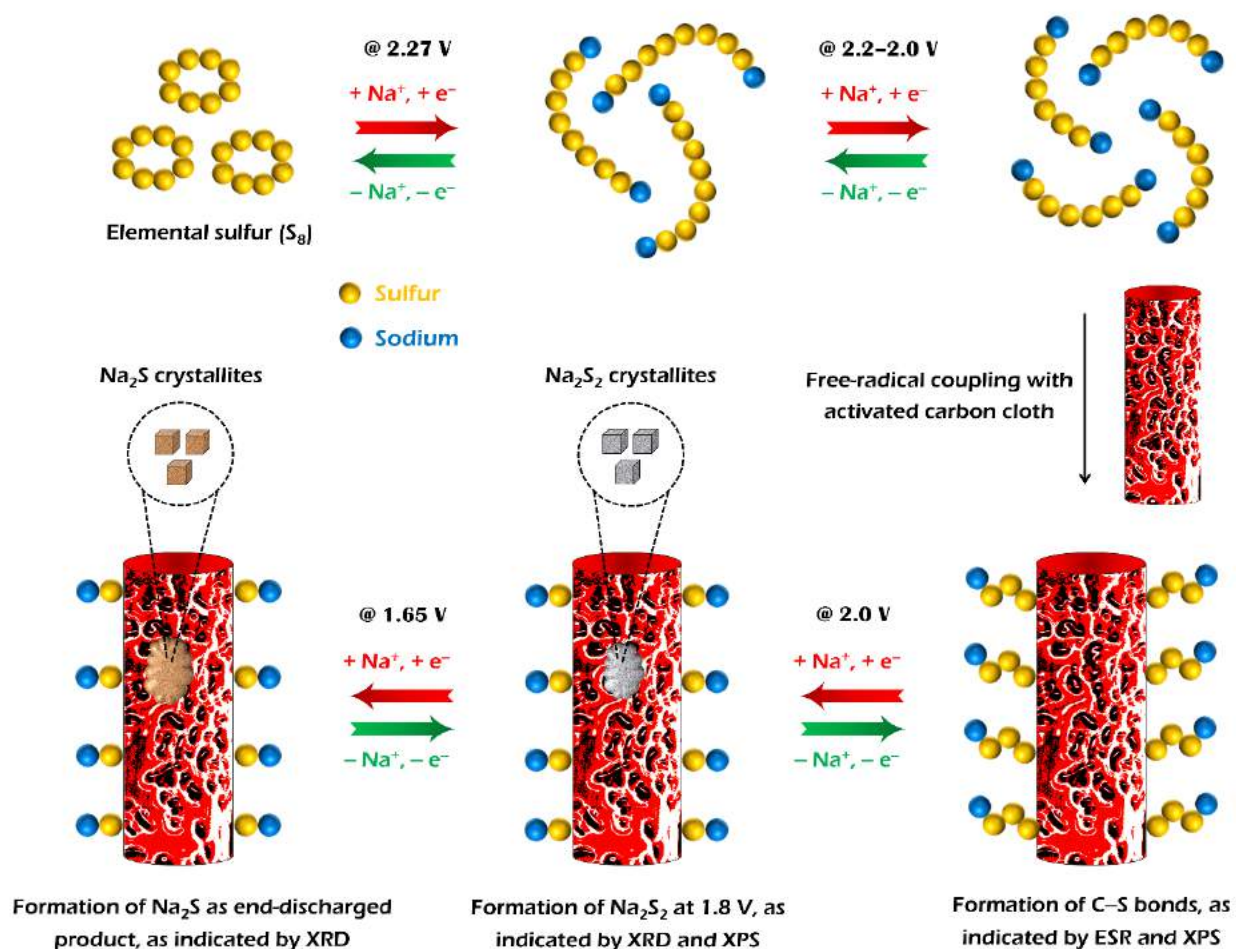


Figure 5.14: Reaction mechanism describing the catalytic effect of the ACC in the $\text{Na}_2\text{S}_6@\text{ACC}$ cathode.

In summary, as schematically illustrated in Figure 5.14, during discharge of a Na-S@ACC battery, the Raman evidence suggests that the Na_2S_6 species undergoes a homolytic bond dissociation process to produce the relatively stable $\text{S}_3^{\cdot-}$ radical

monoanion. Subsequently, the changes observed in the ESR and XPS spectra, indicate formation of C-S bonds on the surface of the ACC, anchoring the $\text{S}_3^- \text{Na}^+$ species from the electrolyte. This anchoring of the S_3^- species facilitates electron transfer from the substrate to carry out the further reduction of the sulfur to form Na_2S_2 and eventually to Na_2S as the end-discharged product. The latter is confirmed by the characteristic diffraction peaks^{14, 51} in the XRD pattern acquired on a completely discharged $\text{Na}_2\text{S}_6@\text{ACC}$ cathode (Figure 5.15)

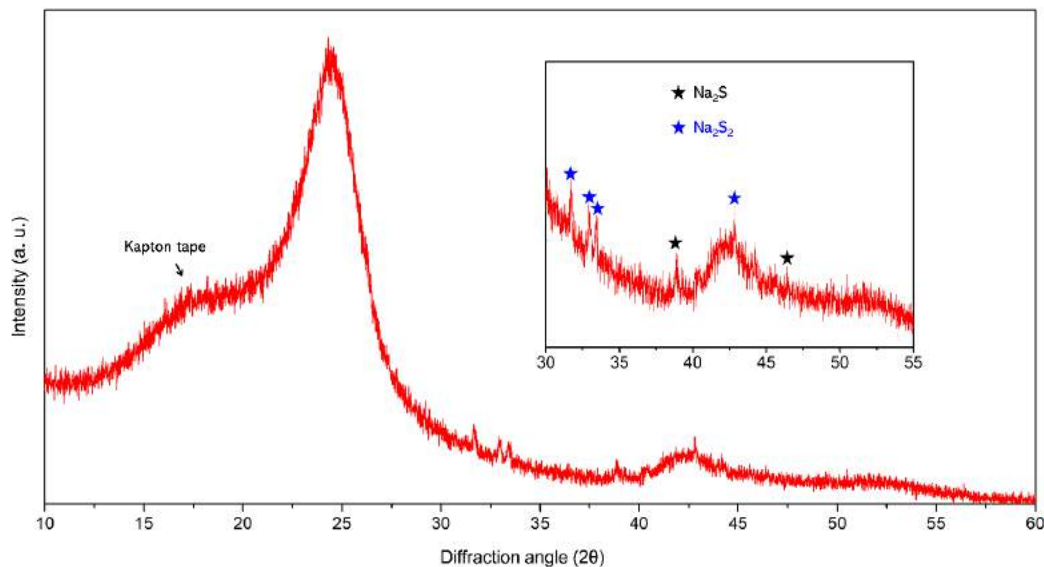


Figure 5.15: XRD pattern of $\text{Na}_2\text{S}_6@\text{ACC}$ cathode after discharging to 1.2 V. The XRD pattern confirms the complete reduction of sulfur to lower-order sodium polysulfides (Na_2S_2 and Na_2S) as fully discharged products.

A fraction ($1/3^{\text{rd}}$) of the sulfur remains attached to the ACC in the form of $\text{C-S}^- \text{Na}^+$; this reduces the theoretical capacity to 1393 mA h g^{-1} , which is still significantly higher than is practically achieved here (second cycle reversible capacity $\sim 980 \text{ mA h g}^{-1}$). ESR and XPS show that the dangling bonds in the ACC catalyst are subsequently readily regenerated through homolytic cleavage of the C-S bonds during charging of Na-S batteries.

5.2.4 Post-cycling characterization of $\text{Na}_2\text{S}_6@\text{ACC}$ cathode

To further understand the extremely stable cycling performance of the $\text{Na}_2\text{S}_6@\text{ACC}$ cathode in the RT Na-S batteries, microstructure and morphology of the $\text{Na}_2\text{S}_6@\text{ACC}$

cathode after charge-discharge cycling were investigated using scanning electron microscopy (Figure 5.16).

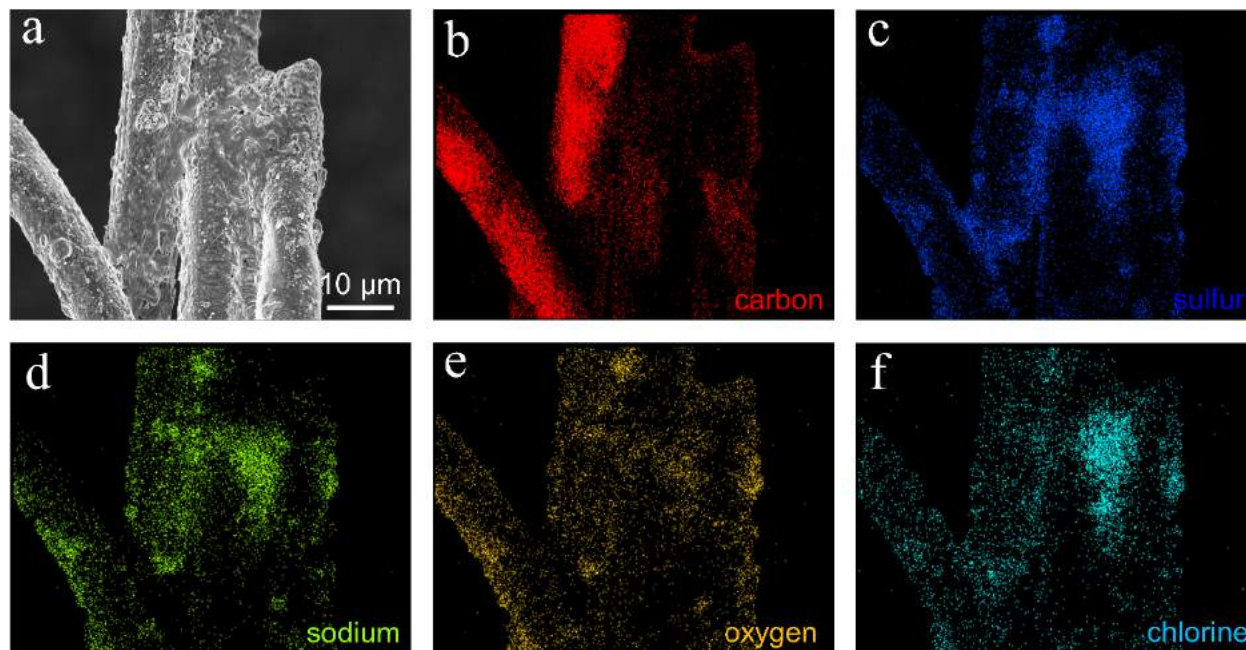


Figure 5.16: (a) Scanning electron microscopy image of Na₂S₆@ACC cathode after 700 cycles, at fully discharged state; (b–f) mapping of different elements taken on the cycled electrode.

Figure 5.16a represents the SEM image of the Na₂S₆@ACC cathode after 700 cycles, in a fully discharge state. It is noteworthy that the activated carbon cloth maintains the mechanical integrity of the electrode, even after long-term cycling. Moreover, it can be observed that a dense product was deposited on the surface of the activated carbon cloth. Sulfur and sodium mappings (Figure 5.16c and d) revealed that the dense product was in fact the mixed phase of sodium polysulfides, which have been uniformly deposited on the surface of the activated carbon cloth.

5.3 Conclusions

Room temperature sodium-sulfur batteries achieving a high nominal cell potential of 1.85 V have been successfully demonstrated using an activated carbon cloth as current collector and polysulfide reservoir. The activated carbon cloth significantly catalyzes the conversion

of intermediate trisulfur radical monoanions to the end-discharge products. Electron spin resonance spectroscopy reveals the existence of carbon atoms containing unpaired electrons in the activated carbon cloth and *in-situ* Raman spectroscopy confirms the formation of the $S_3^{\cdot-}$ radical monoanions during discharge. We propose that a coupling between the unpaired electrons of activated carbon cloth and trisulfur radical monoanions is responsible for observed catalytic enhancement in the kinetics, addressing several major issues that face these batteries. The achievement of an increased nominal cell potential, combined with excellent specific capacity and capacity retention at practical rates, produce a step forward in cell energy density with extremely stable cycle life. These properties, combined with inexpensive starting materials and manufacturing should propel the RT Na-S battery closer to practical application.

References

1. C.W. Park, J. H. Ahn, H.S. Ryu, K. W. Kim and H. J. Ahn, *Electrochem. Solid-State Lett.*, 2006, 9, A123.
2. S. Wenzel, H. Metelmann, C. Reiß, C., A. K. Durr, J. Janek and P. Adelhelm, *J. Power Sources*, 2013, 243, 758.
3. S. Xin, Y. X. Yin, Y.G. Guo and L. J. Wan, *Adv. Mater.*, 2014, 26, 1261.
4. X. Yu and A. Manthiram, *J. Phys. Chem. C*, 2014, 118, 22952.
5. B. W. Zhang, T. Sheng, Y. D. Liu, Y. X. Wang, L. Zhang, W. H Lai, L. Wang, J. P. Yang, Q. F. Gu, S. L. Chou, H. K. Liu and S.-X. Dou, *Nat. Commun.*, 2018, 9, 4082.
6. X. Yu and A. Manthiram, *Adv. Energy Mater.*, 2015, 5, 1500350.
7. B. W. Zhang, T. Sheng, Y. X. Wang, S. Chou, K. Davey, S.-X. Dou and S.-Z. Qiao, *Angew. Chem. Int. Ed.*, 2019, 58, 1484.
8. A. Manthiram and X. Yu, *Small*, 2015, 11, 2108.
9. I. Kim, J. Y. Park, C. H. Kim, J. W. Park, J. P. Ahn, J. H. Ahn, K.W. Kim and H.J. Ahn, *J. Power Sources*, 2016, 301, 332.
10. I. Kim, C. H. Kim, S. H. Choi, J. P. Ahn, J. H. Ahn, K. W. Kim, E. J. Cairns, and H. J. Ahn, *J. Power Sources*, 2016, 307, 31.
11. S. Wei, S. Xu, A. Agrawal, S. Choudhury, Y. Lu, Z. Tu, L. Ma and L. A. Archer, *Nat. Commun.*, 2016, 7, 11722.
12. Y.-X. Wang, J. Yang, W. Lai, S.-L. Chou, Q.-F. Gu, H. K. Liu, D. Zhao and S. X. Dou, *J. Am. Chem. Soc.* 2016, 138, 16576.
13. I. Kim, J. Y. Park, C. H. Kim, J. W. Park, J. P. Ahn, J. H. Ahn, K. W. Kim and H. J. Ahn, *J. Electrochem. Soc.*, 2016, 163, 611.
14. X. Yu and A. Manthiram, *Chem. Mater.*, 2016, 28, 896.
15. Y. M. Chen, W. Liang, S. Li, F. Zou, S. M. Bhaway, Z. Qiang, M. Gao, B. D. Vogt and Y. Zhu, *J. Mater. Chem. A*, 2016, 4, 12471.
16. A. Ghosh, A. Kumar, A. Roy, M. R. Panda, M. Kar, D. R. MacFarlane and S. Mitra, *ACS Appl. Mater. Interfaces*, 2019, 11, 14101.
17. Z. Qiang, Y. M. Chen, Y. Xia, W. Liang, Y. Zhu and B. D. Vogt, *Nano Energy*, 2017, 32, 59.
18. T. H. Hwang, D. S. Jung, J. S. Kim, B. G. Kim and J. W. Choi, *Nano Lett.*, 2013, 13, 4532.

19. R. Carter, L. Oakes, A. Douglas, N. Muralidharan, A. P. Cohn and C. L. Pint, *Nano Lett.* 2017, 17, 1863.
20. A. Ghosh, S. Shukla, M. Monisha, A. Kumar, B. Lochab and S. Mitra, *ACS Energy Lett.*, 2017, 2, 2478.
21. A. Kumar, A. Ghosh, A. Roy, M. R. Panda, M. Forsyth, D. R. MacFarlane and S. Mitra, *Energy Storage Mater.*, 2019, 20, 196.
22. D. Ma, Y. Li, J. Yang, H. Mi, S. Luo, L. Deng, C. Yan, M. Rauf, P. Zhang, X. Sun, X. Ren, J. Li and H. Zhang, *Adv. Funct. Mater.*, 2018, 28, 1705537.
23. W. Bao, C. E. Shuck, W. Zhang, X. Guo, Y. Gogotsi and G. Wang, *ACS Nano.*, 2019, 13, 11500.
24. X. F. Xu, D. Zhou, X. Y. Qin, K. Lin, F. Y. Kang, B. H. Li, D. Shanmukaraj, T. Rojo, M. Armand and G. X. Wang, *Nat. Commun.*, 2018, 9, 3870.
25. H. Ryu, T. Kim, K. Kim, J.-H. Ahn, T. Nam, G. Wang and H.-J. Ahn, *J. Power Sources*, 2011, 196, 5186.
26. Z. W. Seh, J. Sun, Y. Sun and Y. Cui, *ACS Cent. Sci.*, 2015, 1, 449.
27. L. Gao, H. Lu, H. Lin, X. Sun, J. Xu, D. Liu, and Y. Li, *Chem. Res. Chin. Univ.*, 2014, 30, 441.
28. M. A. Lillo-Rodenas, D. Cazorla-Amoros and A. Linares-Solano, *Carbon*, 2003, 41, 267.
29. X. Yu and A. Manthiram, *ChemElectroChem*, 2014, 1, 1275.
30. T. Chivers, *Nature*, 1974, 252, 32.
31. T. Chivers and P. J. W. Elder, *Chem. Soc. Rev.*, 2013, 42, 5996.
32. M. Vijayakumar, N. Govind, E. Walter, S. D. Burton, A. Shukla, A. Devaraj and S. Thevuthasan, *Phys. Chem. Chem. Phys.*, 2014, 16, 10923.
33. R. Steudel and T. Chivers, *Chem. Soc. Rev.*, 2019, 48, 3279.
34. L. Xue, S. Xin, J. B. Goodenough and C. A. Angell, *ACS Energy Lett.*, 2017, 2, 1534.
35. A. Manivannan, M. Chirila, N. C. Giles, M. S. Seehra, *Carbon*, 1999, 37, 1741.
36. O. Chauvert, L. Forro, *Physical Review B (Condensed Matter and Materials Physics)*, 1995, 52, R6963.
37. W.-T. Zheng and C. Q. Sun, *Energy Environ. Sci.*, 2011, 4, 627.

38. Y. Mao, H. Duan, B. Xu, L. Zhang, Y. Hu, C. Zhao, Z. Wang, L. Chen and Y. Yang, *Energy Environ. Sci.*, 2012, 5, 7950.
39. K. H. Wujcik, D. R. Wang, A. Raghunathan, M. Drake, T. A. Pascal, D. Prendergast and N. P. Balsara, *J. Phys. Chem. C*, 2016, 120, 18403.
40. Q. Wang, J. Zheng, E. Walter, H. Pan, D. Lv, P. Zuo, H. Chen, Z. D. Deng, B. Y. Liaw, X. Yu, X. Yang, J.-G. Zhang, J. Liu and J. Xiao, *J. Electrochem. Soc.*, 2015, 162, A474.
41. M. Barghamadi, A. S. Best, A. I. Bhatt, A. F. Hollenkamp, M. Musameh, R. J. Rees and T. Ruther, *Energy Environ. Sci.*, 2014, 7, 3902.
42. K. H. Wujcik, T. A. Pascal, C. D. Pemmaraju, D. Devaux, W. C. Stolte, N. P. Balsara and D. Prendergast, *Adv. Energy Mater.*, 2015, 5, 1500285.
43. M. Wild, L. O'Neill, T. Zhang, R. Purkayastha, G. Minton, M. Marinescu and G. J. Offer, *Energy Environ. Sci.*, 2015, 8, 3477.
44. H.-L. Wu, L. A. Huff and A. A. Gewirth, *ACS Appl. Mater. Interfaces*, 2015, 7, 1709.
45. S. Yu, X. Huang, K. Schwarz, R. Huang, T. A. Arias, J. D. Brock and H. D. Abruna, *Energy Environ. Sci.*, 2018, 11, 202.
46. O. El Jaroudi, E. Picquenard, N. Gobeltz, A. Demortier and J. Corset, *Inorg. Chem.*, 1999, 38, 2917.
47. G. J. Janz, J. R. Downey, E. Roduner, G. J. Wasilczyk, J. W. Coutts and A. Eluard, *Inorg. Chem.*, 1976, 15, 1759.
48. X. Lu, B. W. Kirby, W. Xu, G. Li, J. Y. Kim, J. P. Lemmon, V. L. Sprenkle and Z. Yang, *Energy Environ. Sci.*, 2013, 6, 299.
49. J.-T. Yeon, J.-Y. Jang, J.-G. Han, J. Cho, K. T. Lee and N.-S. Choi, *J. Electrochem. Soc.*, 2012, 159, A1308.
50. C. Zu and A. Manthiram, *Adv. Energy Mater.*, 2013, 3, 1008.
51. H. El-Shinawi, E. J. Cussen and S. A. Corr, *Inorg. Chem.*, 2018, 57, 7499.

Chapter 6

Indium-tin-oxide (ITO) decorated activated carbon cloth as a current collector for room-temperature sodium-sulfur batteries

Chapter 6

6.1 Introduction

Sluggish diffusivity of large size Na^+ ion; among the rapid dissolution of sodium polysulfides, and poor electronic conductivity (sulfur and polysulfides) are the major drawbacks leading to the low capacity and short cycle life¹⁻¹⁰. Many strategies have been attempted to overcome the aforementioned obstacles; Including the different infusion types of sulfur into a porous and/or heteroatom doped carbonaceous conductive matrix, that were found to enhance the electron availability and provide enough space to physically accommodate intermediate polysulfides^{11, 12}. However, these cathode constructions suffer from slow reaction kinetics which not only results in poor cell capacity but also causes low cell voltage. Therefore, witnessing the fact that the electrochemical conversion of active material is dependent on the housing facility of the electron conductive cathode additive, it is essential to develop an active materials host, which not only enable robust binding sites for polysulfides along with an effective electron conductive network, but also endorses the reaction kinetics between sodium and sulfur.

Herein, we report an activated carbon cloth decorated with ITO nanoparticles as electron conducting sulfiphilic host to catalyze the redox conversion of elemental sulfur (S_8) to the end-discharged product, Na_2S . Due to the good tendency of homogeneous and superficial distribution, liquid-phase sodium polysulfide (Na_2S_6) catholyte was used as active material in RT Na-S batteries. The usage of activated carbon cloth as a current collector could significantly improve the electronic conductivity of electrode material throughout the cathode scaffold and hence enhance the active sulfur utilization. The ITO nanoparticles grown on the surface of activated carbon cloth could chemically interact with polysulfides to restrict their gradual dissolution. To investigate further, Cyclic voltammetry coupled with electron spin resonance (ESR) spectroscopy and X-ray photoelectron spectroscopy (XPS) was utilized, and the data revealed that the activated carbon cloth substantially facilitates the redox conversion of intermediate polysulfides through free-radical catalysis. The RT Na-S batteries, containing Na_2S_6 catholyte infiltrated activated carbon cloth ($\text{ACC@ITO@Na}_2\text{S}_6$), delivers a high specific capacity of 1036 mA h g^{-1} during the second cycle and retains 931 mA h g^{-1} after 1000 cycles, with an extremely low rate of capacity decay of 0.01% per cycle. Owing to the conducting ceramic (ITO nano-particles) and activated carbon cloth, the performance of these batteries is much better than the modified RT Na-S batteries explained earlier in this report.

6.2 Results and discussion

6.2.1 Synthesis and characterization

To fabricate liquid-phase catholyte adsorbed in indium tin oxide (ITO) decorated activated carbon cloth (ACC@ITO@Na₂S₆), the ITO decorated carbon cloth (ACC@ITO) was first prepared by following a hydrothermal synthesis procedure. Upon successful preparation of ACC@ITO flexible substrate, Na₂S₆ catholyte was incorporated and allowed to get adsorbed before the complete cell assembly. A schematic illustration of the preparation procedure of the ACC@ITO@Na₂S₆ cathode is shown in Figure 6.1. The microstructure and morphology of the as-prepared products involved in each step of the preparation, as shown in Figure 1, were investigated using the different modes of electron microscopy. Scanning electron microscopy (SEM) images acquired at different magnification reveal the hydrothermal method followed by heat treatment at 1000 °C, strongly eroded the surface as well as the edge of each carbon fiber to create plenty of micropores (Figure 6.2a-d). Moreover, from the high-resolution SEM image deposition of ITO nanoparticles on the surface of activated carbon cloth can be clearly observed (Figure 6.2c). More interestingly, the high-resolution SEM image captured at the edge of a carbon fiber exhibits that the nano-tunnels have been created inside the core (Figure 6.2d).

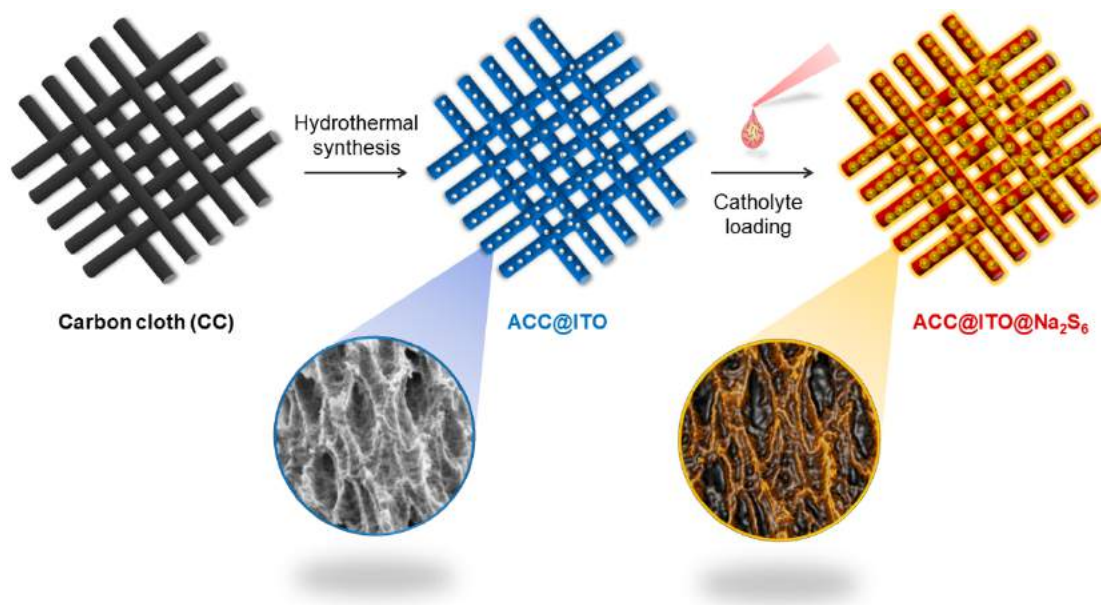


Figure 6.1: Schematic representation of pristine carbon cloth (CC), activated carbon cloth decorated with tin-doped indium-oxide nanoparticle (ACC@ITO) and catholyte loaded on activated carbon cloth decorated with tin-doped indium-oxide nanoparticle (ACC@ITO@Na₂S₆).

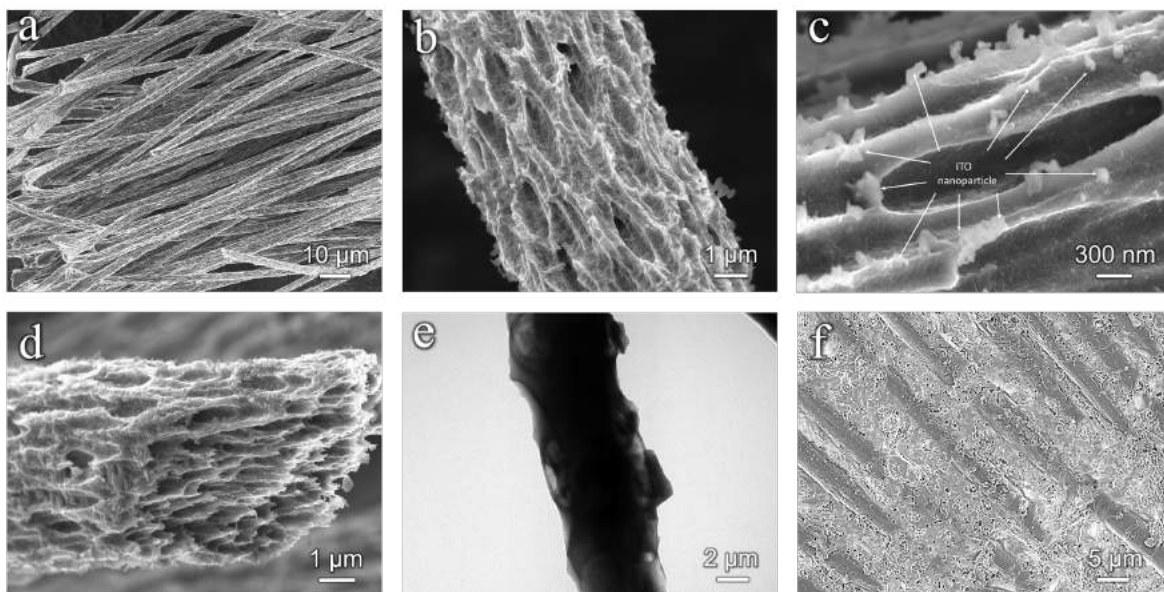


Figure 6.2: (a–d) SEM images and (e) TEM image of activated carbon cloth decorated with tin-doped indium-oxide nanoparticle (ACC@ITO) and (f) ACC@ITO@Na₂S₆ cathode.

The TEM image shows a similar porous and eroded morphology as observed from the SEM images (Figure 6.2e). Due to homogeneity and facile dispersibility of liquid-phase catholyte, it is anticipated that the micro-sized pits and nano-tunnels generated on the surface of carbon cloth fibers could accommodate a large amount of active material, as it can be observed from the SEM image of Na₂S₆ adsorbed ACC@ITO (Figure 6.2f). The SEM image of ACC@ITO@Na₂S₆ shows that the ITO nanoparticles and pits and nano-tunnels on the carbon fibers were entirely shielded with Na₂S₆ active material.

6.2.2 Electrochemical performances of RT Na-S batteries

The activated carbon cloth decorated with ITO nanoparticle infiltrated with Na₂S₆ catholyte (i.e., ACC@ITO@Na₂S₆) was used as a freestanding cathode with respect to sodium metal anode to operate the Na-S batteries at room temperature. To prove the advantage of the activated carbon cloth decorated with tin-doped indium-oxide nanoparticle as a current collector and the sulfur host, the electrochemical performances of a pristine carbon cloth infiltrated with Na₂S₆ catholyte (i.e., CC@Na₂S₆) were recorded and compared.

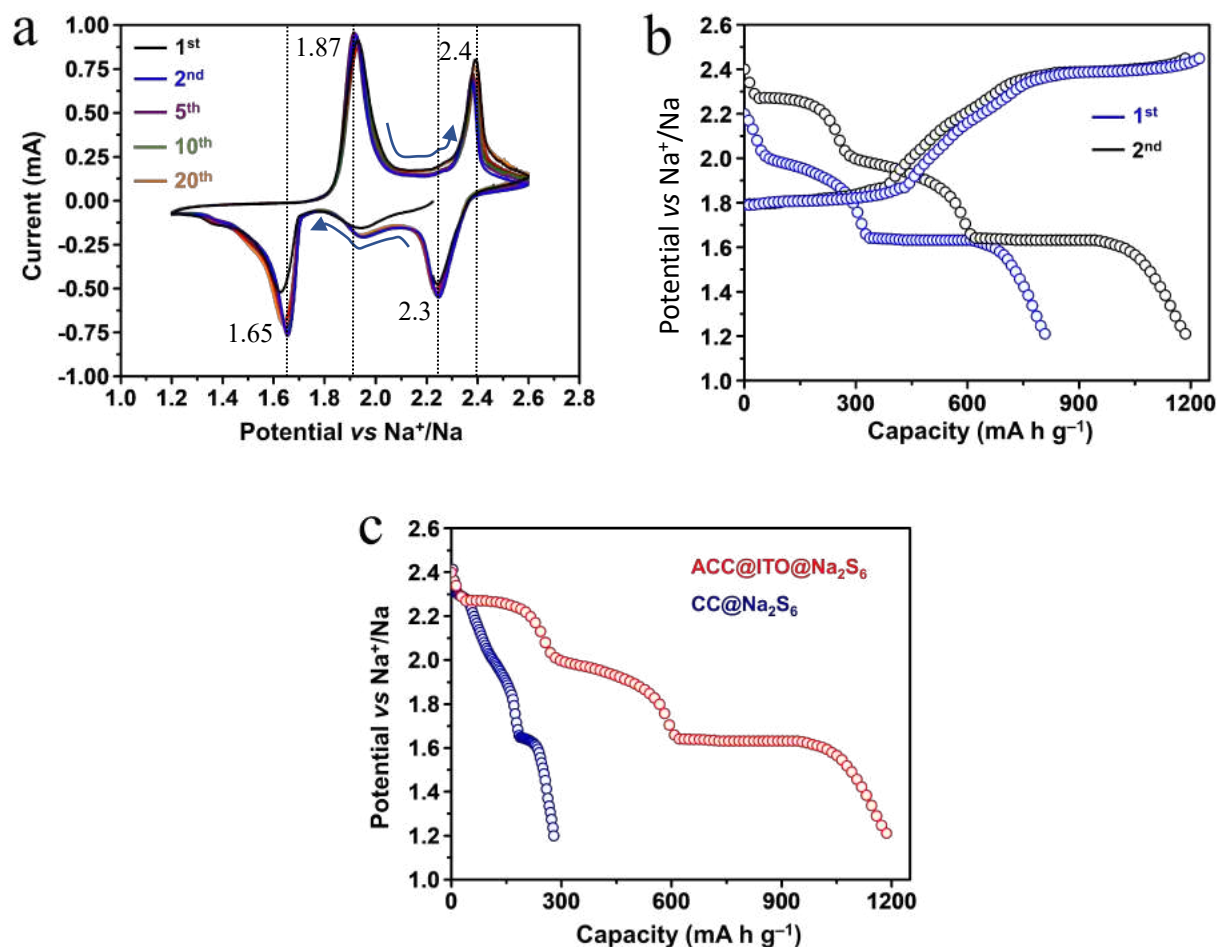


Figure 6.3: (a) Cyclic voltammograms of the ACC@ITO@ Na₂S₆ cathode at a scan rate of 0.1 mV s⁻¹; (b) charge-discharge profiles of the ACC@ITO@ Na₂S₆ cathode at 0.2 C; (c) second cycle discharge profiles of ACC@ITO@ Na₂S₆ and CC@Na₂S₆ cathodes at 0.2 C at 20°C ± 2°C.

In both cases, the RT Na-S batteries were first discharged (i.e., the Na₂S₆ catholyte was first reduced). Figure 6.3a displays the cyclic voltammograms of ACC@ITO@Na₂S₆ cathode at the scan rate of 0.1 mV s⁻¹ for the first, second, fifth, tenth and twentieth cycles. It can be clearly observed that during the cyclic voltammetry scan, the ACC@ITO@Na₂S₆ cathode revealed three reduction peaks and three oxidation peaks, maintaining their reversibility in each cycle. The additional pair of redox peaks were observed at ~1.9 V (during the cathodic scan) and ~2.0 V (during the anodic scan) which could be ascribed to facile kinetics of the electrochemical conversion reaction from Na₂S₆ (higher-order polysulfides) to the middle-order polysulfides and vice-versa²⁶. Remarkably, the above-mentioned additional pair of redox peaks were not observed in cyclic voltammograms of the CC@Na₂S₆ cathode. This observation is confirming

the catalytic activity of activated carbon cloth decorated with tin-doped indium-oxide nanoparticle (ACC@ITO) as a substrate to kinetically promote the interconversion of highly soluble long-chain polysulfides (i.e., Na_2S_6) to the moderately soluble middle-order polysulfides in RT Na-S batteries. The activated carbon cloth decorated with tin-doped indium-oxide nanoparticle, therefore, not only increases the utilization rate of active material but also controls the dissolution of highly soluble intermediates through their rapid conversion to moderately soluble species. The ACC@ITO@ Na_2S_6 cathode revealed highly intense reduction peaks at ~ 1.65 V, corresponding to the complete reduction of active material to lower-order sodium polysulfides (Na_2S_n , $1 \leq n \leq 2$). In comparison to the CC@ Na_2S_6 cathode, the relatively high intense peak at slightly higher reduction potential of ~ 1.65 V indicates the further catalytic effect of activated carbon cloth decorated with tin-doped indium-oxide nanoparticle (ACC@ITO) to greatly facilitate the sluggish conversion of liquid-phase middle-order polysulfides to the solid-phase short-chain polysulfides, which was assigned as another challenge for RT Na-S batteries.

Figure 6.3b displays the representative first and second cycle charge-discharge profiles of ACC@ITO@ Na_2S_6 cathode at 0.2 C ($1 \text{ C} = 1672 \text{ mA h g}^{-1}$) current rate. There is a large mismatch between the initial discharge capacity and the capacity obtained during subsequent charge process which might be because of the starting material (i.e., Na_2S_6) which was in sodiated form.

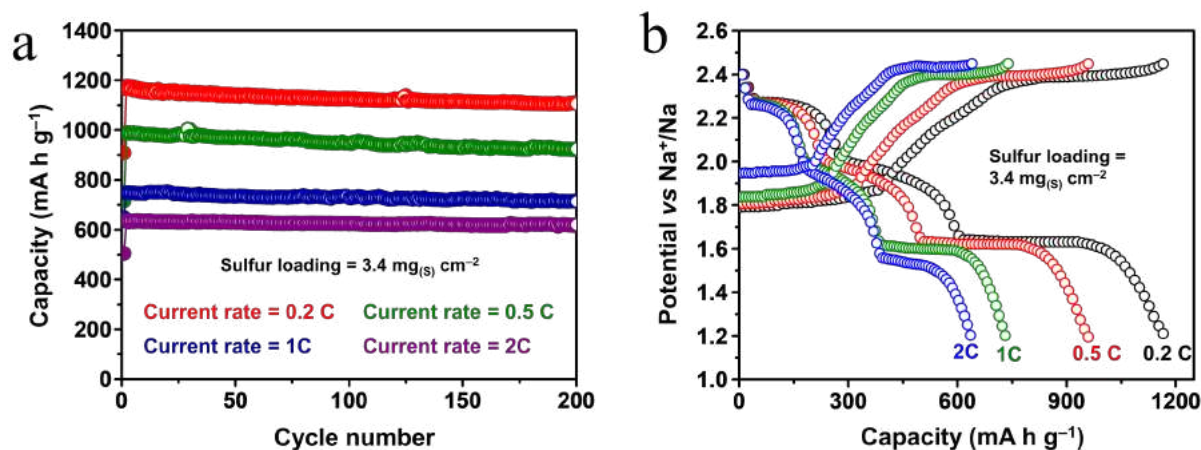


Figure 6.4: (a) cycling performance of ACC@ITO@ Na_2S_6 cathode at different current rate; (b) charge-discharge profiles of ACC@ITO@ Na_2S_6 cathode at different current rates at $20^\circ\text{C} \pm 2^\circ\text{C}$.

After the first cycle, the RT Na-S cell exhibited three discharge plateaus at ~ 2.27 V, ~ 1.9 V, and ~ 1.65 V, respectively during each discharge process. It has been observed during the cathodic scans, that the potential ranges and potential regions of three reduction peaks and discharge

plateaus respectively, match perfectly. Figure 6.3c clearly shows the difference between the discharge curve shapes of $\text{CC@Na}_2\text{S}_6$ and $\text{ACC@ITO@Na}_2\text{S}_6$ cathodes. The discharge curve of $\text{ACC@ITO@Na}_2\text{S}_6$ cathode clearly exhibits three plateaus, which reveals a kinetically facile conversion of elemental sulfur to the end-discharged products.

Figure 6.3c demonstrates the difference between the shape of discharge curves of $\text{CC@Na}_2\text{S}_6$ and $\text{ACC@ITO@Na}_2\text{S}_6$ cathodes. The discharge curve of the $\text{ACC@ITO@Na}_2\text{S}_6$ cathode clearly displays three plateaus, revealing a kinetically facile conversion of elemental sulfur to the end-discharged products (Na_2S). Catalytic conversion of sulfur in $\text{ACC@ITO@Na}_2\text{S}_6$ cathode helps RT Na-S battery to achieve a nominal cell potential of 1.85 V, calculated through an integral approach (Figure 5.6), as discussed previously^{21,27}. Achieving a high nominal cell potential can be strongly ascribed to the facile redox conversion of elemental sulfur to Na_2S .

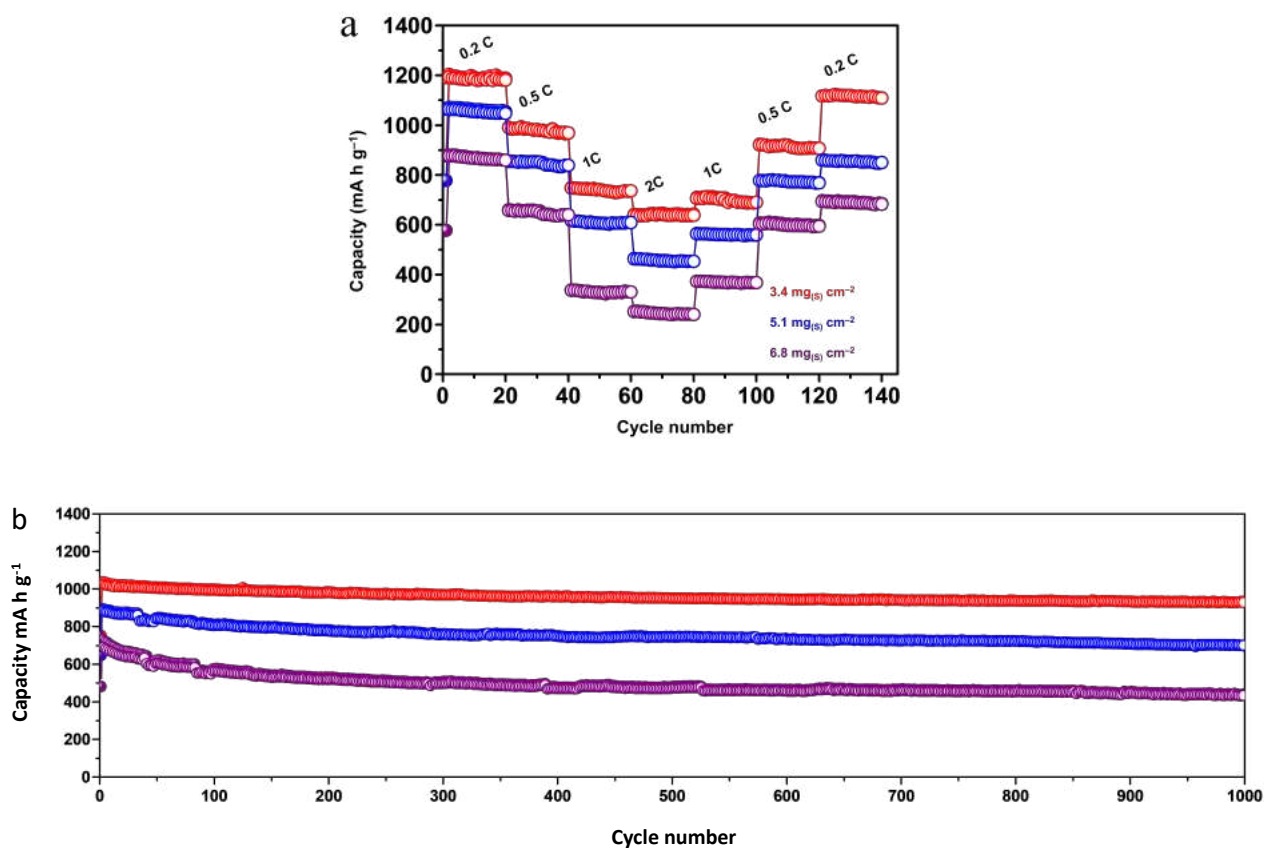


Figure 6.5: (a) rate capability of $\text{ACC@ITO@Na}_2\text{S}_6$ cathode at different current rates; and (b) long-term cycling performance of $\text{ACC@ITO@Na}_2\text{S}_6$ cathode with different sulfur loading at 0.5 C at $20^\circ\text{C} \pm 2^\circ\text{C}$.

With the intention to examine the superiority of activated carbon cloth decorated with tin-doped indium-oxide nanoparticle as current collector in terms of cycling performance, RT Na-S batteries were cycled at the different current rates. Figure 6.4a demonstrates the cycling performance of ACC@ITO@Na₂S₆ cathodes at 0.2 C, 0.5 C, 1C and 2C. The ACC@ITO@Na₂S₆ cathode exhibited high initial specific capacities of 1177 mA h g⁻¹, 990 mA h g⁻¹, 750 mA h g⁻¹, and 635 mA h g⁻¹ and a specific capacity of 1109 mA h g⁻¹, 921 mA h g⁻¹, 715 mA h g⁻¹, and 616 mA h g⁻¹ after 200 cycles maintained at 0.2 C, 0.5 C, 1C, and 2C, respectively. The charge-discharge profiles of the ACC@ITO@Na₂S₆ cathode at 0.2 C, 0.5 C, 1C, and 2C are shown in Figure 6.4b.

The corresponding specific capacities obtained at different current rates are plotted against cycle number and shown in Figure 6.5a. The ACC@ITO@Na₂S₆ cathode with sulfur loading of 3.4 mg cm⁻² (red) exhibited specific capacities of 1203 mA h g⁻¹, 991 mA h g⁻¹, 748 mA h g⁻¹, and 641 mA h g⁻¹ at 0.2 C, 0.5 C, 1C, and 2C, respectively. Figure 6.5b shows the long-term cycling performance of ACC@ITO@Na₂S₆ with sulfur loading 3.4 mg cm⁻² (red), 5.1 mg cm⁻² (blue) and 6.8 mg cm⁻² (purple) cathode for 1000 cycles at 0.5 C. During long-term cycling, the Na₂S₆@ACC cathode displayed an extremely stable cycling performance. With an average capacity loss of 0.01% per cycle, the cell delivered an initial capacity of 1036 mA h g⁻¹ and maintained a high capacity of 931 mA h g⁻¹ after 1000 cycles.

6.2.3 Understanding the catalytic behavior of ACC@ITO@Na₂S₆ cathode in Na-S battery

The ACC@ITO@Na₂S₆ cathode exhibited a new cathodic peak/discharge plateau at 1.98 V with good repeatability. Similarly, in comparison to CC@Na₂S₆ cathode, the ACC@ITO@Na₂S₆ cathode exhibits highly intense reduction peak at 1.65 V, associated with the conversion of Na₂S₂ to Na₂S. These observations strongly indicate the catalytic effect of ACC@ITO current collector in RT Na-S batteries to propel the redox conversion of intermediate products. Due to the catalytic activity of ACC@ITO current collector, the utilization of active species is increased, leading to both high nominal cell potential and high specific capacity. Both activated carbon and ITO are well known to behave as paramagnetic materials, owing to the presence of unpaired electrons.^{28–31} On the other hand, RT Na-S batteries undergo through tri-sulfur radical to monoanion (S_n^{•-}) as one of the major and stable intermediate products^{29–33}. A major fraction of as-formed higher- and middle-order polysulfides (i.e., S_n²⁻, 4 ≤ n ≤ 6) easily undergo through an “entropy-driven” dissociation process to generate the sulfur radical anion species³³.

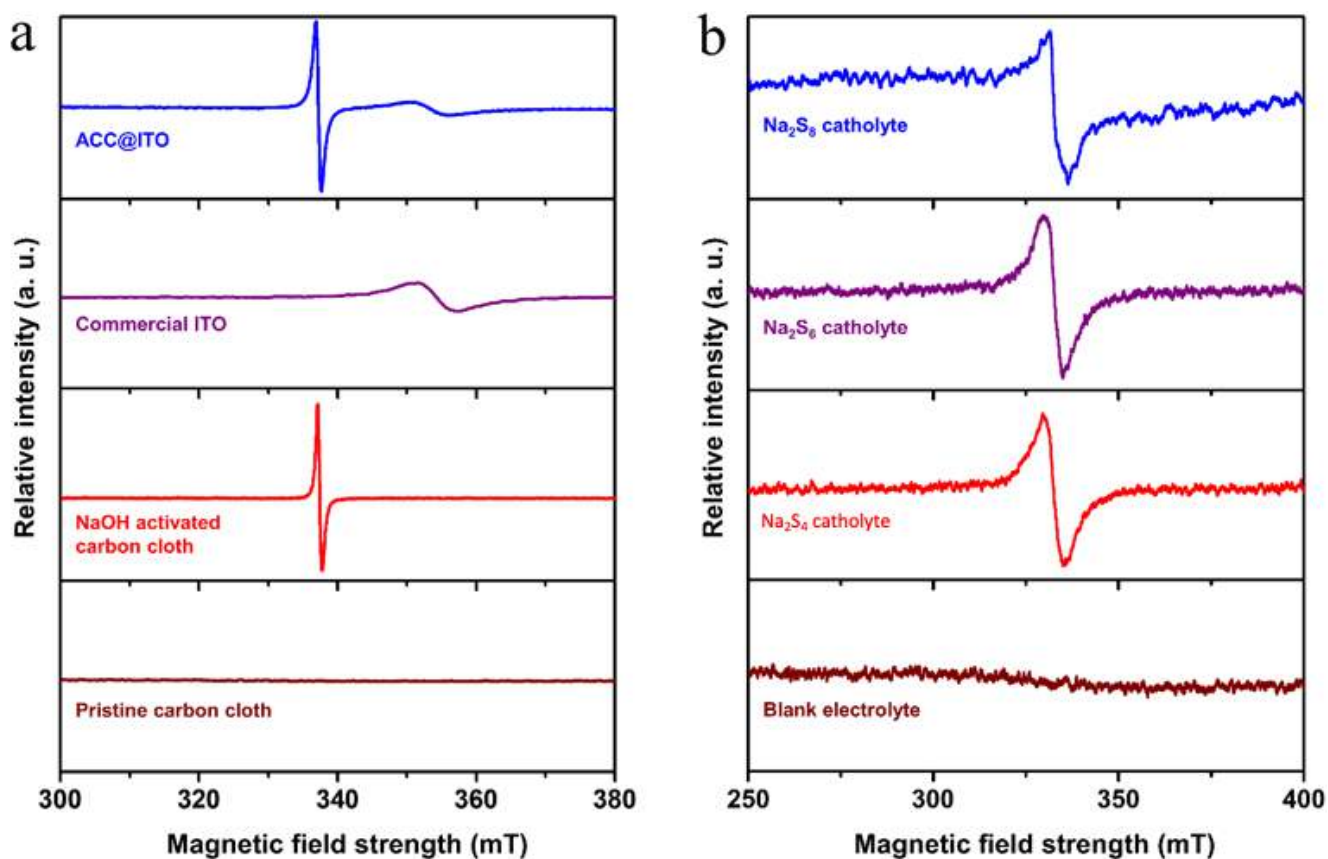


Figure 6.6: (a) ERS spectra of pristine carbon cloth, NaOH activated carbon cloth, ITO powder and activated carbon cloth decorated with tin-doped indium-oxide nanoparticle (ACC@ITO); (b) ESR spectra of blank electrolyte, Na₂S₄, Na₂S₆ and Na₂S₈ catholytes.

It is hypothesized that the redox conversion of active material is significantly enhanced through free-radical catalysis. However, to validate our prediction, electron paramagnetic resonance spectroscopy technique was employed to investigate the presence of unpaired electrons in individually activated carbon cloth, ITO and the chemically synthesized sodium polysulfides (Na₂S₄, Na₂S₆ and Na₂S₈). Figure 6.6a represents the ESR spectra of the pristine carbon cloth, NaOH-activated carbon cloth, commercial ITO powder and the as-prepared ACC@ITO substrate. The pristine carbon cloth shows no ESR signal, indicating the absence of any unpaired electrons. The NaOH-activated carbon cloth exhibited a strong ESR signal, due to generation of plenty of dangling bonds in the carbon structure during the chemical activation process. The unsaturated carbon atoms containing unpaired electrons (also called dangling bonds) serve as active sites in free-radical catalysis process. Interestingly, the ACC@ITO substrate exhibits two characteristic ESR active peaks of activated carbon cloth and indium tin oxide (ITO). The paramagnetism in ITO arises mainly due to oxygen vacancies in the crystal structure. Figure 6.6b

represents the ESR spectra of blank electrolyte and three different representative catholytes (i.e., Na_2S_4 , Na_2S_6 and Na_2S_8). The Na_2S_4 , Na_2S_6 and Na_2S_8 were catholytes was prepared chemically by dissolving a stoichiometric amount of elemental sulfur (S_8) and sodium sulfide (Na_2S). The reference blank electrolyte did not show any ESR activity, as expected. However, all three catholytes individually exhibited strong ESR signals. This observation confirms that in an aprotic solvent such as TEGDME, the polysulfide dianions (S_n^{2-}) tend to undergo “thermodynamically favorable” and “entropy-driven” dissociation process to produce paramagnetic $\text{S}_3^{\bullet-}$ radical-monoanion species.

The kinetic rate for any chemical reaction depends upon the amount of activation energy associated with that particular reaction. Higher the amount of activation energy, the chemical reaction experiences sluggish kinetics. In a catalytic reaction, the free energy released from any kind of weak noncovalent interactions or coupling between a catalyst and a substrate is the source of free energy used by the catalyst to decrease the activation energy required to complete the reaction.

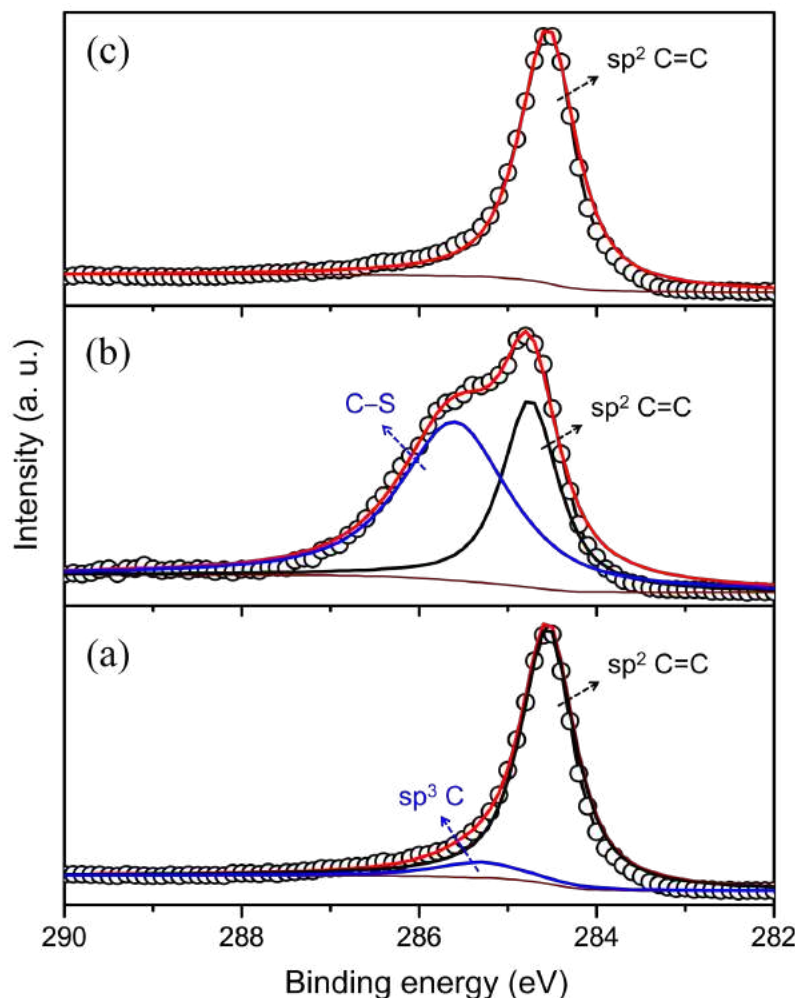


Figure 6.7: XPS spectra of fresh ACC@ITO (a), fully discharged Na_2S_6 @ACC cathode (b) and fully re-charged Na_2S_6 @ACC cathode (c).

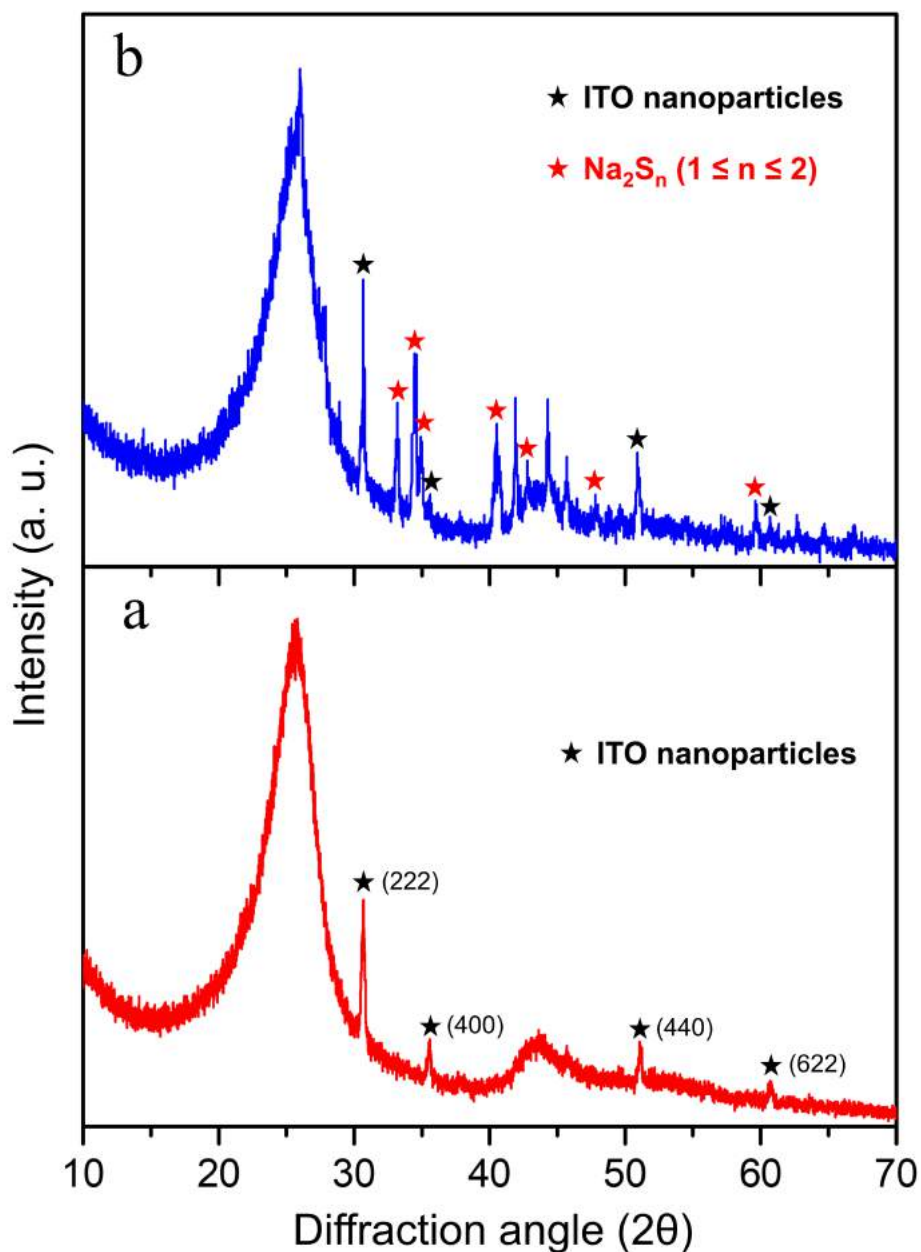


Figure 6.8: XRD pattern of ACC@ITO (a) and ACC@ITO@ Na_2S_6 cathode after 50 cycles at 0.2 C, at fully discharged state (b). The XRD pattern confirms the complete reduction of sulfur to lower-order sodium polysulfides (Na_2S_2 and Na_2S) as fully discharged products.

Free-radical coupling between two radical-containing species is one of the major sources of free energy required to lower the activation energy. When two free-radicals combine, the process releases

free energy, which compensates much of the energy required to lower the activation energy for the formation of the product.

Furthermore, we have carried out ex-situ XPS experiments to confirm the formation of C–S bonds during the discharge process through a free-radical coupling process and their subsequent cleavage during recharge. The XPS plot shown in Figure 6.7 depicts the reversible formation/breakage of C–S bonds during discharge/charge processes of Na-S batteries. Figure 6.7(a-c) depicts the deconvoluted C1s XPS spectrum of the $\text{Na}_2\text{S}_6@\text{ACC}@\text{ITO}$ cathode. Figure 6.7b depicts the C1s XPS spectrum of $\text{Na}_2\text{S}_6@\text{ACC}@\text{ITO}$ cathode exhibits an additional peak at 285.9 eV, corresponding to the formation of C–S bond at deep discharge. The formation of C–S bond is only possible through the coupling of the unpaired electrons present on activated carbon cloth and trisulfur radical-anion. However, the fully charged cathode (Figure 6.7c) exhibited the absence of characteristic peak of the C–S bond, indicating that during the charge process, the C–S bond dissociates to form the carbon dangling bonds and elemental sulfur.

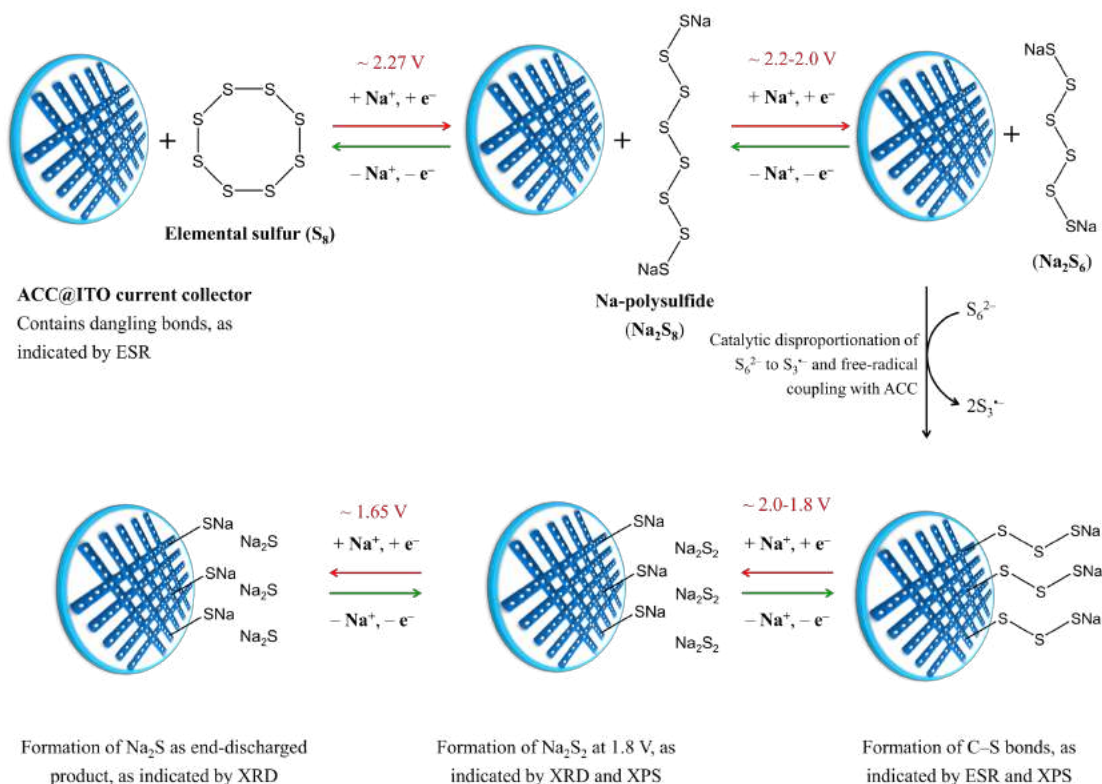


Figure 6.9: Reaction mechanism behind the catalytic effect of ACC@ITO in room temperature sodium-sulfur batteries.

After discharging the cell to 1.8 V, the confirmation of the product formed through the XRD pattern was recorded on the ACC@Na₂S₆ cathode. The XRD results depict the formation of Na₂S₂ as an insoluble lower-order polysulfides at 1.8 V (Figure 6.8). Again, the Na₂S₆@PCC cathode did not show any characteristic peaks of sodium-polysulfides after discharging to 1.8 V, as expected (Figure 6.8).

Based on these experimental observations, we propose that the dangling bonds (containing unpaired electrons), generated on the surface of activated carbon cloth, anchor the relatively stable S₃^{•−} radical monoanions from the electrolyte to accelerate their conversion to the lower-order polysulfides via the mechanism shown in Figure 6.9. It is believed that the carbon atoms possessing unpaired electrons (i.e., the dangling bonds) form chemical bonds with trisulfur radical monoanions (S₃^{•−}), generated during the discharge of RT Na-S batteries to create Na₂S₂ and ultimately to Na₂S as the end-discharged product. Hence, the activated carbon cloth catalyzes the conversion of sulfur to the lower-order sodium polysulfides as end-discharged products. The catalyst is regenerated during the charge process, through homolytic cleavage of C–S bonds as shown in Figure 6.9.

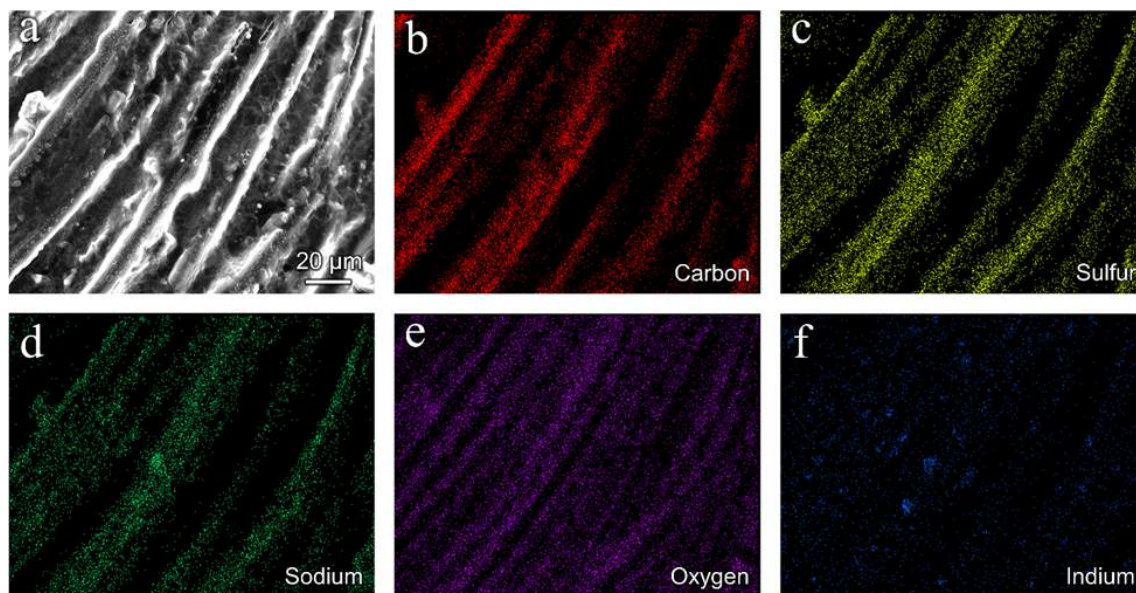


Figure 6.10: (a) Scanning electron microscopy image of ACC@ITO@ Na₂S₆ cathode after 1000 cycles, at fully discharged state; (b–f) mapping of different elements taken on the cycled electrode.

6.2.4 Post-cycling characterization of $\text{Na}_2\text{S}_6@\text{ACC}@\text{ITO}$ cathode after charge-discharge

The scanning electron microscopy technique was used to investigate the microstructure and morphology of the $\text{ACC}@\text{ITO}@\text{Na}_2\text{S}_6$ cathode after charge-discharge cycling. Figure 6.10a represents the SEM image of the $\text{ACC}@\text{ITO}@\text{Na}_2\text{S}_6$ cathode after 1000 cycles, at a fully discharged state. It is noteworthy that due to its high mechanical integrity, carbon cloth maintains the mechanical integrity of the electrode, even after long-term cycling performance. Moreover, from the SEM image, it can be observed that a dense product was deposited on the surface of activated carbon cloth. Sodium and sulfur mappings (Figure 6.10e & f) revealed that the dense product was, in fact, the mix phase of sodium polysulfides. It is believed that the discharge product was presumably retained through strong electrostatic interaction with the tin-doped indium oxide nanoparticles grown on the surface of activated carbon cloth.

6.3 Conclusions

A room-temperature sodium-sulfur battery that achieves high specific capacity with long-term stability has been practically realized using indium tin oxide nanoparticles. These ITO nanoparticles are decorated on activated carbon cloth as a novel current collector. The excellent electronic conductivity of the current collector drastically enhances the extent of the conversion of the active material in RT Na-S batteries. Indium tin oxide greatly immobilizes the higher-order sodium polysulfide species. Activated carbon cloth, apart from providing a continuous electron conduction pathway, catalyzes the conversion of higher-order sodium polysulfides to lower-order sodium sulfides. The rational design of a hybrid current collector described here will open a new direction to enhance the electrochemical performance of the RT Na-S.

References

1. C.W. Park, J. H. Ahn, H.S. Ryu, K. W. Kim and H. J. Ahn, *Electrochem. Solid-State Lett.*, 2006, 9, A123.
2. S. Wenzel, H. Metelmann, C. Reiß, C., A. K. Dürr, J. Janek and P. Adelhelm, *J. Power Sources*, 2013, 243, 758.
3. S. Xin, Y. X. Yin, Y.G. Guo and L. J. Wan, *Adv. Mater.*, 2014, 26, 1261.
4. X. Yu and A. Manthiram, *J. Phys. Chem. C*, 2014, 118, 22952.
5. I. Bauer, M. Kohl, H. Althues and S. Kaskel, *Chem. Commun.*, 2014, 50, 3208.
6. X. Yu and A. Manthiram, *Adv. Energy Mater.*, 2015, 5, 1500350.
7. X. Yu and A. Manthiram, *Chem. Eur. J.*, 2015, 21, 4233.
8. A. Manthiram and X. Yu, *Small*, 2015, 11, 2108.
9. I. Kim, J. Y. Park, C. H. Kim, J. W. Park, J. P. Ahn, J. H. Ahn, K.W. Kim and H.J. Ahn, *J. Power Sources*, 2016, 301, 332.
10. I. Kim, C. H. Kim, S. H. Choi, J. P. Ahn, J. H. Ahn, K. W. Kim, E. J. Cairns, and H. J. Ahn, *J. Power Sources*, 2016, 307, 31.
11. S. Wei, S. Xu, A. Agrawal, S. Choudhury, Y. Lu, Z. Tu, L. Ma and L. A. Archer, *Nat. Commun.*, 2016, 7, 11722.
12. Y.-X. Wang, J. Yang, W. Lai, S.-L. Chou, Q.-F. Gu, H. K. Liu, D. Zhao and S. X. Dou, *J. Am. Chem. Soc.* 2016, 138, 16576.
13. I. Kim, J. Y. Park, C. H. Kim, J. W. Park, J. P. Ahn, J. H. Ahn, K. W. Kim and H. J. Ahn, *J. Electrochem. Soc.*, 2016, 163, 611.
14. X. Yu and A. Manthiram, *Chem. Mater.*, 2016, 28, 896.
15. Y. M. Chen, W. Liang, S. Li, F. Zou, S. M. Bhaway, Z. Qiang, M. Gao, B. D. Vogt and Y. Zhu, *J. Mater. Chem. A*, 2016, 4, 12471.
16. Z. Qiang, Y. M. Chen, Y. Xia, W. Liang, Y. Zhu and B. D. Vogt, *Nano Energy*, 2017, 32, 59.
17. L. Fan, R. Ma, Y. Yang, S. Chen and B. Lu, *Nano Energy*, 2016, 28, 304.
18. Y.-X. Wang, B. Zhang, W. Lai, Y. Xu, S.-L. Chou, H.-K. Liu and S.-X. Dou, *Adv. Energy Mater.*, 2017, 7, 1602829.
19. R. Carter, L. Oakes, A. Douglas, N. Muralidharan, A. P. Cohn and C. L. Pint, *Nano Lett.* 2017, 17, 1863.

20. A. Ghosh, S. Shukla, M. Monisha, A. Kumar, B. Lochab and S. Mitra, *ACS Energy Lett.*, 2017, 2, 2478–2485.
21. S. Gope, D. K. Singh, M. Eswaramoorthy and A. J. Bhattacharyya, *Chemistry Select*, 2017, 2, 9249–9255.
22. Y. Hao, X. Li, X. Sun and C. Wang, *Chemistry Select*, 2017, 2, 9425.
23. D. Ma, Y. Li, J. Yang, H. Mi, S. Luo, L. Deng, C. Yan, M. Rauf, P. Zhang, X. Sun, X. Ren, J. Li and H. Zhang, *Adv. Funct. Mater.*, 2018, 28, 1705537.
24. Min-Kyu Jeon, Misook Kang, *Materials Letters*, 2008, 62, 676–682.
25. Jianrong Zhang, Lian Gao, Minghai Chen, *Materials Letters*, 2007, 61, 2671–2674.
26. X. Yu and A. Manthiram, *ChemElectroChem*, 2014, 1, 1275.
27. A. Manivannan, M. Chirila, N. C. Giles, M. S. Seehra, *Carbon*, 1999, 37, 1741.
28. O. Chauvert, L. Forro, *Physical Review B (Condensed Matter and Materials Physics)*, 1995, 52, R6963.
29. K. H. Wujcik, D. R. Wang, A. Raghunathan, M. Drake, T. A. Pascal, D. Prendergast and N. P. Balsara, *J. Phys. Chem. C*, 2016, 120, 18403.
30. Q. Wang, J. Zheng, E. Walter, H. Pan, D. Lv, P. Zuo, H. Chen, Z. D. Deng, B. Y. Liaw, X. Yu, X. Yang, J.-G. Zhang, J. Liu and J. Xiao, *J. Electrochem. Soc.*, 2015, 162, A474.
31. M. Vijayakumar, N. Govind, E. Walter, S. D. Burton, A. Shukla, A. Devaraj and S. Thevuthasan, *Phys. Chem. Chem. Phys.*, 2014, 16, 10923.
32. K. H. Wujcik, T. A. Pascal, C. D. Pemmaraju, D. Devaux, W. C. Stolte, N. P. Balsara and D. Prendergast, *Adv. Energy Mater.*, 2015, 5, 1500285.
33. T. Chivers and P. J. W. Elder, *Chem. Soc. Rev.*, 2013, 42, 5996.
34. O. El Jaroudi, E. Picquenard, N. Gobeltz, A. Demortier and J. Corset, *Inorg. Chem.*, 1999, 38, 2917.
35. G. J. Janz, J. R. Downey, E. Roduner, G. J. Wasilczyk, J. W. Coutts and A. Eluard, *Inorg. Chem.*, 1976, 15, 1759.
36. X. Lu, B. W. Kirby, W. Xu, G. Li, J. Y. Kim, J. P. Lemmon, V. L. Sprenkle and Z. Yang, *Energy Environ. Sci.*, 2013, 6, 299.
37. J.-T. Yeon, J.-Y. Jang, J.-G. Han, J. Cho, K. T. Lee and N.-S. Choi, *J. Electrochem. Soc.*, 2012, 159, A1308.

Chapter 7

Concluding Remarks and Future Scope

Chapter 7

Concluding Remarks and Future Scope

The objective of this thesis is to mitigate the major challenges that are associated with the sulfur cathode material in RT-NaS batteries. In this study, a successful attempt has been made to enhance the energy density and cyclability of RT-NaS batteries. Throughout the thesis, the modification of an electronically conductive cathode scaffold has been carried out. The cathode scaffold that is decorated with MnO₂ nanoarrays wrapped with alginate binders. Further, the catalytic activity of the activated carbon cloth that is decorated with conductive ceramic nanoparticles (ITO) has been studied. The high-performance cathode that is a result of such surface modification yields a high energy-density RT-NaS battery.

In summary, a high energy-density room-temperature Na-S battery has been practically realized by incorporating a CC@MnO₂ substrate containing Na₂S₆ catholyte as an efficient multifunctional cathode. The Na-S cell offered an initial energy density of 946 W h kg⁻¹, and retained 728 W h kg⁻¹ after 500 cycles. The mechanism of interaction between MnO₂ and intermediate products was investigated through XPS, which revealed the *in-situ* formation of polythionate complexes through disproportionation reactions of higher-order polysulfides in the presence of thiosulfate surface species. The polythionate complexes anchored the polysulfides, restricting their rapid dissolution. We believe that the concept of employing a sodium polysulfide catholyte as active material, and CC@MnO₂ as both an electronically conductive substrate and a polysulfide reservoir, could encourage the practical realization of room-temperature sodium-sulfur batteries with high energy output.

In summary, we have developed a mechanically robust, integrated cathode scaffold consisting of sodium-alginate wrapped MnO₂ nanoarrays decorated carbon cloth which synergistically increase the redox kinetics and mitigate fatal polysulfide shuttling and the electrode pulverization. Here, carbon cloth provides continuous electronic pathway, whereas, MnO₂ nanoarrays and sodium-alginate nanofibers offer enormous adsorption sites to bind the sodium-polysulfides chemically and physically and further accelerate the redox conversion. The CC@MnO₂@Na-alg substrate infiltrated with Na₂S₆ catholyte has delivered an initial reversible specific capacity of 882 mA h g⁻¹, retaining 838 mA h g⁻¹ after 1000 cycles. Addition of alginate results in an enhancement in specific capacity and capacity retention of CC@MnO₂ architecture by 37% and 10%, respectively. This superior electrochemical performance has been attributed to the fibrous nature of alginate which promotes the faster transport of ions and complete utilization of active material. Furthermore, a complete computational analysis estimates the possible binding sites and binding strength of alginate molecule towards PS confinement.

Room temperature sodium-sulfur batteries achieving a high nominal cell potential of 1.85 V have been successfully demonstrated using an activated carbon cloth as current collector and polysulfide reservoir. The activated carbon cloth significantly catalyzes the conversion of intermediate trisulfur radical monoanions to the end-discharge products. Electron spin resonance spectroscopy reveals the existence of carbon atoms containing unpaired electrons in the activated carbon cloth, and *in-situ* Raman spectroscopy confirms the formation of the $S_3^{\bullet-}$ radical monoanions during discharge. We propose that a coupling between the unpaired electrons of activated carbon cloth and trisulfur radical monoanions is responsible for observed catalytic enhancement in the kinetics, addressing several major issues that these batteries face. The achievement of an increased nominal cell potential, combined with excellent specific capacity and capacity retention at practical rates, produce a step forward in cell energy density with extremely stable cycle life. These properties, combined with inexpensive starting materials and manufacturing should propel the RT Na-S battery closer to practical application.

The report also discusses another room-temperature sodium-sulfur battery achieving high specific capacity with long-term stability that has been practically realized using indium tin oxide nanoparticles decorated activated carbon cloth as a novel current collector. The excellent electronic conductivity of the current collector enhances the extent of active material conversion drastically in RT Na-S batteries. Indium tin oxide greatly immobilizes the higher-order sodium polysulfide species. Activated carbon cloth, apart from providing a continuous electron conduction pathway, catalyses the conversion of higher-order sodium polysulfides to lower-order sodium sulfides. The rational design of a hybrid current collector described here will open new possibilities to enhance the electrochemical performance of the RT Na-S.

The chemical stability of anode with the electrolyte determines the long-term cycle stability of RT Na-S batteries. Metallic sodium is unstable with organic electrolytes and reacts with dissolved polysulfides, which hampers the performance of rechargeable batteries. Therefore, the future work may possibly include the search for a more suitable electrolyte that can enable the suppression of polysulfide dissolution, and introduction to electrolyte additives which can passivate and protect the sodium-anode surface. Further, the investigation of all solid-state RT-NaS cell can be the future scope of this work.

Publications

Peer reviewed journal:

1. **A Kumar**, A Ghosh, A Roy, MR Panda, M Forsyth, DR MacFarlane, S Mitra, High-energy density room temperature sodium-sulfur battery enabled by sodium polysulfide catholyte and carbon cloth current collector decorated with MnO₂ nanoarrays, *Energy Storage Materials*, 2019, 20, 196-202.
2. **A Kumar**, A Ghosh, M Forsyth, DR MacFarlane, S Mitra, Free-radical catalysis enhances the redox kinetics of room-temperature sodium-sulfur batteries, *ACS Energy Lett.* 2020, 5, 6, 2112–2121.
3. **A Kumar**, A Ghosh, Arpita Ghosh, Aakash Ahuja, M Forsyth, DR MacFarlane, S Mitra, A Robust Cathode Scaffold for Room-Temperature Sodium-Sulfur Batteries (Manuscript).
4. **A Kumar**, A Ghosh, M Forsyth, DR MacFarlane, S Mitra, Indium-tin-oxide (ITO) decorated activated carbon cloth as a current collector for room-temperature sodium-sulfur batteries (Manuscript).

Conference Proceeding:

1. **A. Kumar**, A High-Performance Cathode Scaffold for Room-Temperature Sodium Sulfur Batteries, 2018 MRS Fall Meeting & Exhibit, November 26, 2018 (Oral)

Other Contributions:

1. A Ghosh, S Shukla, M Monisha, **A Kumar**, B Lochab, S Mitra, Sulfur copolymer: a new cathode structure for room-temperature sodium–sulfur batteries, *ACS Energy Letters* 2017, 2 (10), 2478-2485.
2. A Roy, A Ghosh, **A Kumar**, S Mitra, A high-performance sodium anode composed of few-layer MoSe₂ and N, P doped reduced graphene oxide composites, *Inorganic Chemistry Frontiers* 2018, 5 (9), 2189-2197.
3. **A Kumar**, A Ghosh, S Mitra, M R Panda, Electrochemical Cell Including Optical Window Made of Transparent Adhesive Tape and Method for Manufacturing thereof, IN Patent App. 52555/2018-MU M.

4. S Mitra, M R Panda, A Ghosh, A Raj, **A Kumar**, Q Bao, Rechargeable Sodium-ion Batteries Based on Layered Electrode Materials and Method of Fabricating the Same, IN Patent App. 35761/2018-MU M
5. D Muthuraj, A Ghosh, **A Kumar**, S Mitra, Nitrogen and Sulfur Doped Carbon Cloth as Current Collector and Polysulfide Immobilizer for Magnesium-sulfur Batteries ChemElectroChem 2019, 6 (3), 684-689
6. A Ghosh, **A Kumar**, A Roy, MR Panda, M Kar, DR MacFarlane, S Mitra, Three-Dimensionally Reinforced Freestanding Cathode for High-Energy Room-Temperature Sodium–Sulfur Batteries, ACS applied materials & interfaces 2019, 11 (15), 14101-14109
7. A Ghosh, **A Kumar**, M Kar, D MacFarlane, S Mitra, Cathode electrode for lithium-sulfur batteries, IN Patent App. 201,921,040,500
8. Arnab Ghosh, **Ajit Kumar**, Amlan Roy, Cuong Nguyen, Aakash Ahuja, Md. Adil, Manjunath Chatti, Mega Kar, Douglas R. MacFarlane, and Sagar Mitra, Ultrathin Lithium Aluminate Nanoflake-Inlaid Sulfur as a Cathode Material for Lithium–Sulfur Batteries with High Areal Capacity, *ACS Appl. Energy Mater.* 3, 2020, 3,6, 5637–5645
9. Monisha Monisha, P Preetham, Arnab Ghosh, **Ajit Kumar**, Saad Zafar, Sagar Mitra, Bimlesh Lochab, Halogen-free flame-retardant sulfur copolymers with stable Li–S battery performance, Energy Storage Materials, 2020, 29, 350-360

Acknowledgements

I would like to express my deepest gratitude to my supervisors, Prof. Sagar Mitra, Prof. Douglas R. MacFarlane & Prof. Maria Forsyth for their constant support, encouragement and guidance so that I could complete this thesis. I am very thankful for the opportunity to work with them.

I would also like to thank my research progress committee members, Prof. Venkatasailanathan Ramadesigan, Prof. Xinyi zhang for their time and inputs for guiding my Ph.D work.

I am so fortunate to have very friendly and cooperative senior colleagues and lab mates. I would like to thank all the former ECEL members Dr. Pavan Srinivas Veluri, Dr. Sowmiya Theivaprakasam, Dr. Shivani Singh, Dr. C.V. Manohar, Dr. Ananta Sarkar, Dr. Md. Furquan, for introducing me to all the instruments and provide necessary training for their operation during initial stage of my Ph.D. I am very thankful to all my colleagues, Dr. Arpita Ghosh, Divyamahalakshmi, Prasit Kumar Dutta, Manas Ranjan Panda, Amlan Roy, Md. Adil, Tuhin Subhra Sahu, Preetham Permude, Govind Mishra, Supriya Sau, Manoj Gautam, Abhinanda Sengupta, Harshita Lohani, Rohini K. V, Pradeep Kumar, Shashidhar Reddy, Murali Krishna and Bhawana, for their support and encouragement. I am especially thankful to Arnab Ghosh for supporting me each and every time on different problems in the research work. I would like to express my special thanks to Aakash Ahuja for his support to organize the thesis. Furthermore, I would like to thank ECEL staff member, Mr. Ajay Shivsharan for his continuous support. I am also thankful to Mr. Ashish and Mr. Dubey for supplying chemicals and necessary stuffs at very short time notice.

I am very grateful to have such a nice and friendly environment in the Department of Energy Science and Engineering. I would like to thank IIT-B Monash Research Academy for providing great collaboration work and infrastructure to pursue my research work at IIT Bombay and Monash university. I am very much thankful to all the staff of IITB-Monash Research Academy, and special thanks to both Seba Sanjay and Krishna Warriar. I would like to express my deepest gratitude to Prof. Murali Sastry the CEO of IITB-Monash Research Academy, for his constant support and encouragement towards the research. I am very much thankful to all the technical staff of Central Research Facility (SAIF), National Centre for Photovoltaics Research and Education (NCPRE) and Industrial Research and Consultancy Centre (IRCC), IIT Bombay for providing financial and instrumental supports.

Last but not the least, I am very grateful to my wife, Poonam, my family members and friends, whose unconditional love and support has always been a source of inspiration for me.

